Modeling and Analysis of Chemical Degradation and Gas Crossover in Proton Exchange Membrane Electrolyzers

Modellierung und Analyse chemischer Degradation und des Gasdurchtritts in Protonenaustauschmembran-Elektrolyseuren

Von der Fakultät für Maschinenwesen der Rheinisch-Westfälischen Technischen Hochschule Aachen zur Erlangung des akademischen Grades eines Doktors der Ingenieurwissenschaften genehmigte Dissertation

vorgelegt von

Sven Michael Dörner

Berichter: Univ.-Prof. Alexander Mitsos, Ph.D.
Asst. Prof. Dr.-Ing. Dominik Bongartz

Tag der mündlichen Prüfung: 22.05.2026

Titel: Modeling and Analysis of Chemical Degradation and Gas Crossover in Proton Exchange Membrane Electrolyzers

Autor: Sven Michael Dörner

Reihe: Aachener Verfahrenstechnik Series
AVT.SVT - Process Systems Engineering
Band 46 (2026)

Herausgeber: Aachener Verfahrenstechnik
Forckenbeckstraße 51
52074 Aachen
Tel.: +49 (0)241 80 97717
Fax.: +49 (0)241 80 92326
E-Mail: secretary.svt@avt.rwth-aachen.de
https://www.avt.rwth-aachen.de

Volltext verfügbar: https://doi.org/RWTH-2026-05728

Vorwort

Die vorliegende Arbeit entstand im Rahmen einer Industriepromotion während meiner Tätigkeit bei der Siemens Energy AG in Frankfurt am Main.
Mein besonderer Dank gilt zunächst meinen akademischen Betreuern, Prof. Alexander Mitsos, Ph. D., und Prof. Dr.-Ing. Dominik Bongartz, die mich während der gesamten Promotionszeit fachlich wie auch persönlich in herausragender Weise begleitet haben. Ihre wissenschaftlichen Anregungen, ihre konstruktive Kritik sowie ihr Vertrauen haben wesentlich zum Gelingen dieser Arbeit beigetragen.
Ebenso danke ich meinen Betreuern bei Siemens Energy, insbesondere Dr. Rüdiger Schneider und Dr. Markus Kinzl, für die kontinuierliche Unterstützung, die wertvollen fachlichen Diskussionen und die Möglichkeit, diese Arbeit in einem industriellen Umfeld mit hoher praktischer Relevanz durchführen zu können. Mein Dank gilt zudem meinen Kollegen Dr. Henning Schramm und Dr. Ralf Joh für die angenehme Zusammenarbeit, den fachlichen Austausch und ihre Unterstützung im Arbeitsalltag.
Weiterhin möchte ich mich bei meinen Abschlussarbeitern bedanken, insbesondere bei Johannes Paduch und Pitt Lucht, für ihre engagierte Mitarbeit und die konstruktive Zusammenarbeit.
Der größte Dank gilt meiner Familie für ihre bedingungslose Unterstützung und ihren Rückhalt über all die Jahre. Mein besonderer Dank gilt meinen Eltern Susanne und Michael Dörner sowie meiner Frau Anna Dörner für ihre Geduld, ihr Verständnis und ihre stetige Ermutigung. Ebenso danke ich unserer Tochter Eliana Dörner, die diese Zeit auf ihre ganz eigene Weise bereichert hat.

Düsseldorf, Januar 2026 *Sven Michael Dörner*

Contents

Kurzfassung

Die vorliegende Arbeit untersucht die Leistungsfähigkeit und Langzeitstabilität von Protonenaustauschmembran-Elektrolyseuren (PEM-Elektrolyseuren), einer Schlüsseltechnologie für die nachhaltige Wasserstofferzeugung. PEM-Elektrolyseure zeichnen sich durch hohe Effizienz, schnelle Dynamik und einen kompakten Systemaufbau aus und gelten daher als vielversprechend für die Integration in zukünftige Energiesysteme. Ihre breite industrielle Anwendung wird jedoch durch hohe Systemkosten, betriebliche Unsicherheiten und eine begrenzte Langzeitstabilität erschwert, wobei Degradationsprozesse eine zentrale Rolle spielen.

Ziel dieser Dissertation ist es, das mechanistische Verständnis der chemischen, transportbedingten und verunreinigungsinduzierten Prozesse zu vertiefen, die die Degradation von PEM-Elektrolyseuren bestimmen. Zu diesem Zweck werden drei komplementäre Modelle in Kombination mit experimenteller Validierung eingesetzt: (i) ein dynamisches Modell der chemischen Membrandegradation, (ii) ein experimentell validiertes Modell für den Wasserstoff- und Sauerstoffdurchtritt durch die Membran unter industriell relevanten Drücken sowie (iii) ein Mehrkomponenten-Ionenaustauschmodell zur Modellierung der Entfernung gelöster Eisenverunreinigungen. Aus den Ergebnissen ergibt sich eine konsistente mechanistische Interpretation, nach der der Sauerstoffdurchtritt die Bildung von Wasserstoffperoxid und radikalischen Spezies beeinflusst, der Eiseneintrag die chemische Membrandegradation über Fenton-Reaktionen verstärkt und der Ionenaustausch diese durch Begrenzung katalytisch aktiver Verunreinigungen mitigiert.

Die chemische Membrandegradation wird mithilfe eines dynamischen, ortsgemittelten Modells untersucht, das das Reaktionsnetzwerk hydroxylischer Radikale, Peroxidbildungsprozesse sowie eine semi-empirische Beschreibung des Sauerstoffdurchtritts kombiniert. Das Modell reproduziert experimentell beobachtete Fluoridfreisetzungsraten und charakteristische Degradationstrends, wie ein Maximum bei mittleren Stromdichten, und quantifiziert den Einfluss von Betriebsparametern wie Druck und Stromdichte. Zur Erweiterung der Datenbasis für Gasdurchtrittsmodelle werden großskalige Messungen des Wasserstoff- und Sauerstoffdurchtritts an einem sechszelligen PEM-Elektrolyseur bei 60 °C und Drücken bis 8,5 bar durchgeführt. Die Ergebnisse zeigen eine nichtlineare Abhängigkeit des Sauerstoffdurchtritts vom Druck, die mit bestehenden Modellen nicht erfasst werden kann und zur Entwicklung eines modifizierten Ansatzes mit stromdichteabhängiger Übersättigung und elektroosmotischem Schleppeffekt führt. Ergänzend wird ein räumlich aufgelöstes Mehrkomponenten-Ionenaustauschmodell entwickelt, das die konkurrierende Adsorption von Fe^{2+}- und Fe^{3+}-Ionen im Prozesswasser beschreibt, auf einer erweiterten Langmuir-Formulierung basiert und Einblicke in Verunreinigungsdynamik und Minderungsstrategien liefert.

Insgesamt tragen die entwickelten Modelle und experimentellen Ergebnisse zu einem vertieften Verständnis degradationsrelevanter Prozesse in PEM-Elektrolyseuren bei, wobei die drei Beiträge komplementäre Aspekte der chemischen Membranalterung adressieren.

Summary

This thesis investigates the performance and long-term durability of Proton Exchange Membrane (PEM) electrolyzers, a key technology for sustainable hydrogen production. PEM electrolyzers offer high efficiency, fast dynamic response, and compact system design, making them promising candidates for large-scale integration into future energy systems; their widespread deployment, however, is challenged by high system costs, operational uncertainties, and limited long-term durability, with degradation phenomena playing a central role.

The objective of this dissertation is to advance the mechanistic understanding of the chemical, transport, and impurity-related processes that govern PEM electrolyzer degradation. To this end, the thesis combines three complementary models with experimental validation: (i) a dynamic model of chemical membrane degradation, (ii) an experimentally validated model for hydrogen and oxygen gas crossover under industrially relevant pressures, and (iii) a multi-species ion exchange model for the removal of dissolved iron impurities. Taken together, the results support a coherent mechanistic interpretation of how oxygen crossover influences hydrogen peroxide formation and radical chemistry, how iron ingress amplifies chemical membrane degradation via Fenton reactions, and how ion exchange mitigates degradation by limiting the availability of catalytic impurities.

Chemical membrane degradation is examined using a dynamic lumped model that combines the hydroxyl-radical reaction network, hydrogen-peroxide formation pathways, and a semi-empirical oxygen crossover formulation, reproducing experimentally reported fluoride release rates and characteristic degradation trends such as a maximum at intermediate current densities, while quantifying the influence of operating conditions such as pressure and current density. To address the scarcity of high-pressure experimental data, new measurements of hydrogen and oxygen crossover are presented for a six-cell PEM electrolyzer operated at 60 °C and pressures up to 8.5 bar, revealing a nonlinear dependence of oxygen crossover on pressure that is not captured by existing approaches and motivating a modified model incorporating current-dependent supersaturation and electro-osmotic water drag. A modified oxygen crossover model incorporating current-dependent supersaturation and electro-osmotic water drag is introduced and shown to provide improved agreement with experimental results. In addition, a spatially resolved multi-species ion exchange model is developed to describe the competitive adsorption of Fe^{2+} and Fe^{3+} ions in electrolyzer process water; the model extends multi-component Langmuir theory and captures the essential interaction between ferrous and ferric ions observed in equilibrium and breakthrough experiments, providing insights into exchanger performance and impurity transport dynamics.

Overall, the models and experimental results presented in this thesis contribute to a more comprehensive understanding of degradation-relevant processes in PEM electrolyzers. The three investigated topics are physically connected by their roles in chemical membrane aging, addressing complementary aspects of the same degradation pathway spanning transport phenomena, chemical reaction mechanisms, and mitigation strategies.

Publications and Copyrights

This dissertation is based on research conducted by the author in the context of an industrial doctoral program in cooperation with Siemens Energy and the Chair of Process Systems Engineering (AVT.SVT) at RWTH Aachen University between March 1, 2021 and January 31, 2026. Parts of this dissertation have already been published as described in the following.

Relation between thesis chapters and publications

- Chapter 1 (Introduction) was written specifically for this dissertation and provides an overarching description of the research topics addressed in Publications P1–P3.
- Chapter 2 is reproduced/adapted in part from Publication P1. [1]
- Chapter 3 is reproduced/adapted in part from Publication P3. [2]
- Chapter 4 is reproduced/adapted in part from Publication P2. [3]
- Chapter 5 (Conclusion) was written specifically for this dissertation and provides an overarching summary and outlook on the research topics addressed in Publications P1–P3.

Peer-reviewed journal publications forming part of this dissertation

P1 **S. Dörner**, M. Kinzl, A. Mitsos, and D. Bongartz. *Dynamic lumped cell-level model of chemical membrane degradation in PEM electrolysis: Impact of pressure and time dependence*. Industrial & Engineering Chemistry Research, 64(52):24982-24993, 2025. [1]

Author contributions (CRediT): S. Dörner: writing – original draft, conceptualization, methodology, investigation, visualization. M. Kinzl: writing – review & editing, conceptualization. A. Mitsos: writing – review & editing, conceptualization, supervision. D. Bongartz: writing – review & editing, conceptualization, methodology, supervision.

P2 **S. Dörner**, J. Paduch, C. Plath, M. Wessling, A. Mitsos, and D. Bongartz. *Multi-species ion exchange model with competitive adsorption for iron removal in PEM water electrolysis*. Chemical Engineering Research and Design, 222:325-339, 2025. [3]

Author contributions (CRediT): S. Dörner: conceptualization, methodology, writing – original draft, visualization, supervision. J. Paduch: methodology, software, formal analysis, investigation, validation. C. Plath: supervision. M. Wessling: supervision. A. Mitsos: writing – review & editing, conceptualization, supervision. D. Bongartz: writing – review & editing, conceptualization, methodology, supervision.

P3 **S. Dörner**, A. Mitsos, and D. Bongartz. *Gas Crossover in PEM Electrolyzers: Experimental Validation and Improved Oxygen Crossover Model.* Chemical Engineering Science, 324:123310, 2026. [2]

Author contributions (CRediT): S. Dörner: writing – original draft, conceptualization, methodology, investigation (computational part), visualization. A. Mitsos: writing – review & editing, conceptualization, supervision. D. Bongartz: writing – review & editing, conceptualization, methodology, supervision.

Student theses supervised / co-supervised (work partially used in this dissertation)

- J. Paduch. *Modellierung und Simulation der Reduzierung von Eisenionen in einer PEM-Elektrolyse-Anlage (Modeling and Simulation of Iron Ion Reduction in a PEM Electrolysis Plant).* Master's thesis, RWTH Aachen University, Chair of Chemical Process Engineering, Aachen, 2022. [4]
- P. Lucht. *Modelling and Simulation of Degradation-Causing Ion Release in PEM Electrolysis Plants.* Master's thesis, Hochschule für Angewandte Wissenschaften Hamburg, Faculty of Engineering and Computer Science, in collaboration with Siemens Energy AG, Hamburg, 2022. [5]

J. Paduch's master's thesis, which I co-supervised, established a first multi-species ion exchange model for iron removal and the corresponding analysis. Building on this work, the model was further developed, validated, and consolidated into Publication P2 as part of this dissertation.

Copyright / Permissions

1. Introduction

Hydrogen (H_2) has emerged as a critical energy carrier in the global transition toward a sustainable economy, primarily due to its potential to decarbonize multiple end-use sectors and its ability to store and distribute energy flexibly [6]. Among the various technologies for green hydrogen production, Proton Exchange Membrane (PEM) electrolyzers have gained significant attention. These devices offer high energy efficiency, rapid response to varying power inputs, and a compact design, making them suitable for integration with renewable energy sources [7]. However, the widespread deployment of PEM electrolyzers is constrained by several interrelated challenges, including high system costs, operational complexity, and long-term durability [7]. The overall performance of a PEM electrolyzer is typically assessed in terms of its energy efficiency, its durability over the targeted lifetime, and the resulting hydrogen production cost. These metrics are affected by several loss and degradation mechanisms, including catalyst degradation, mechanical and thermal membrane failure, contamination, and chemical degradation of the membrane, as well as by gas crossover. Among these, this thesis focuses on chemical membrane degradation, gas crossover, and iron contamination, which are closely coupled and directly affect efficiency, safety margins, and lifetime [8]. In addition to membrane degradation itself, gas crossover phenomena and impurity-related effects play an important role in both performance losses and degradation pathways [6].
The objective of this thesis is to enhance the understanding of chemical degradation mechanisms in PEM electrolyzer systems and to improve the modeling of degradation and gas crossover phenomena under varying operating parameters. The modeling-based approach supports the analysis of degradation-relevant mechanisms and their potential mitigation. The models are then used to analyze and identify favorable operating regimes. By tackling these interrelated issues, this work provides guidance relevant to the efficiency, longevity, and overall performance of PEM electrolyzers.

1.1. Chemical Membrane Degradation

Chemical membrane degradation denotes the irreversible chemical attack on the perfluorosulfonic acid (PFSA) polymer by reactive oxygen species, in particular hydroxyl radicals. These radicals cleave the polymer side chains and backbone, causing fluoride release, membrane thinning, and loss of mechanical and ionic integrity, ultimately leading to pinhole formation and failure. The performance of PEM electrolyzers is highly dependent on the integrity of the polymer electrolyte membrane. Chemical degradation poses a significant threat to membrane structure, leading to reduced efficiency, increased gas crossover, and shortened operational lifespan [9, 10]. Factors contributing to this degradation include temperature, oxygen (O_2) crossover, and the transport of ferrous ions (Fe^{2+}) from corroding iron-containing components within the electrolyzer [11]. A major mechanism driving chemical degradation is the formation of hydrogen peroxide and radical species

via Fenton-type reactions, which exacerbates membrane deterioration and increases the electrical resistance of the membrane [9]. In addition, elevated gas crossover can reduce hydrogen production efficiency and pose safety risks due to the formation of explosive gas mixtures, particularly under pressurized operation [12].
Understanding these degradation mechanisms is crucial for developing accurate predictive models. Initial models in the literature focused on fuel cells, considering fundamental kinetic mechanisms and transport phenomena. For example, Shah et al. developed a time-dependent 1D fuel cell model that included kinetic degradation mechanisms and transport phenomena, providing insights into diffusion within the material [13]. Gubler et al. extended this approach by designing a 0D chemical degradation model that described the formation and consumption of radical intermediates [9]. Further advancements were made by Ghelichi et al., who discretized the Nafion membrane structure, offering deeper insights into degradation processes [14].
In the context of PEM electrolyzers, Chandesris et al. developed a 1D model that incorporated temperature and current density effects, highlighting operational conditions that accelerate degradation [11]. Frensch et al. expanded this model by including additional reaction pathways, validating it with experimental data, and emphasizing the impact of iron ions and hydrogen peroxide on fluoride emissions [15]. However, these models either address fuel cells rather than electrolyzers, are restricted to steady state, or neglect key operating parameters such as pressure and the dynamic, time-dependent evolution of degradation. A dynamic, electrolyzer-specific cell-level model linking these operating parameters to the degradation rate is therefore still missing.

1.2. Gas Crossover

Accurate modeling of gas crossover is crucial for optimizing electrolyzer performance and avoiding the risk of explosive gas mixtures. Various models have been developed to address fundamental phenomena, such as those by Choi et al. [16], which focused on basic gas and water crossover mechanisms, and by Ito et al. [17], which introduced solubility and diffusion coefficients to calculate permeability. Schalenbach et al. [12] employed Fick's law to establish crossover rates, fitting hydrogen diffusion coefficients to experimental data, while Trinke et al. [18] extended these models to include supersaturation effects. Further studies by Afshari et al. [19] and Omrani et al. [20] explored the impact of various operating conditions on crossover, but lacked large-scale experimental validation.
Recognizing these gaps, this thesis adapts and extends an established supersaturation-based hydrogen crossover model to describe oxygen crossover and validates it through large-scale experiments to bridge the gap between theoretical models and practical applications [18].

1.3. Iron Contamination and Ion Exchange

Ion exchange systems can significantly mitigate membrane degradation by effectively removing Fe ions from process water. Initial models focused on single-ion removal, but Melis et al. [21] developed a competitive adsorption model for multiple species. Van Assche et al. [22] further refined this approach by considering the size of adsorbent molecules. How-

ever, these models have not been tailored specifically for PEM electrolyzers. This thesis addresses this gap by developing a comprehensive ion exchange model for PEM electrolyzers, predicting competitive adsorption of Fe^{2+} and Fe^{3+} ions, and solving mass balances dynamically. The model is discretized along its length to account for spatial distribution in the ion exchanger, and validated against laboratory experiments to provide critical insights for designing and operating ion exchange systems that mitigate membrane degradation and enhance performance.

1.4. Objective and Structure of this Thesis

This dissertation is structured as follows. Chapter 2 investigates the chemical degradation of the polymer electrolyte membrane in PEM electrolyzers by developing a dynamic, lumped model that captures radical-driven degradation mechanisms and their dependence on operating conditions. Chapter 3 focuses on hydrogen and oxygen crossover across the membrane, combining experimental measurements under industrially-relevant pressures with the evaluation and refinement of existing crossover models. Chapter 4 addresses the role of metal-ion impurities by developing a dynamic multi-species ion exchange model for the removal of dissolved iron ions from the electrolyzer process water. Finally, Chapter 5 summarizes the main findings of the dissertation and discusses their implications and limitations, as well as directions for future research.
To provide an overview of the physical context of the investigated phenomena, Figure 1.1 illustrates a schematic PEM electrolyzer and highlights the specific components and transport pathways addressed by the modeling approaches developed in this dissertation. The figure indicates where the phenomena addressed in this dissertation are located within the electrolyzer: chemical membrane degradation (Chapter 2) and gas crossover (Chapter 3) both occur within and across the membrane and are therefore closely related, while ion exchange (Chapter 4) takes place in a distinct domain, the anode water circuit.

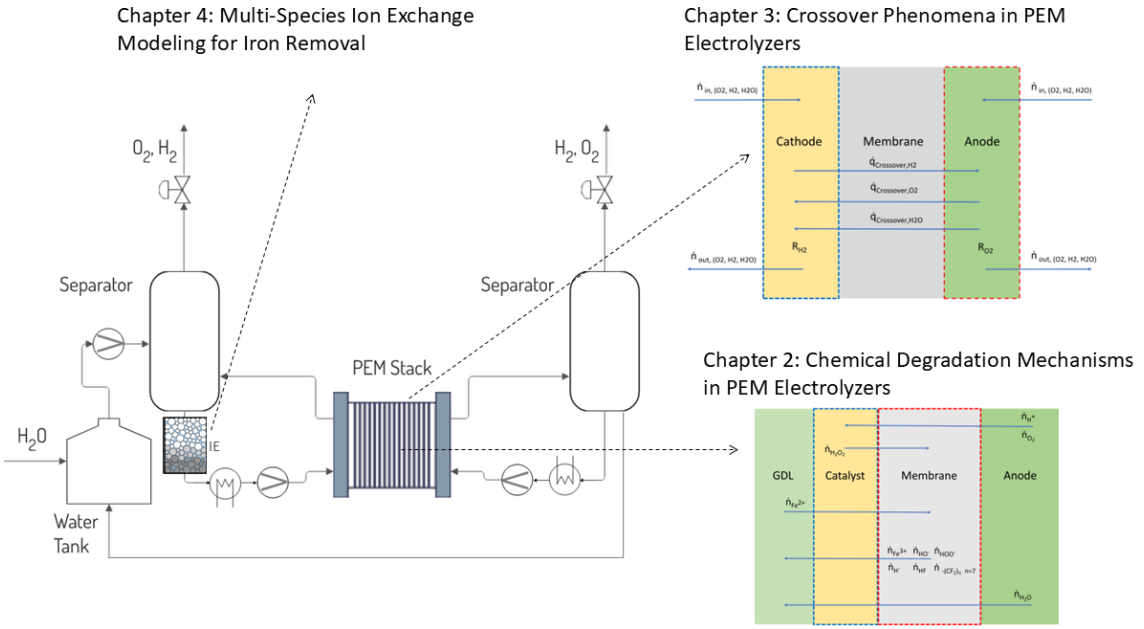

Figure 1.1.: Schematic representation of a PEM electrolyzer indicating the physical domains addressed by the modeling approaches developed in this dissertation. Chapter 2 focuses on chemical membrane degradation processes within the membrane and catalyst layers. Chapter 3 addresses hydrogen and oxygen crossover across the membrane between anode and cathode compartments. Chapter 4 investigates ion exchange systems integrated into the anode stream for the removal of dissolved iron impurities.

2. Chemical Degradation Mechanisms in PEM Electrolyzers

2.1. Introduction

Following the motivation and scope outlined in Chapter 1, this chapter focuses on chemical degradation of the polymer electrolyte membrane as a key durability limitation in PEM electrolyzers. Chemical membrane degradation is a dynamic process that evolves over the lifetime of an electrolyzer and can ultimately lead to irreversible loss of membrane function [23]. In the present work, we restrict the scope to chemical degradation. Under the fully hydrated, high-potential conditions of PEM electrolyzers, radical-induced chemical attack on the membrane is a particularly relevant degradation pathway, whereas mechanical and thermal degradation are governed by different driving forces and require separate, specialized model formulations [24]. The chapter develops a dynamic model-based description of the degradation mechanism and uses it to analyze operating-condition effects on the fluoride release rate (FRR) and membrane lifetime.

Chemical membrane degradation is mainly affected by (*i*) temperature, (*ii*) oxygen (O_2) crossover from the anode to the cathode side, and (*iii*) the flux of ferrous ions (Fe^{2+}) from corroding cell and balance-of-plant components into the membrane [11]. Oxygen crossover causes hydrogen peroxide (H_2O_2) formation at the cathode catalyst layer. H_2O_2 diffuses into the membrane and forms radicals that degrade the polymer. This mechanism, known as the Fenton reaction, is accelerated by Fe^{2+}. These radicals attack the side chains and backbone of the PFSA polymer, causing chain scission and fluoride release. This progressively thins the membrane, raises gas crossover and ohmic resistance, and can ultimately lead to pinhole formation and membrane failure. Thus, the diffusion of H_2O_2 and the influx of Fe^{2+} collectively contribute to membrane degradation and limit the lifetime of PEM electrolyzers [24].

The desire to increase electrolyzer lifetime motivates the prediction of operating-condition effects on chemical membrane degradation and an improved understanding of the underlying mechanism. Several previous works have taken a model-based approach to analyze degradation, using the fluoride release rate (FRR) as an indicator. These models range from fundamental kinetic models, which provide a microscopic view of degradation reactions, to cell-level models, which combine kinetics with species transport and provide a macroscopic view.

The scientific community initially focused on fuel cell models. Shah et al. [13] developed a 1D time-dependent fuel cell model incorporating transport phenomena, H_2O_2 formation, and radical generation. The model includes side-chain cleavage and backbone unzipping as degradation pathways and considers three reaction domains: anode, cathode, and membrane.

Building on Shah et al., Gubler et al. [9] developed a 0D (lumped) fuel cell degradation

model that includes a more detailed radical mechanism. In contrast to the three-domain structure of Shah et al., all reactions take place in the membrane. Gubler et al. report a hydroxyl radical ($^{\bullet}OH$) formation rate five orders of magnitude lower than that of Shah et al. and attribute this to different assumptions regarding the Fe^{2+}/Fe^{3+} ratio.
Ghelichi et al. [14] introduced a more detailed PFSA degradation approach by dividing the membrane structure into headgroup, trunk, and backbone segments and modeling the degradation of each. This approach improved the mechanistic understanding of membrane degradation. Coms [25] proposed a fuel cell degradation model focusing on sulfonyl radical formation via peroxide intermediates, which dominates under dry, low-humidity fuel cell conditions.
While fuel cell models provide valuable insights, PEM electrolyzers operate under fully hydrated conditions and at higher potentials [6, 26]. These conditions suppress sulfonyl-radical formation and increase hydroxyl radical formation [27], leading to degradation pathways that differ from fuel cells and require dedicated electrolyzer-specific models.
Frühwirt et al. [28] recently presented the most comprehensive lumped kinetic PFSA degradation model to date, combining 23 reactions into a complete cause-and-effect chain. Their model simulates PFSA degradation over time using FRR as an indicator and shows good agreement with experimental data. Importantly, the model of Frühwirt et al. emphasizes the role of hydroxyl radicals , which are more relevant under the fully hydrated and high-potential conditions typical of PEM electrolyzers, making this model the most suitable basis for our study.
Chandesris et al. [11] developed a 1D PEM electrolyzer model incorporating chemical degradation based on the Gubler kinetics and an O_2 crossover and H_2O_2 formation mechanism, considering the cathode catalyst layer as only reaction domain. Their simulated FRR showed good agreement with experimental data. Frensch et al. [15] extended this model with additional reactions and experiments, confirming that FRR is strongly influenced by Fe^{2+} and H_2O_2 concentrations.
In summary, existing PEM electrolyzer cell-level models build upon chemical degradation mechanisms and combine them with transport phenomena, but they do not account for the dynamic PFSA degradation process as in the model of Frühwirt et al. [28] or incorporate the influence of pressure on degradation, except in the conference contribution by Eckert et al. [29]. Furthermore, previous PEM electrolyzer models assume that all reactions occur in the cathode catalyst layer, whereas the latest kinetic degradation models are formulated for the membrane domain.
To bridge this gap, we propose a dynamic lumped cell-level model of chemical membrane degradation in PEM electrolyzers. We incorporate the dynamic PFSA degradation mechanism of Frühwirt et al. [28] and investigate key parameters that influence degradation, including pressure. The model includes two reaction domains: the membrane, where degradation occurs, and the cathode catalyst layer, where H_2O_2 is formed. Because chemical membrane degradation exhibits a long quasi-steady-state phase and experimental data often come from this regime, we employ a pseudo-steady-state approach (PSSA) to facilitate parameter estimation. This approach is also used to analyze the influence of current density and water flow on the FRR, while time-dependent simulations are used to study the full degradation dynamics.
The remainder of this chapter is structured as follows: First, the model is described in detail, including all equations. Then the results are discussed, starting with parameter estimation and validation, followed by the influence of current density, water flow, and

pressure on FRR, the time-dependent FRR simulations, and the lifetime estimation. Finally, conclusions and potential future work are presented.

2.2. Model Description

In the following, we describe the proposed dynamic lumped cell-level model, which combines three literature models. The proposed model is implemented with Aspen Custom Modeler (AspenTech, Version 14.3), and all equations and parameters (see Table 2) are explained below. Aspen Custom Modeler was chosen because it allows the formulation of stiff DAE systems with user-defined reaction networks and supports both steady-state and fully dynamic simulations in one environment, which is required for the combination of PSSA-based parameter estimation and long-term degradation simulations in this work. Aspen Properties was not used; instead, all thermophysical parameters (such as densities, solubilities, and humidification-dependent proton concentration) were taken directly from the literature and are listed with their sources in Tables 1 and 2.
The model combines the extended kinetic reaction model proposed by Frühwirt et al. [28], which outlines the complete time-dependent cause-and-effect chain of membrane degradation, with the H_2O_2 formation mechanism from the work of Chandesris et al. [11] and the oxygen crossover mechanism from the work of Trinke et al. [30]. The original reaction model proposed by Frühwirt et al. was formulated for a batch experiment, where degradation of a piece of membrane material in a beaker cell was investigated. For the present work, we adapt it to a cell-level model of an electrolysis cell that includes the transport of water across the membrane. This inclusion is important because it accounts for the washout of reaction products, ions, and reactants. In addition, the model is further enhanced by integrating a semi-empirical oxygen crossover model developed by Trinke et al. [30] that accounts for two key operating parameters: pressure and current density. These parameters significantly affect the oxygen crossover rate, which in turn affects the production rate of H_2O_2, and thus the overall degradation process.
A schematic representation of the dynamic lumped cell-level model developed in this work is given as an overview in Figure 2.1. The model considers two reaction systems: the membrane and the cathode catalyst layer, both modeled as concentrated systems.
In the cathode catalyst layer, only the formation of H_2O_2 is considered, under the assumption that it diffuses into the membrane and is involved in reactions to form radicals. Although radicals may be also formed at the catalyst, they are expected to have such short lifetimes that the diffusion length is much smaller than the thickness of the membrane. This assumption is largely supported by the results shown by Gubler et al. [9]. It is assumed that all of the O_2 transported from the membrane to the cathode catalyst layer is entirely converted to H_2O_2, since this is the dominant reaction pathway in the catalyst and the formation of water can be neglected (as shown below). It is also assumed that all the H_2O_2 produced in the catalyst layer is completely transferred to the membrane. This is a conservative assumption, since in reality there will be less H_2O_2 inside the membrane causing chemical degradation.
In the membrane, the entire degradation mechanism of Frühwirt et al. [28] is considered. In addition, the washout of ions and degradation products by the transfer water flow from the anode to the cathode is included. However, the primary membrane components, such as sulfonic acid headgroups (–SO_3H), side chains, and backbone structure, are not washed out due to their size and interconnection (as shown below). In the following, we describe the occurring reactions and transport processes in more detail.

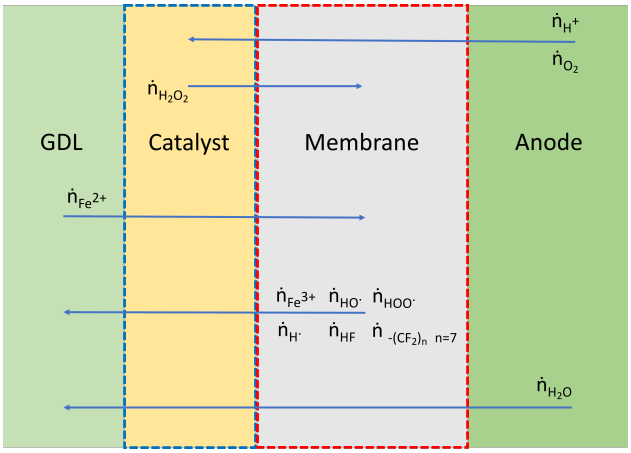

Figure 2.1.: Schematic of the PEM electrolyzer membrane degradation model. The reactions occur in two reaction systems (cathode catalyst and membrane). The species H^+ and O_2 are transported from the anode to the cathode catalyst and Fe^{2+} is transported from the GDL to the membrane. The formed H_2O_2 is transported from the cathode catalyst to the membrane. The reaction products inside the membrane are washed out towards the GDL by H_2O that flows from the anode through both reaction systems to the GDL.

2.2.1. Hydrogen Peroxide Formation

The model of hydrogen peroxide formation is based on the work of Chandesris et al. [11]. At the cathode catalyst layer, H_2O_2 is formed through the 2-electron oxygen reduction reaction (ORR)

$$O_2 + 2\,H^+ + 2\,e^- \longrightarrow H_2O_2. \tag{2.1}$$

The potential on the cathode side is low, more specifically negative compared to the standard hydrogen electrode (SHE). Under these conditions, Reaction (2.1) becomes dominant over the 4-electron ORR

$$O_2 + 4\,H^+ + 4\,e^- \longrightarrow 2\,H_2O, \tag{2.2}$$

and thus the latter can generally be neglected [11].
The electrochemical reaction rate of H_2O_2 is calculated based on third-order kinetics [11]: $R_{H_2O_2} = k_1\, c_{O_2}\, c_{H^+}^2$. The concentration in the ionomer phase of the catalyst c_{H^+} is a result of the membrane properties:

$$c_{H^+} = \frac{\rho_m + 32.4\,\lambda}{(1 + 0.0648\,\lambda)\,EW_0}, \tag{2.3}$$

where ρ_m is the density of the PFSA membrane and EW_0 the equivalent weight. The proton concentration c_{H^+} depends on the degree of humidification λ of the membrane [31]. The rate constant k_1 related to the 2-electron ORR (2.1), which is defined per unit of the electrochemically active surface area, is given by the following equation [11]:

$$k_1 = k_0 \exp\left(\frac{-\Delta H_{H_2O_2}}{R\,T}\right) \exp\left(\frac{-\alpha_{H_2O_2}\,F}{R\,T}\eta_{2e}\right), \tag{2.4}$$

where $\alpha_{H_2O_2}$ is the transfer coefficient and η_{2e} the cathodic overpotential, with the equilibrium potential set to be 0.695 V compared to the SHE. The activation energy for the

electrochemical reaction is denoted as $\Delta H_{H_2O_2}$. The pre-exponential factor k_0 is taken from the work of Sethuraman et al. [32].
Given the reaction rate per electrochemical surface area, $R_{H_2O_2}$, the formation rate of H_2O_2 per volume of the catalyst is computed as $r_1 = \frac{R_{H_2O_2}\,\gamma_C}{d_{\text{catalyst}}}$, where γ_C is the rugosity of the cathode electrode and d_{catalyst} the thickness of the cathode catalyst layer [11].

2.2.2. Oxygen Crossover

Trinke et al. [30] formulated a semi-empiric equation for oxygen crossover that considers a supersaturation effect of O_2 at the anode side. It computes the O_2 flux at the membrane-cathode interface as

$$q_{O_2,\text{mem}} = \frac{n_{\text{drag}}\, i\, p^{\text{A}}_{O_2}\, S_{O_2}\, s_{\text{sat}}}{\frac{F\,\rho_{H_2O}}{M_{H_2O}}}, \tag{2.5}$$

where n_{drag} is the drag coefficient, i the current density and $p^{\text{A}}_{O_2}$ the partial pressure of O_2 at the anode. S_{O_2} is the O_2 solubility in water and s_{sat} the supersaturation factor.
Here, the original crossover correlation of Trinke et al. [30] is used; an improved oxygen crossover model, validated against large-scale high-pressure experiments, is developed in Chapter 3.

2.2.3. Degradation Mechanism

In the degradation process of PFSA membranes, radicals target multiple structural points: Carboxylic acid (–COOH) end groups and tertiary carbons within the main chain, sulfonic acid headgroups (–SO_3H), ether groups and tertiary carbons within the side chain [33]. The complete main- and side-chain degradation mechanism is implemented as described by Frühwirt et al. [28] in Table 1. The reaction rates r_i are calculated using the equations described in Table 1 with Arrhenius-type temperature dependence for the reaction rate coefficient k_i:

$$k_i = A_i\, \exp\left(-\frac{E_{\text{act,i}}}{R\,T}\right), \tag{2.6}$$

where the parameters A_i and $E_{\text{act,i}}$ are given in Table 1 and were determined experimentally by several authors and collected by Frühwirt et al. [28].
To calculate the concentration of species j in the membrane, the following general approach is used:

$$\frac{dc_j}{dt} = \sum_i (\nu_{j,i}\, r_i) + \frac{q_{j,\text{in}}}{d_{\text{membrane}}} - \frac{q_{j,\text{out}}}{d_{\text{membrane}}}, \tag{2.7}$$

where $\nu_{j,i}$ is the stoichiometric factor, d_{membrane} the thickness of the membrane, and $q_{j,\text{in}}$ and $q_{j,\text{out}}$ describe species entering and leaving the membrane, respectively. The only two species that enter the membrane and take part in the reactions there, in accordance with our assumptions, are Fe^{2+} and H_2O_2, so $q_{j,\text{in}}$ is non-zero for these species (see Figure 2.1). To calculate $q_{H_2O_2,\text{in}}$, the H_2O_2 formation rate r_1 in the cathode catalyst is multiplied with the catalyst thickness d_{catalyst}, whereas $q_{Fe^{2+},\text{in}}$ is used as fitting parameter (as shown below). The outgoing molar fluxes $q_{j,\text{out}}$ are due to washout and are calculated as

$$q_{j,\text{out}} = c_j\, v_{H_2O}, \tag{2.8}$$

where v_{H_2O} is the velocity of the water flowing from the anode to the cathode. The side chain and backbone structures of the membrane (-SO_3H, SC-$O^\bullet$ and BB-$O^\bullet$) are linked together and therefore do not go with the water, but their degradation products do.
This approach, derived from Chandesris et al. [11], simplifies the behavior of water and species within the membrane, treating water similarly to bulk water in terms of solvation and ion transport under the highly hydrated conditions typical of PEM electrolyzers.
Equation (2.8) reflects this simplification, consistent with Chandesris et al.'s model. Although water in the membrane acts more as a solute in the ionomer phase, and a full phase equilibrium for all species isn't modeled due to a lack of specific data, this approach effectively captures the essential aspects of membrane degradation under the operational conditions of PEM electrolyzers.
We note that membrane proton conductivity is not part of the present model formulation, as no cell voltage or ohmic-loss model is included; the time evolution of SO_3H groups is therefore used exclusively within the chemical degradation mechanism.

2.2.4. Water Flow

In the model, temperature and pressure are spatially uniform and the water supply to both half-cell chambers is equal, with electro-osmosis being the primary factor in water transport across the membrane: The movement of H^+ ions from the anode to the cathode results in the "dragging" of multiple water molecules. As water is consumed on the anode side, a gradient could be developed that leads to back diffusion of water from the cathode to the anode side as an opposing effect. The combination of both effects leads to the volumetric flow rate $Q^t_{H_2O}$ of the transfer water, which is calculated by using a semi-empirical formulation derived by Chandesris et al. [11]:

$$Q^t_{H_2O} = \left(-0.322 \log\left(\frac{i}{\mathrm{A\ cm^{-2}}}\right) + 5.59\right) Q^c_{H_2O}, \tag{2.9}$$

where $Q^c_{H_2O}$ is the volumetric flow rate of the water consumed in the reaction to H_2 and O_2:

$$Q^c_{H_2O} = \frac{M_{H_2O}\, i\, A}{2\, F\, \rho_{H_2O}} \tag{2.10}$$

The velocity v_{H_2O} is derived from the net flow of water through the membrane:

$$v_{H_2O} = \frac{Q^t_{H_2O}}{A} \tag{2.11}$$

It is important to note that no pressure-driven water transport term is included. In the present model, both half-cell chambers are operated at equal pressure, and therefore no trans-membrane pressure difference exists that could induce additional water flux. As a result, the transferred water flow varies only through its dependence on current density via the empirical correlation of Chandesris et al. [11], which captures the combined effects of electro-osmotic drag and back-diffusion under electrolyzer operating conditions.

2.2.5. Pseudo-Steady State Approach

After setting up the model, we use the PSSA to make parameter estimation and validation with experimental steady-state data points more computationally tractable.

Our results of the time-dependent simulations show that there is a long plateau period of the FRR (see Figure 2.2). The motivation for PSSA is that (a) we suspect that experimental data of Chandesris et al. [11] is conducted during this plateau period or close to it, since the largest increase in FRR is during the first 200-300 hours of the simulation, and (b) that with PSSA we can introduce a (pseudo-)steady state for the FRR in the plateau region, which can then be conveniently be located via the steady-state mode of Aspen Custom Modeler. Consequently, by capturing this pseudo-steady state behavior - where the FRR levels off without being affected by the whole depletion of the membrane structure - we enable application of the parameter estimation algorithm in steady-state mode to fit the model to experimental data.
To capture the plateau regime without long transients during parameter estimation, we enforce PSSA by treating the rate of the first reaction step in the degradation mechanism as a constant during the steady-state fitting runs. This first reaction step is Reaction 14 in Table 1, which describes the attack of $^{\bullet}$OH radicals on the SC–SO_3H headgroup. It represents the initiation of the degradation chain and is comparatively slow, and therefore governs the build-up of downstream intermediates. For the steady-state fitting runs, only the rate of Reaction 14 is held constant; all other reactions, species balances, and washout terms remain fully dynamic.
This produces a (pseudo-)steady FRR near the plateau while all downstream reactions and washout terms remain active. Consequently, the long plateau observed in the dynamic model is represented as a steady state close to its maximum, which is suitable for parameter estimation with steady-state experimental data (see Figures 2.2 and 2.7).
By using PSSA, we are able to run simulations in Aspen Custom Modeler's steady-state mode, so we can vary certain parameters such as pressure or water flow rate and compare the results (as shown below). However, we do not use the PSSA for time-dependent simulations. For these simulations, we use the model without the PSSA applied and run them using the dynamic mode of Aspen Custom Modeler (as shown below). In such simulations, the full complexity of the system, including the time-dependent consumption of reactants, is taken into account.

2.2.6. Fluoride Release Rate & Parameter Estimation

The resulting FRR (R_{FRR}), which is a measure of the intensity of degradation, can be determined by summing the fluoride formation rates of the individual reactions (cf. Table 1, R 15 - 23) and then multiplying this aggregated rate by the membrane thickness d_{membrane}.
The FRR is fitted to the experimental data of Chandesris et al. [11] by using the Aspen Custom Modeler least squares algorithm. In line with other literature, the Fe^{2+} flux $q_{\mathrm{Fe^{2+},in}}$ is taken as the fitting parameter, since experimentally determined literature values for this flux are inconsistent or not available [15].
Chandesris et al. [11] proposed three source term models for the Fe^{2+} flux: constant flux, current-density dependent flux and temperature-dependent flux. The current-density dependent model deviated from the experimental data, unlike the other two, as confirmed by the simulations in this work.
Consistent with previous PEM electrolyzer degradation models [11, 15], we fit a constant Fe^{2+} source term ($q_{\mathrm{Fe^{2+},in}}$). In a lumped (0D) formulation, FRR is governed by Fe^{2+} availability rather than its net direction of ingress, so we do not analyze directionality further.

2.3. Results & Discussion

2.3.1. Parameter Estimation & Validation

In this subsection, we focus on the parameter estimation and validation of the dynamic lumped cell-level model of chemical membrane degradation. First, the use of the PSSA is motivated. Then the model is used for the parameter estimation. The estimation aims to align the FRR (R_{FRR}) simulation results with the experimental data presented by Chandesris et al. [11]. Table 2 details the parameter values used for the model, including the estimated parameter value $q_{\mathrm{Fe^{2+},\,in}}$. This estimated value is subsequently set as a parameter for all succeeding simulations.

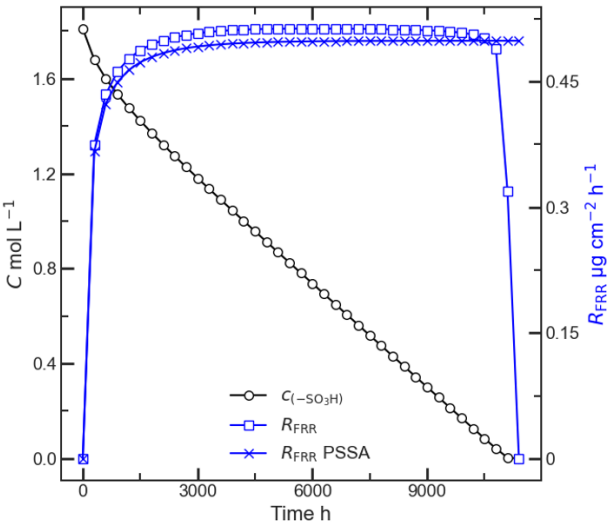

Figure 2.2.: Time-dependent evolution of (-SO_3H) headgroup concentration without PSSA applied and comparison of FRR with (R_{FRR} PSSA) and without PSSA (R_{FRR}) applied over operating hours. The FRR increases sharply at the beginning and develops a long plateau for several thousand hours for both simulations before the FRR drops sharply to zero for the simulation without PSSA. With PSSA, the FRR reaches a steady state that closely approximates the plateau.

In the simulation without the application of PSSA, the initial reactant (-SO_3H) experiences a steady decrease over time, while the FRR approaches its maximum within the first quarter of the total run time (see Figure 2.2). For instance, over the first 1000 operational hours, the (–SO_3H) concentration reduces from 1.81 to 1.51 $\mathrm{mol\,L^{-1}}$, while the FRR shows a steep increase from 0 to 0.4 $\mathrm{\mu g\,cm^{-2}\,h^{-1}}$. Over the next approximately 10500 operational hours, the FRR concentration remains relatively constant, despite a gradual decrease in the (-SO_3H) headgroup concentration. This constant level of FRR is maintained until all (-SO_3H) and its subsequent products are exhausted, at which point there is a rapid drop in the FRR concentration to zero.
In comparison, in the simulation with the application of PSSA, the initial reactant (-SO_3H) is constant and does not change its value, whereas the FRR approaches its maximum within the first quarter of the total run time (see Figure 2.2) similar to the other simulation. The difference is that the FRR levels off and reaches a steady state, without a rapid drop in the FRR concentration to zero.

When the two simulations are compared, the maximum values of both simulations are close to each other (see Figure 2.2), so the error introduced by this approximation is small and justifies the use of the PSSA. Since we suspect the experimental FRR data comes from or near this plateau period, we use the PSSA to fit our model and to characterize what happens for the longest period of degradation.
Using the PSSA, the simulated (pseudo-)steady state FRR is fitted to the available (pseudo-)steady state experimental data points, which represent average FRR values over a range of time intervals. In the model, $q_{Fe^{2+},in}$ is the only fitting parameter (as shown above).
The parameter estimation simulation results shown in Figure 2.3a were obtained using the PSSA integrated model adjusted to a cell temperature of 333 K, which is consistent with the experimental data and is a practical operating temperature. Additionally, we validated our model at a higher temperature of 353 K, as shown in Figure 2.3b, to compare its performance with the experimental data and simulation results from Chandesris et al. [11]. The root mean square (RMS) error at 333 K at the optimal solution is $0.1\,\mu g\,cm^{-2}\,h^{-1}$.

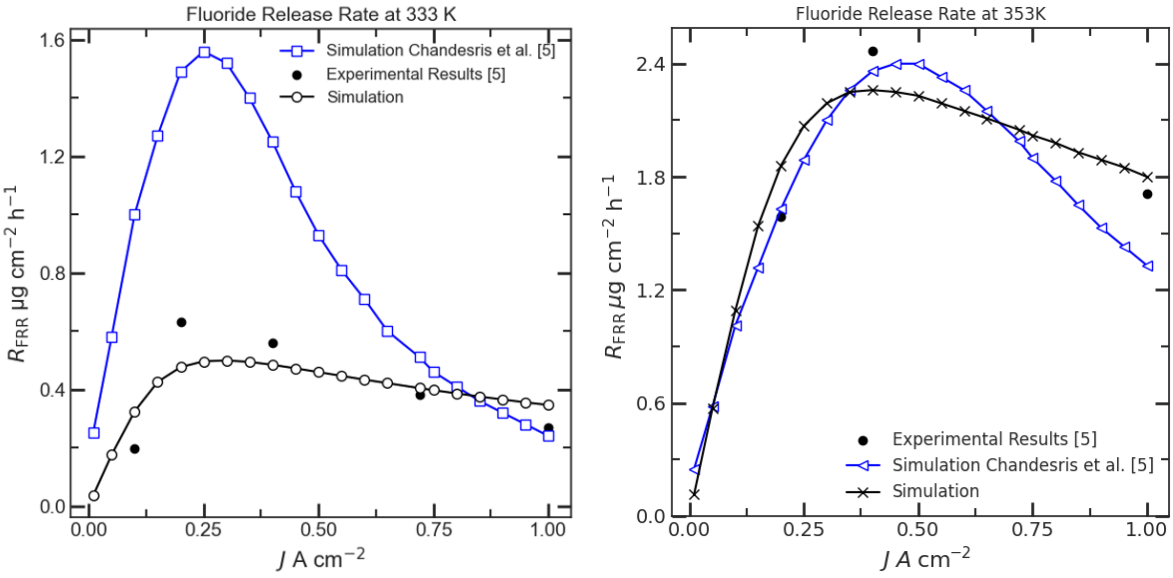

(a) 333 K **(b)** 353 K

Figure 2.3.: Comparison of fitted model output with experimental and simulation results from Chandesris et al. [11] at different temperatures: (a) 333 K and (b) 353 K. The Fe^{2+} flux was used as a fitting parameter to achieve a reasonable agreement between the model and the experimental data.

Starting at a current density of $0\,A\,cm^{-2}$, the degradation rate increases from low current density up to a peak near $0.3\,A\,cm^{-2}$, then decreases more gradually. The fitted model accurately reflects this qualitative behavior of the FRR. Compared to the simulation by Chandesris et al. [11], our model achieves a closer fit to experimental data. Chandesris et al. based their electrolyzer cell-level model on the degradation kinetics of Gubler et al. [9], extended with O_2 crossover and H_2O_2 formation, and assumed all reactions take place in the cathode catalyst layer. In contrast, our model embeds the more detailed hydroxyl-radical network of Frühwirt et al. [28] directly in the membrane rather than using the carboxylic-acid–centered scheme emphasized by Ghelichi et al. [14]. This choice reflects fully hydrated electrolyzer conditions. By calculating the RMS error from the graphical

results of Chandesris et al., we find their relative RMS error at 353 K to be about 0.1538, closely matching our relative RMS error of 0.1562 at 333 K. This demonstrates that our model's performance at a lower, more practical temperature is comparable to their model's performance at a higher temperature.

2.3.2. Analysis of Current Density and Water Flow Impact on FRR

The experimental data in Figure 2.3a shows that FRR initially increases with increasing current densities, peaking at about $0.3\,\mathrm{A\,cm^{-2}}$ for 333 K, and then decreases at a slower rate. This pattern of FRR with respect to current density inspired a more in-depth analysis to better understand the driving forces behind this unusual shape.

Chandesris et al. [11] presented a fundamental investigation of the relationship between current density and FRR. Their work revealed the distinct nonlinear trend in FRR as a function of current density shown in Figure 2.3a. They attributed their findings to the interplay of various electrochemical reactions and their subsequent impact on the dynamics of $^{\bullet}OH$ in the system. Their explanation for this pattern is that it results from the balance between reactions that generate $^{\bullet}OH$ radicals and those that consume them. At very low current densities, a reaction that consumes most of the $^{\bullet}OH$ becomes dominant, resulting in reduced fluoride release. At high current density, they suggest that the decrease in fluoride release is due to the decrease in the molar percentage of O_2 and thus the H_2O_2 formation. However, they did not examine the potential impact of increased water flow resulting in greater washout of radicals and reaction products, especially at higher current densities.

Extending the basic findings of Chandesris et al, our study further examines the pattern of the FRR curve. We focus on the influence of water flow velocity on the degradation dynamics and the resulting washout of Fe^{2+} ions, H_2O_2, and $^{\bullet}OH$. Based on our simulation results, our interpretation is as follows: As the current density increases, the water flux across the membrane also increases due to electro-osmotic drag. This increased water flux concurrently leads to an increased transport of O_2 molecules through the membrane. Consequently, there is a higher production of H_2O_2, as shown in Figure 2.4a. The increased concentration of H_2O_2 in combination with Fe^{2+} ions leads to an increased formation of $^{\bullet}OH$ radicals, which enhance membrane degradation by participating in the reactions that degrade the membrane and release the fluoride.

However, the increased water flux at higher current density also leads to more H_2O_2, Fe^{2+} and $^{\bullet}OH$ being washed out of the membrane and cathode catalyst layer. This causes the Fe^{2+} concentration to stabilize due to the diffusion-limited supply of Fe^{2+} ions (see Figure 2.4a vs. 2.4b). This limitation leads to the fact that fewer $^{\bullet}OH$ radicals are formed, and a maximum point is reached beyond which the washing out is greater than the new formation, and thus, the $^{\bullet}OH$ concentration decreases again as current density increases further.

In summary, at higher current densities, the degradation rate decreases due to two factors: (*i*) the decrease in Fe^{2+} ion concentration due to its increased consumption and limited supply, and (*ii*) the increased water flow through the membrane and thus more significant washout of Fe^{2+} ions, H_2O_2, and $^{\bullet}OH$.

In order to confirm whether the washing-out of species through the increased water flux indeed determines the observed shape of H_2O_2 and Fe^{2+}, and $^{\bullet}OH$ concentration as function of current density, we conducted simulations in which the water flux was artificially fixed to

a constant value (see Figures 2.4c and 2.4d). With such a constant water flux, no maximum point of the $^{\bullet}OH$ concentration is observed (see Figure 2.4d), but the concentration keeps increasing with increasing current density. This provides further evidence that the washing out of H_2O_2, Fe^{2+} and $^{\bullet}OH$ is indeed a primary factor contributing to the decline of $^{\bullet}OH$ concentration observed in Figure 2.4b.
Overall, the reaction network in Table 1 shows distinct dominant steps depending on operating conditions. At low current densities, reactions consuming $^{\bullet}OH$ (such as R3 and R7) limit the availability of radicals, resulting in low FRR. At intermediate current densities, the combination of elevated H_2O_2 levels and sufficient Fe^{2+} supply promotes $^{\bullet}OH$ formation through R1, leading to the observed FRR maximum. At higher current densities, increasing water flux enhances the washout of H_2O_2, Fe^{2+}, and $^{\bullet}OH$, while Fe^{2+} availability becomes diffusion-limited, which suppresses further radical formation. These mechanistic insights suggest potential mitigation strategies such as minimizing Fe^{2+} ingress from hardware corrosion, reducing H_2O_2 formation or crossover, or introducing radical scavengers to suppress $^{\bullet}OH$ generation from R1.

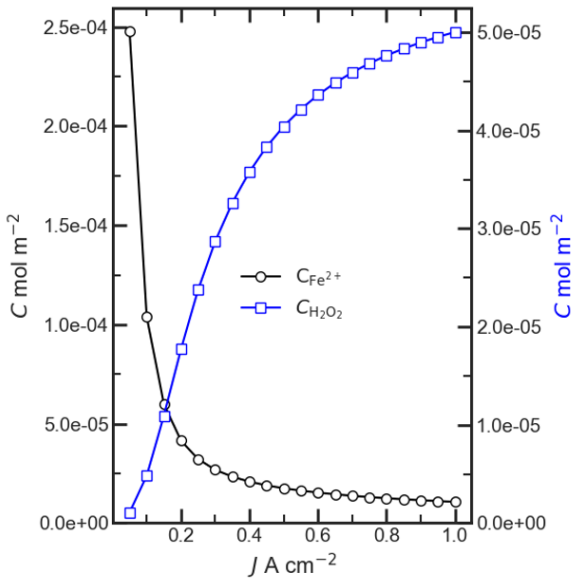

(a) Simulation of the concentration of H_2O_2 and Fe^{2+} in the membrane with a current density dependent water flow rate.

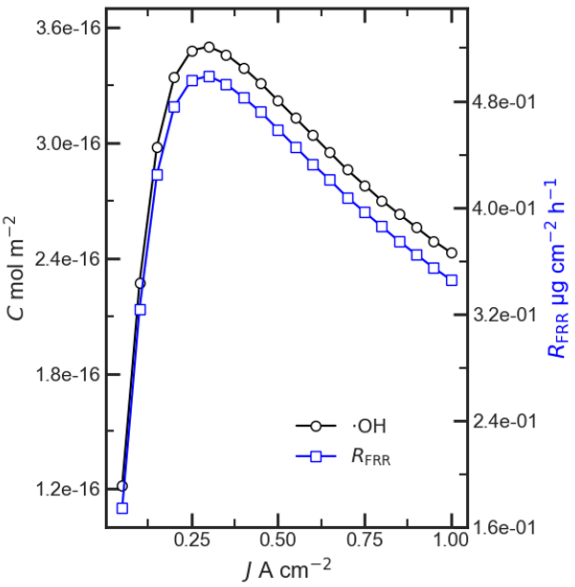

(b) Simulation of the concentration of •OH and FRR in the membrane with a current density dependent water flow rate.

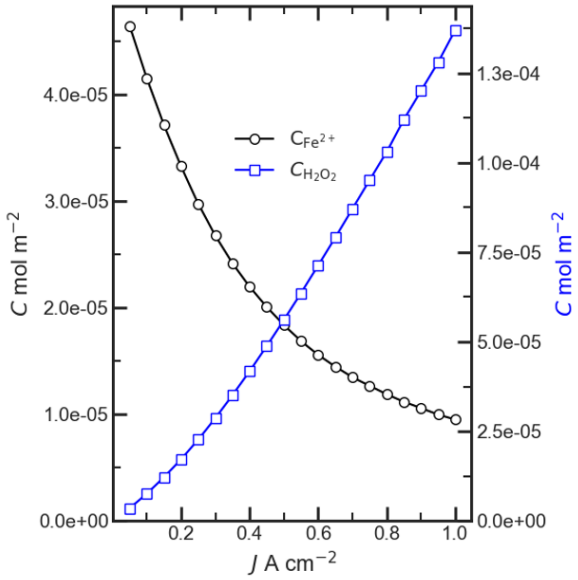

(c) Simulation of the concentration of H_2O_2 and Fe^{2+} in the membrane at fixed water flow rate ($v_{H_2O} = 0.005\,8\,\mathrm{m\,h^{-1}}$). Note the different scale of the y-axes compared to Figure 2.4a.

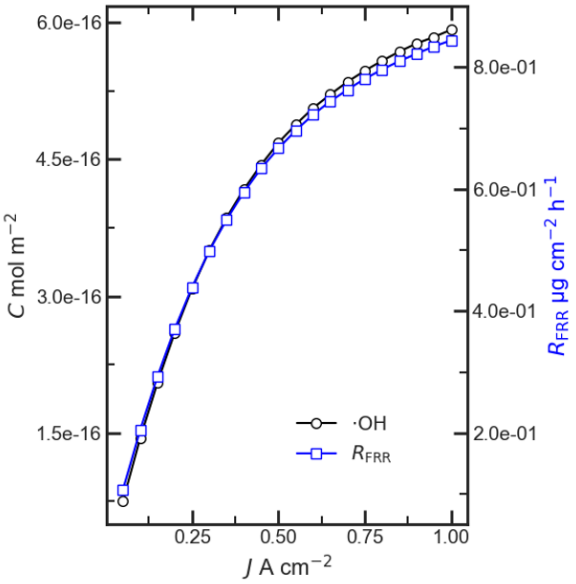

(d) Simulation of the concentration of •OH and FRR in the membrane at fixed water flow rate ($v_{H_2O} = 0.005\,8\,\mathrm{m\,h^{-1}}$).

Figure 2.4.: PSSA simulations comparing current density dependent and fixed water flow effects on species concentrations and FRR in the membrane.

2.3.3. Influence of Pressure on the FRR

A second factor affecting the FRR (besides the current density) is the partial pressure of O_2 in the anode chamber, which in turn is determined by the overall operating pressure.

Existing degradation models are not suitable to investigate this aspect, since they use a fixed H_2O_2 concentration or oxygen flux, thereby not incorporating the impact of changes in O_2 flux across the membrane affected by the O_2 partial pressure in the anode chamber. In contrast, our model includes the oxygen crossover equation of Trinke et al. [30], which considers the pressure as a parameter to be used in the calculation of the O_2 partial pressure and is validated by experiments.

We analyzed the relationship through a series of steady-state simulations, as shown in Figure 2.5. As discussed in the previous section, the simulation at a current density of $0.5\,\mathrm{A\,cm^{-2}}$ has the highest fluoride release values.

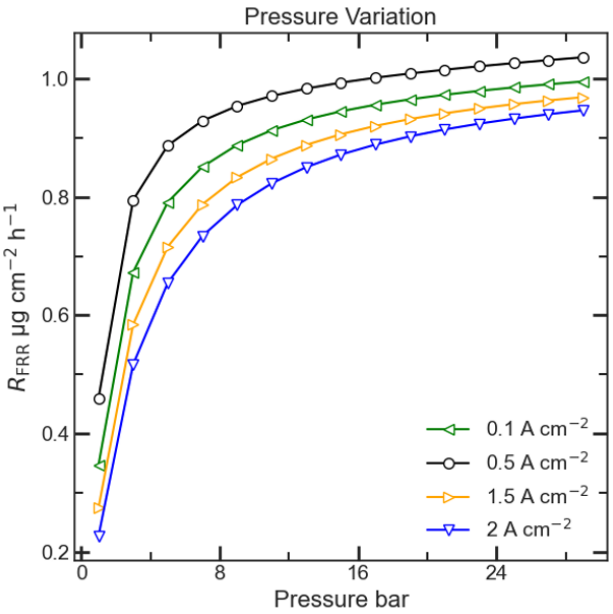

Figure 2.5.: PSSA - Simulation of the Fluoride Release Rates by Variation of the Pressure. Greatest degradation occurs at intermediate current densities around $0.5\,\mathrm{A\,cm^{-2}}$. After a steep increase of the FRR with increasing pressure, it levels off starting at around 6 bar.

As the pressure is increased from 1 bar to 29 bar, the FRR increases steeply for all curves up to a point where the increase in FRR slows. From the shape of the curves, it can be concluded that pressure changes in the low-pressure range influence the evolution of the FRR more than in the higher-pressure range. Increased pressure leads to increased dissolution and subsequent transport of O_2 across the membrane to the cathode. As a result, the rate of H_2O_2 formation in Reaction (2.1) is influenced by the O_2 concentration at the membrane-catalyst interface, which is directly affected by changes in pressure. Because H_2O_2 is the primary reactant in the Fenton reaction, the concentration of H_2O_2 affects the degradation and, thus, the rate at which fluoride is released. However, this increase in FRR levels off at higher pressures. This flattening effect is likely due to the Fe^{2+} flux remaining unchanged despite variations in pressure, thereby limiting further increases in FRR.

2.3.4. Time-Dependent FRR Simulations at Various Current Densities

To understand the dynamics of chemical membrane degradation at different operating conditions, we conducted time-dependent simulations with our dynamic model (see Figure 2.6).
The initial 500 hours of the simulation show a rapid increase in the FRR for all applied current densities, with the maximum rate being highest at intermediate current densities ($0.5\,\mathrm{A\,cm^{-2}}$), consistent with the previous section observation. Between 500 and 1000 hours, the FRR increase slows down and finally becomes approximately constant after 4500 hours. The slopes of the curves are steeper at intermediate current densities and gradually decrease as they approach the maximum value.
Each curve reaches a plateau, and in order to understand this behavior we re-examine the reaction system. According to the degradation mechanism proposed by Frühwirt et al. [28], degradation starts at the side chain headgroups (-SO_3H), as shown in Reaction 14 (see Table 1). This reaction produces the subsequent side chain degradation intermediate SC-$O^\bullet$, but does not itself release any HF per molecule of reactant. In contrast, the degradation of SC-$O^\bullet$ contributes significantly to the release of HF per molecule of reactant, as seen in Reaction 15 in Table 1. Initially, the concentration of headgroups is high and the concentration of side chains is low; over the course of the reaction, the concentration of headgroups decreases and the concentration of side chains increases. The increase in side chain concentration is highest at the beginning and slows down until an equilibrium is reached, as these side chain structures are simultaneously consumed during degradation and a balance between the rate of new side chain formation and its consumption is reached. As this equilibrium is gradually approached, it manifests itself in the FRR plot as a maximum point that is slowly approached, providing a plausible explanation for the observed curve.
The simulation results suggest that the time scale for reaching the maximum FRR is in the thousands of hours, and the steepest increase of the FRR is in the hundreds of hours. This could have important implications for the operation of PEM electrolyzers: It would mean that short-term operation at current densities near the degradation maximum at intermediate current densities around $0.5\,\mathrm{A\,cm^{-2}}$ would not significantly affect chemical membrane degradation, as long as the electrolyzer is not operated at these conditions for longer periods.

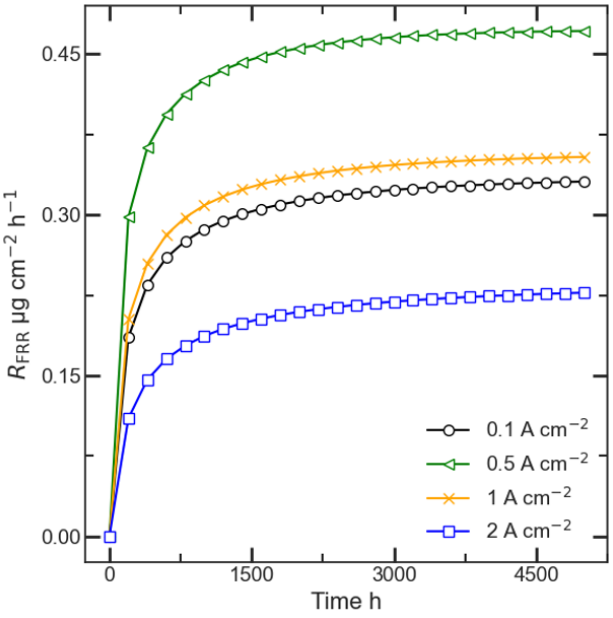

Figure 2.6.: Time-dependent simulation of FRR at different current densities. Greatest degradation occurs at intermediate current densities around $0.5\,\mathrm{A\,cm^{-2}}$, and it takes more than 1000 hours to reach maximum FRR.

2.3.5. Lifetime Estimation of PEM

Predicting membrane lifetime is of importance for operational planning, safety considerations, and cost-effectiveness. Using the dynamic model, which includes the complete cause-and-effect chain of the degradation mechanism, we can estimate the lifetime of the membrane, until including its total consumption. This approach provides an estimate of membrane lifetime while highlighting the influence of FRR on overall lifetime predictions. The potential reason for the initial shape of the curves was already explained (as shown above), while now we conduct simulations until all reactants are consumed, eventually leading to a complete dissolution of the membrane, in order to be able to estimate the lifetime.

The simulation results are shown in Figure 2.7, which compare the FRR at two constant current densities. Both simulations start with a steep increase in the FRR, followed by a leveling off to form a plateau over several thousand hours to the point where the FRR drops sharply to zero. In the first simulation a current density of $0.3\,\mathrm{A\,cm^{-2}}$ is set, resulting in a maximum FRR of around $0.5\,\mathrm{\mu g\,cm^{-2}\,h^{-1}}$. In the second simulation, the current density is set to a higher value of $1\,\mathrm{A\,cm^{-2}}$, resulting in a lower maximum FRR of around $0.23\,\mathrm{\mu g\,cm^{-2}\,h^{-1}}$. At the simulation with $0.3\,\mathrm{A\,cm^{-2}}$ and a higher FRR maximum, it takes approximately 12,000 hours before all of the starting materials have been decomposed, and there is no more fluoride release, which is equivalent to complete dissolution of the membrane. It takes approximately 25,000 hours to dissolve the membrane at the simulation with $1\,\mathrm{A\,cm^{-2}}$ and the lower maximum FRR. The time until the membrane dissolves is about half as long when the FRR doubles. This result seems explainable because the reactant start concentrations are the same, and the total amount of fluoride dissolved from the membrane is also the same. Moreover, the 12,000–25,000-hour range presented here is tied to our base parameter set, particularly the specific membrane and the constants from

Table 2. Different membranes or contamination levels may exhibit earlier or later failure. However, the lifetime estimates generated here should be interpreted with caution: On the one hand, the model assumes a uniform elevated concentration of H_2O_2 across the membrane. This assumption strongly influences the overall degradation time, since in reality concentrations are higher at the cathode–membrane interface than at the anode interface [31]. On the other hand, we assume complete dissolution of the membrane, which will not occur in practice. Instead, at a certain degree of degradation, pinholes form that already limit the membrane's function [34, 35]. Pinhole formation is a multi-dimensional effect that this lumped model cannot account for.

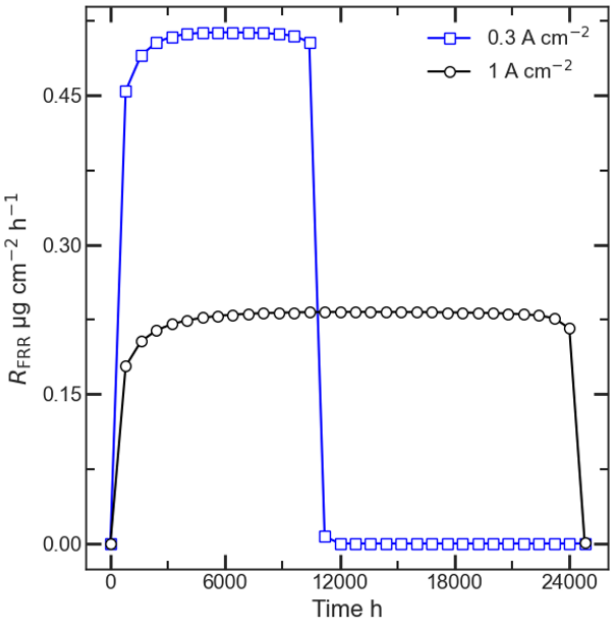

Figure 2.7.: Time-dependent Simulation of FRR at a Current Density of 0.3 and $1\,\mathrm{A\,cm^{-2}}$. Steep increase in the FRR, followed by a leveling off to form a plateau over several thousand hours to the point where the FRR drops sharply to zero.

2.4. Conclusion

We developed a dynamic lumped cell-level model of chemical membrane degradation, by combining state-of-the-art models from the literature for the chemical degradation mechanism [28], hydrogen peroxide formation [11] and oxygen crossover [30]. The model is split into two reaction systems, the cathode catalyst and the membrane, taking into account where the reactions take place. The flux of Fe^{2+} ions into the membrane is a crucial parameter for membrane degradation and was estimated from literature data, resulting in good agreement between observed experimental and simulated values on the FRR. We used the model to examine the effect of performance parameters on the FRR and to study the dynamic degradation behavior during PEM electrolyzer operation.
A maximum degradation is observed at an intermediate level of $0.3\,\mathrm{A\,cm^{-2}}$ for PSSA associated with current density variations. This peak in FRR results from a condition where $^{\bullet}$OH radical generation is maximized. Beyond this point, however, the increased

water flux and $Fe_2{}^+$ ion limitations begin to dominate, resulting in rapid washout of key species and reduced degradation. This highlights the role of the balance between radical production and washout processes in determining membrane degradation.
Simulations at different operating pressure suggest that FRR increases with increasing pressure before leveling off. This effect can be attributed to the increasing H_2O_2 concentration due to elevated O_2 crossover, which increases $^{\bullet}OH$ formation and thus the FRR, which is then eventually limited due to limited availability of Fe^{2+}.
The time-dependent simulation results confirm that the maximum degradation rates are observed at intermediate current density ranges, and the simulations show that the time scale for reaching this maximum degradation extends to thousands of hours. For PEM electrolyzer operators, this suggests that operating their systems close to this intermediate current density range for short-term periods would not significantly accelerate chemical membrane degradation, since these high degradation rates are realized only after a longer period of time. However, prolonged operation at these intermediate current densities will eventually drive the degradation to its maximum plateau level.
Furthermore, dynamic simulations were performed to provide an estimate of membrane lifetime, indicating that the assumed lifetime of the membrane is between 12,000 and 25,000 hours at a constant current density when compared between a maximum and low degradation operating point.
Despite yielding valuable insights, the current model does have several limitations: The lumped nature of the model limits its ability to capture spatial variations or account for differences in cell design. The model simulates complete dissolution of the membrane and does not take into account mechanisms such as pinhole formation that can cause earlier failure of the membrane. Additionally, it requires the prior knowledge or estimation of the Fe^{2+} flux, which may not always be possible.
Future improvements to the model should aim to address these limitations. To provide a more comprehensive representation of the degradation process, the model could be adapted to include additional degradation mechanisms and multi-dimensional effects such as pinhole formation. This would improve the predictability of the model and its ability to more accurately simulate real-world conditions in PEM electrolyzers. Strategies to determine Fe^{2+} concentrations and methods to measure them directly inside the membrane should be explored. The development of multidimensional models will extend the scope of the model considerably. In future extensions, the time-dependent SO_3H concentration predicted by the degradation mechanism could also be coupled to a membrane conductivity model to link chemical aging with electrochemical performance more directly.
While the present chapter focuses on chemical degradation within the membrane, several of its limitations—most notably the lumped model formulation and the simplified treatment of transport phenomena—are directly linked to gas crossover effects. Oxygen crossover enters the degradation model as a boundary condition through H_2O_2 formation, but its magnitude and dependence on operating conditions are not resolved in detail here. For this reason, the following chapter is dedicated to the modeling and experimental analysis of hydrogen and oxygen crossover in PEM electrolyzers.

3. Crossover Phenomena in PEM Electrolyzers

3.1. Introduction

In the preceding chapter, oxygen crossover was identified as a key driver of chemical membrane degradation, since it controls hydrogen peroxide formation and thus radical generation. Because crossover depends strongly on operating conditions and additionally governs gas purity and safety, this chapter examines hydrogen and oxygen crossover in more detail as a central operational process governing species transport across the membrane. Reliable crossover modeling is required to quantify gas mixing effects under relevant operating conditions and to support the subsequent degradation and performance analyses [36, 37].
Early PEM electrolyzer models did not consider gas crossover across the membrane. For example, one of the earliest PEM electrolyzer models was introduced by Choi et al. [16], which focused on fundamental phenomena such as polarization behavior, Butler-Volmer electrode kinetics and electrolyte transport resistance. However, although the model considered the production rates of hydrogen and oxygen, it did not model gas crossover and only included water transport across the membrane.
Later models started including gas crossover, considering molecular diffusion as the primary transport mechanism. For example, Ito et al. [17] developed a more comprehensive cell model that included molecular diffusion of hydrogen and oxygen through the membrane. Crossover was estimated using permeability coefficients derived from a literature-based meta-analysis. However, the model was not experimentally validated, limiting its applicability for realistic conditions. Similarly, Schalenbach et al. [12] also modeled hydrogen and oxygen crossover via diffusion. They experimentally measured anodic hydrogen content to determine the hydrogen permeability coefficient, but used literature values, specifically those from Ito et al., for oxygen permeability, without conducting their own measurements.
For hydrogen crossover, a more advanced model was introduced by Trinke et al. [18], which, like earlier models, still assumes molecular diffusion as the primary transport mechanism. However, it additionally incorporates the effect of hydrogen supersaturation in water, as initially proposed by Bessarabov et al. [38] and supported by experimental studies [39, 40]. Supersaturation here refers to the dissolved gas concentration in the ionomer phase exceeding Henry's law equilibrium values. The model of Trinke et al. [18] accounts for the effect of current density on crossover, includes membrane thickness as a parameter, and shows good agreement with their experimental data under a subset of conditions.
Recent studies have applied the above hydrogen crossover models to analyze PEM electrolyzer behavior under varying conditions. Afshari et al. [19] employed the model of Schalenbach et al. [12] to investigate the influence of temperature, cathode pressure, and membrane thickness on anodic hydrogen content, concluding that thicker membranes substantially reduce crossover. Omrani et al. [20] implemented the Trinke et al. [18] model

within a cell-level simulation to study the role of hydrogen supersaturation. While these works provide valuable insights into crossover trends, they lack experimental validation, limiting their applicability to real-world electrolyzer systems.
For oxygen crossover, Trinke et al. [30] proposed a model based primarily on electro-osmotic drag as main oxygen transport mechanism, rather than molecular diffusion. Supersaturation was included as a constant multiplier of the Henry equilibrium concentration, independent of current density. The model predicted increasing oxygen crossover with current density due to increasing water drag, but assumed a fixed supersaturation level. Although experimental observations qualitatively confirmed a general rise in crossover with increasing current density, the model was not validated against measured oxygen concentrations.
In summary, although numerous studies have proposed gas crossover models for PEM electrolyzers, experimental validation remains limited, especially under realistic, industrially-relevant conditions. Most available data have been obtained at low pressures or from small-scale laboratory setups, which do not adequately represent industrial environments. For example, Schalenbach et al. [12] measured hydrogen crossover at various current densities, but only under low-pressure conditions. Likewise, Trinke et al. [18] investigated both hydrogen and oxygen crossover at laboratory scale and ambient pressure. Industrial PEM electrolyzers typically operate at significantly higher pressures, often tens of bars, to reduce downstream compression requirements, and improve overall system efficiency. Such conditions influence gas crossover behavior, highlighting the need for experimental validation under industrially-relevant, high-pressure operating scenarios. Despite valuable insights from previous studies at low pressures and laboratory scale, a clear gap remains in validating crossover models under elevated pressures and industrial conditions.
We address this gap by presenting new experimental data from a large-scale, high-pressure laboratory PEM electrolyzer operated at constant temperature (60 °C) and then validating existing models and introducing a refined oxygen crossover model. Specifically, we measured hydrogen and oxygen concentrations at the gas outlets of both the anode and cathode compartments. Measurements were conducted under steady-state conditions across a range of current densities (0.2–2 $\mathrm{A\,cm^{-2}}$) and operating pressures (1–8.5 bar) at a constant temperature of 60 °C. These data are used to evaluate the performance of existing hydrogen and oxygen crossover models. We compare model predictions both with the original literature parameters and after fitting selected empirical parameters (e.g., permeability, mass transfer coefficients) to our experimental data. Noting shortcomings in current oxygen crossover models, we introduce a new model that incorporates current density-dependent supersaturation of oxygen, following the approach used in the hydrogen crossover model by Trinke et al. [18].
The remainder of this chapter is structured as follows: Section 3.2 provides an overview of the experimental setup. Section 3.3 presents the crossover models, including both literature-based and newly developed formulations. In Section 3.4, the models are validated against experimental data and applied to simulate crossover behavior under varying pressures and membrane thicknesses. Finally, Section 3.5 summarizes the key findings and discusses implications for electrolyzer design and operation.

3.2. Experimental Setup

The experimental setup is summarized schematically in Figure 3.1.

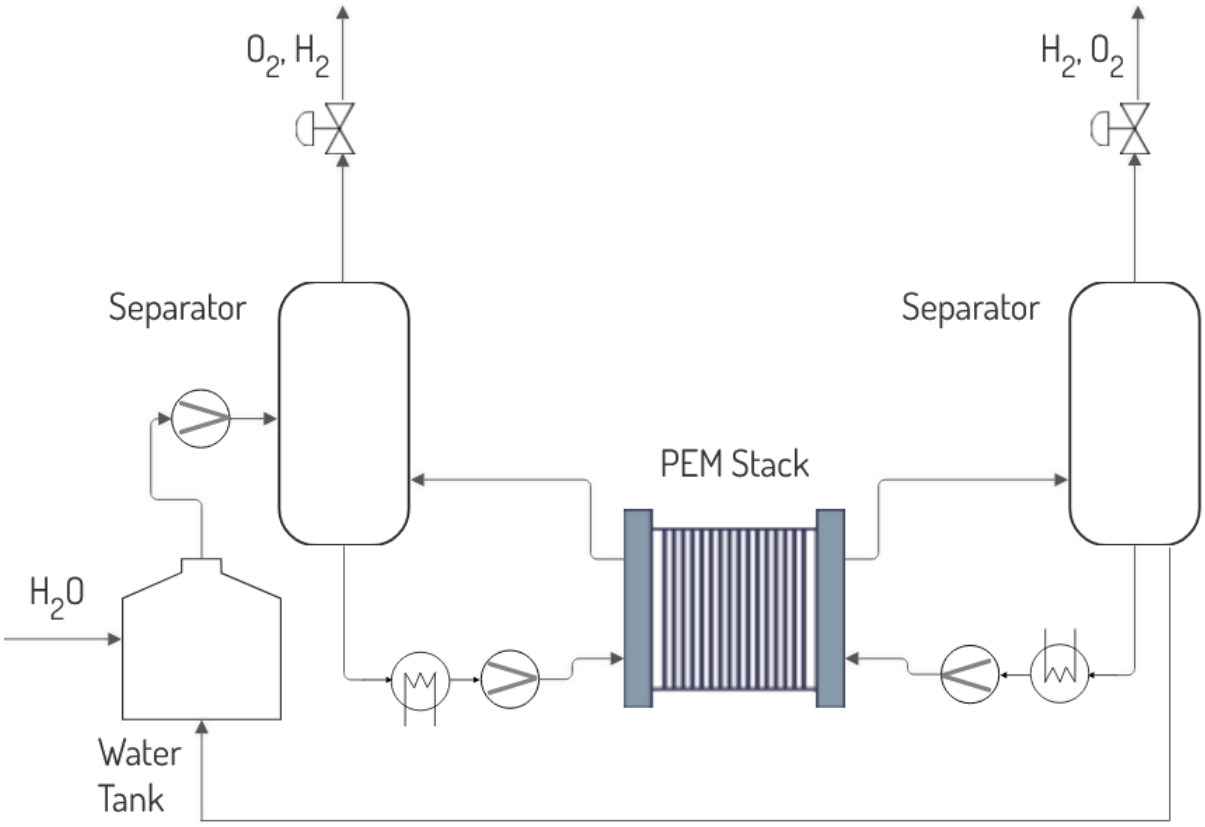

Figure 3.1.: Process-flow diagram of the laboratory PEM electrolyzer test bench used for crossover measurements. The experimental setup is designed according to the Siemens Process Analytics and Instrumentation guidelines for green hydrogen production [41]. Deionized water is recirculated from the tank through the anode (left) and cathode (right) loops. Gas–liquid separators remove entrained water before the dry gas streams are analyzed. Both compartments are operated at equal pressure ($1.15\,\mathrm{bar}$ or $8.5\,\mathrm{bar}$); therefore, no bulk pressure-driven convection across the membrane occurs, and crossover is governed by diffusion and, for O_2, electro-osmotic water drag. Heat exchangers maintain $60\,^{\circ}\mathrm{C}$ and pumps set the loop flow rates. Gas compositions (H_2 in O_2 and O_2 in H_2) are sampled downstream of the separators.

We used a proprietary laboratory-scale PEM electrolyzer stack consisting of six cells with an active area of 300 cm^2 per cell, designed to emulate industrial operation. All cells are equipped with perfluorosulfonic acid (PFSA) membranes, selected for their high proton conductivity and chemical stability. This configuration ensures performance and operational characteristics representative of commercial electrolyzers.
The system includes a complete balance of plant comprising gas-liquid separators, pumps, pressure regulators, and temperature controllers. The gas–liquid separators remove liquid water from the outlet streams, enabling accurate quantification of the dry hydrogen and oxygen concentrations. Gas compositions were determined using gas chromatography, calibrated with certified reference mixtures to ensure accuracy and reproducibility. Pumps control water and gas flow rates, while the pressure and temperature controllers maintain stable operating conditions throughout each experiment.
Experiments were performed at industrially-relevant conditions, particularly under elevated pressures, and with varying current densities and controlled temperatures. Specifically, experiments were performed with both the anode and cathode compartments operated at equal pressure, either both at 1.15 bar or both 8.5 bar. Consequently, no total pressure difference across the membrane was imposed; i.e., no bulk pressure-driven convective permeation could occur in our experiments. The pressures were selected to represent both near-ambient and elevated-pressure operation, allowing systematic analysis of pressure effects on gas crossover. They should be understood as representative conditions, but not as economically optimized set points. All measurements were conducted at a constant temperature of 60 °C, also chosen to reflect industrially-relevant operation. No experiments at variable temperatures were performed. The current density was varied between 0.2 and 2 $A\,cm^{-2}$, with each measurement series lasting several hours. Hydrogen and oxygen concentrations, as well as current, voltage, pressure, temperature, and water flow rates, were continuously recorded. Steady-state conditions were typically reached within a few minutes at all investigated current densities, and no systematic dependence of the equilibration time on current density was observed. Only values obtained during steady-state operation were used for analysis. Concentrations of hydrogen and oxygen were specifically measured at the gas outlets of the corresponding gas-liquid separators. The generated gas crossover measurement data are presented here for the first time as discrete data points in the figures throughout the chapter.

3.3. Gas Crossover Models: Literature and New Approach

Several modeling frameworks have been proposed to describe gas crossover phenomena in PEM electrolyzers, ranging from detailed multi-dimensional simulations to simplified empirical correlations. In this work, we adopt a zero-dimensional, lumped-parameter modeling approach, formulating steady-state mole balances for each compartment without explicitly resolving spatial gradients. Steady-state assumptions are justified as our experimental conditions reach equilibrium rapidly, and transient variations in species concentrations and fluxes become negligible over the measurement periods. Our focus is strictly on calculating gas crossover fluxes across the membrane. In line with the experimental dataset, all models herein are formulated at constant temperature. No explicit temperature is included beyond evaluating literature correlations for diffusion or solubility coefficients at the considered, constant temperature of 60 °C.

The behavior of a PEM electrolysis cell is primarily governed by electrochemical reactions at the electrodes and gas transport across the membrane. A schematic overview of these processes is illustrated in Figure 3.2. The models explicitly incorporate hydrogen and oxygen diffusion, as well as oxygen advective transport via electro-osmotic water drag (commonly termed convection in PEM electrolyzer literature, though distinct from bulk pressure-driven convection). However, transport phenomena such as diffusion and bulk convection within the cathode and anode compartments are implicitly accounted for, based on the assumption of perfect mixing inherent in the lumped-parameter approach.
All crossover models considered in chapter, including the newly proposed oxygen model, assume that gas transport occurs predominantly through the water-swollen hydrophilic domains of the PFSA membrane. This assumption is consistent with the high-hydration operating conditions of PEM electrolyzers, where membranes are continuously water-flooded. While alternative transport pathways through hydrophobic domains have been discussed in the literature [42], these are expected to play only a minor role under the present conditions.
Two-phase phenomena, including bubble nucleation, growth, and coalescence in both compartments, are also implicitly represented in some of the presented models through current density-dependent supersaturation models and empirical mass transfer parameters. Explicit modeling of bubble dynamics or detailed two-phase flow phenomena is beyond the scope of this lumped-parameter approach.
In this section, we first introduce simple models for the cathode and the anode compartment of a PEM electrolyzer, followed by a summary of literature models for hydrogen, oxygen and water crossover in PEM electrolyzers. Subsequently, we introduce an improved oxygen crossover model specifically developed to overcome limitations observed in existing formulations when compared to our new experimental data.

3.3.1. Cathode Compartment

In the cathode compartment, protons are reduced to molecular hydrogen via the half-cell reaction:

$$2\,\mathrm{H^+} + 2\,\mathrm{e^-} \rightarrow \mathrm{H_2}. \tag{3.1}$$

The corresponding hydrogen production rate per unit active area, assuming 100% Faradaic efficiency, is given by [43]:

$$R_{\mathrm{H2}} = \frac{J}{2F}, \tag{3.2}$$

where J is the current density and F is the Faraday constant.
The steady-state mole balance for hydrogen in the cathode compartment is:

$$0 = \dot{n}_{\mathrm{in,\ cat,\ H_2}} + R_{\mathrm{H_2}}\,A - \dot{n}_{\mathrm{out,\ cat,\ H_2}} - \dot{q}_{\mathrm{Crossover,\ H_2}}\,A, \tag{3.3}$$

where $\dot{n}_{\mathrm{in,\ cat,\ H_2}}$ and $\dot{n}_{\mathrm{out,\ cat,\ H_2}}$ represent the molar flow rates of hydrogen entering and leaving the compartment through the inlet and outlet of the half cell, A the cell area, and $\dot{q}_{\mathrm{Crossover,\ H_2}}$ denotes the hydrogen crossover flux from cathode to anode.
The mole balance for oxygen is:

$$0 = \dot{n}_{\mathrm{in,\ cat,\ O_2}} - \dot{n}_{\mathrm{out,\ cat,\ O_2}} + \dot{q}_{\mathrm{Crossover,\ O_2}}\,A, \tag{3.4}$$

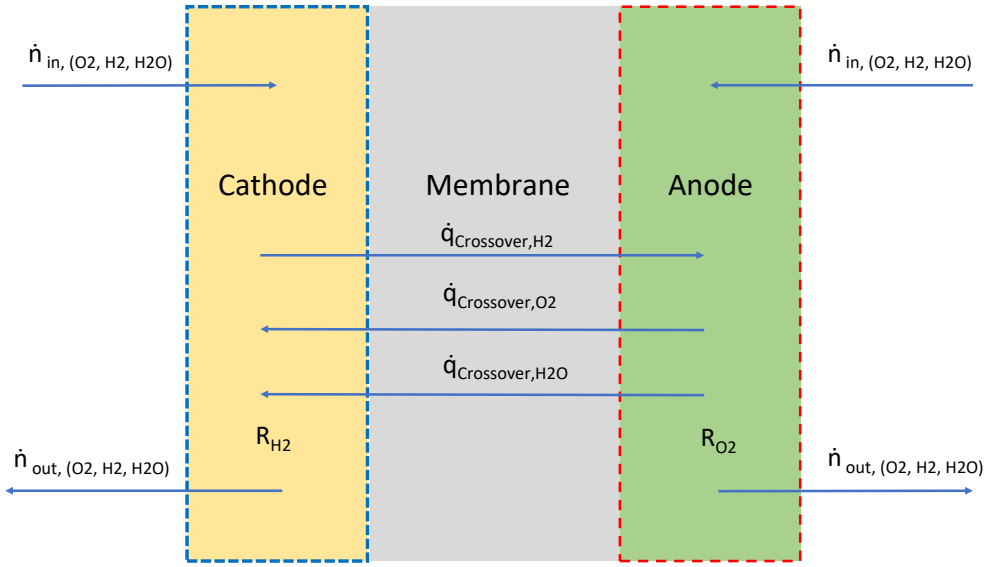

Figure 3.2.: Schematic representation of the anode and cathode control volumes used for mole balance derivation. Species production (R), inlet/outlet flows, and gas crossover fluxes across the membrane are indicated. Flux directions correspond to typical operating conditions; negative fluxes are permitted but not physically expected. All three species (hydrogen (H_2), oxygen (O_2) and water (H_2O)) are shown at both compartment inlets due to impurities and recirculation after gas-liquid separation. Electrochemical reactions (R) are detailed in the respective model section. The embedded schematic illustrates the proposed oxygen crossover model (Section 3.3.3, Eq. (3.24)), which extends the formulation of Trinke et al. [30] by introducing a current-density–dependent supersaturation of oxygen in the anode ionomer film. Oxygen generated by the oxygen evolution reaction can leave the ionomer either by mass transfer to the bulk water phase or through advective transport via electro-osmotic water drag.

where $\dot{n}_{\text{in, cat, O}_2}$ and $\dot{n}_{\text{out, cat, O}_2}$ represent the molar flow rates of oxygen entering and leaving the compartment through the inlet and outlet of the half cell, and $\dot{q}_{\text{Crossover, O}_2}$ represents the oxygen crossover flux from the anode to the cathode compartment. Oxygen recombination is not explicitly included in the mole balance equations but rather lumped in the semi-empirical crossover models presented below, that implicitly account for the effects of oxygen recombination on crossover rates. This is done in analogy with the literature [12, 30], as there is currently no deep understanding of the recombination mechanism.

Lastly, the water balance is given by:

$$0 = \dot{n}_{\text{in, cat, H}_2\text{O}} - \dot{n}_{\text{out, cat, H}_2\text{O}} + \dot{q}_{\text{Crossover, H}_2\text{O}}\, A, \tag{3.5}$$

where $\dot{n}_{\text{in, cat, H}_2\text{O}}$ and $\dot{n}_{\text{out, cat, H}_2\text{O}}$ represent the molar flows of water entering and leaving the compartment through the inlet and outlet of the half cell and $\dot{q}_{\text{Crossover, H}_2\text{O}}$ represents the water crossover flux from the anode to the cathode compartment.

3.3.2. Anode Compartment

In the anode compartment, water is oxidized to produce oxygen, protons, and electrons according to:

$$2\,H_2O \rightarrow O_2 + 4\,H^+ + 4\,e^-. \tag{3.6}$$

The corresponding oxygen production rate per unit active area, assuming 100% Faradaic efficiency, is given by [43]:

$$R_{O_2} = \frac{J}{4F}, \tag{3.7}$$

where J is the current density and F is the Faraday constant.
The steady-state mole balance for hydrogen in the anode compartment accounts for crossover from the cathode:

$$0 = \dot{n}_{\text{in, an, } H_2} - \dot{n}_{\text{out, an, } H_2} + \dot{q}_{\text{Crossover, } H_2}\, A, \tag{3.8}$$

where $\dot{n}_{\text{in, an, } H_2}$ and $\dot{n}_{\text{out, an, } H_2}$ represent the molar flow rates of hydrogen entering and leaving the compartment through the inlet and outlet of the half cell.
Similar to the cathode mole balance, hydrogen recombination is not explicitly included in the mole balance equations. Instead, it is assumed that the effects of hydrogen recombination on the crossover rates are implicitly accounted for during the empirical fitting process for the crossover models with the measured data.
The mole balance for oxygen is given by:

$$0 = \dot{n}_{\text{in, an, } O_2} - \dot{n}_{\text{out, an, } O_2} + R_{O_2}\, A - \dot{q}_{\text{Crossover, } O_2}\, A, \tag{3.9}$$

where $\dot{n}_{\text{in, an, } O_2}$ and $\dot{n}_{\text{out, an, } O_2}$ represent the molar flow rates of oxygen entering and leaving the compartment through the inlet and outlet of the half cell. The water balance in the anode includes consumption via the oxygen evolution reaction and transport across the membrane:

$$0 = \dot{n}_{\text{in, an, } H_2O} - \dot{n}_{\text{out, an, } H_2O} - \dot{q}_{\text{Crossover, } H_2O}\, A - R_{H_2O}\, A, \tag{3.10}$$

where $\dot{n}_{\text{in, an, } H_2O}$ and $\dot{n}_{\text{out, an, } H_2O}$ represent the molar flow rates of water entering and leaving the compartment through the inlet and outlet of the half cell, $R_{H_2O} = 2\,R_{O_2}$ represents the consumption rate of water per unit area inside the compartment and $\dot{q}_{\text{Crossover, } H_2O}$ represents the water crossover flux from the anode to the cathode compartment.

3.3.3. Crossover Models

In this section, we present hydrogen and oxygen crossover models for PEM electrolyzers. Hydrogen and oxygen are treated separately because the dominant transport mechanisms and thus the modeling approaches may differ for each gas. Hydrogen crossover is primarily diffusion-driven, while oxygen crossover according to some models is influenced more strongly by electro-osmotic drag. Besides established crossover models, we introduce a newly developed oxygen crossover model. All presented models are later evaluated against experimental data in Section 3.4 to assess their predictive accuracy under industrially-relevant conditions.

Hydrogen Crossover Models Several hydrogen crossover models have been proposed in the literature, primarily based on diffusion through the membrane. The two most widely referenced models are those of Schalenbach et al. and Trinke et al., which differ in their treatment of supersaturation effects.

1. **Schalenbach et al. Model [44]**: This model assumes that hydrogen crossover occurs solely by molecular diffusion, without supersaturation effects, and neglects hydrogen partial pressure in the anode. The flux is given by:

$$\dot{q}_{\text{Crossover, H}_2} = \frac{\epsilon_{\text{H}_2}\, p_{\text{cathode,H}_2}}{d_{\text{membrane}}}, \tag{3.11}$$

with ϵ_{H_2} as the permeability coefficient of hydrogen in PFSA membranes, $p_{\text{cathode,H}_2}$ as the partial pressure of hydrogen in the cathode and d_{membrane} as thickness of the membrane.

In this and following models, the permeability coefficients for hydrogen and oxygen are treated as independent empirical parameters, consistent with prior literature and reflective of their distinct transport behaviors in PFSA membranes.

2. **Trinke et al. Model [18]:** This model also considers diffusion but in contrast to the model by Schalenbach et al. [44], Trinke et al. [18] introduces the effect of hydrogen supersaturation in the ionomer film of the cathode catalyst layer. Their model assumes that the generated molecular hydrogen initially dissolves in the water phase within the ionomer film. Once solubility is exceeded, hydrogen is thermodynamically expected to transition into the gas phase; however, this process is limited by mass transport from the ionomer to the bulk water. As a result, supersaturation increases with current density. Based on these assumptions, Trinke et al. [18] formulated a mass balance to compute the supersaturated hydrogen concentration in the ionomer film:

$$c_{\text{H}_2}^{\text{super}} = \frac{\left(\frac{J}{2F} + k_{\text{MT,H}_2}\, c_{\text{H}_2}^{\text{Henry}}\right)}{k_{\text{MT,H}_2} + \frac{D_{\text{H}_2}^{\text{eff}}}{d_{\text{membrane}}}}, \tag{3.12}$$

with J as the current density, $c_{\text{H}_2}^{\text{Henry}}$ as the equilibrium concentration of hydrogen in water according to Henry's Law, $D_{\text{H2}}^{\text{eff}}$ as the effective diffusion coefficient of hydrogen in PFSA membranes, F as the Faraday constant, $k_{\text{MT,H}_2}$ as the mass transfer coefficient for transport of hydrogen from the ionomer film to the bulk water in the cathode, and d_{membrane} as the thickness of the membrane.

The effective diffusion coefficient is defined as:

$$D_{\text{H}_2}^{\text{eff}} = \frac{\phi}{\tau} D_{\text{H}_2}, \tag{3.13}$$

with D_{H_2} denotes the diffusion coefficient of hydrogen in PFSA membranes, ϕ is the volume fraction of water in the membrane, and τ represents the tortuosity of the water channels within the membrane. The effective permeability is proportional to ϕ/τ, indicating that it increases with porosity and decreases with tortuosity. Following Trinke et al. [30], the effective diffusion coefficient of oxygen in the membrane is corrected by the water volume fraction ϕ. While ϕ is not a literal porosity, it serves

as an approximate measure of the water-filled free volume within the polymeric membrane. In this way, ϕ provides a physically motivated correction factor for molecular diffusion in hydrated membranes. This simplified approach captures the dominant effect of water uptake on gas transport without requiring a detailed microstructural model.

The equilibrium concentration of dissolved hydrogen at the gas–ionomer interface is given by Henry's law:

$$c_{\mathrm{H_2}}^{\mathrm{Henry}} = S_{\mathrm{H_2}}\, p_{\mathrm{cathode,H_2}}, \tag{3.14}$$

with $S_{\mathrm{H_2}}$ as the solubility of hydrogen in water.

Trinke et al. [18] consider different approaches to model the mass transfer coefficient $k_{\mathrm{MT,H_2}}$, which they interpret as describing the diffusive transport of dissolved hydrogen from the ionomer film to the surrounding liquid phase. This coefficient does not represent phase change (e.g., degassing into gas bubbles), but rather the limited mass transfer that gives rise to local supersaturation within the ionomer. In particular, they consider $k_{\mathrm{MT,H_2}}$ to either be constant,

$$k_{\mathrm{MT,H_2}} = \text{constant} \tag{3.15}$$

or a linear function of current density,

$$k_{\mathrm{MT,H_2}} = a_{\text{fitting}}\, J + b_{\text{fitting}} \tag{3.16}$$

or proportional to the square root of current density,

$$k_{\mathrm{MT,H_2}} = c_{\text{fitting}}\, \sqrt{J} \tag{3.17}$$

with a_{fitting}, b_{fitting}, and c_{fitting} as fitting parameters.

Inserting the supersaturated concentration $c_{\mathrm{H_2}}^{\mathrm{super}}$ into Fick's law, and assuming negligible hydrogen concentration on the anode side, yields the final crossover flux expression:

$$\dot{q}_{\mathrm{Crossover,\ H_2}} = \frac{D_{\mathrm{H2}}^{\mathrm{eff}} \left(\frac{J}{2F} + k_{\mathrm{MT,H_2}}\, S_{\mathrm{H_2}}\, p_{\mathrm{cathode,H_2}}\right)}{k_{\mathrm{MT,H_2}}\, d_{\mathrm{membrane}} + D_{\mathrm{H2}}^{\mathrm{eff}}}. \tag{3.18}$$

When comparing the two models in Equations (3.11) and (3.18), they both predict that crossover increases with increasing hydrogen partial pressure in the cathode and with decreasing membrane thickness. However, the second model also predicts that hydrogen crossover increases with current density.

Oxygen Crossover Models Three oxygen crossover models are considered in this study: two from the literature and one newly proposed. The first, by Schalenbach et al. [44], is based solely on diffusion through the membrane. It assumes that advective transport via water drag and supersaturation effects are negligible. This simplification is justified by the authors with the statement that supersaturation is difficult to quantify and has a minor impact under typical operating conditions. However, previous studies in electrochemical systems have shown that gas concentrations can exceed solubility limits, particularly at elevated current densities [40, 45, 46]. As a result, neglecting supersaturation may lead to underestimation of crossover, especially in industrially-relevant regimes.

1. **Schalenbach et al. Model [44]** Despite this limitation, the Schalenbach model remains widely used and computes the oxygen crossover flux as:

$$\dot{n}_{\text{Crossover, O}_2} = \frac{\epsilon_{\text{O}_2}\, p_{\text{anode,O}_2}}{d_{\text{membrane}}}, \tag{3.19}$$

where ϵ_{O_2} is the permeability coefficient of oxygen in PFSA membranes, $p_{\text{anode,O}_2}$ is the partial pressure of oxygen in the anode and d_{membrane} is the thickness of the membrane.

2. **Trinke et al. Model [30]:** This model adopts a fundamentally different approach from Schalenbach et al., assuming advective oxygen transport via electro-osmotic drag as the dominant transport mechanism for oxygen, while neglecting diffusion. Unlike the corresponding hydrogen model discussed in Section 3.3.3, this model only includes the effect of oxygen supersaturation as a constant factor, independent of current density.

   The crossover flux is given by:

$$\dot{q}_{\text{Crossover,O}_2} = \frac{\text{TWK}\, J\, p_{\text{anode,O}_2}\, S_{O_2}\, s_{\text{sat}}}{F\, \frac{\rho_{\text{H2O}}}{M_{\text{H2O}}}}, \tag{3.20}$$

   where TWK is the number of water molecules per H^+ ions transported across the membrane, ρ_{H2O} is the density of water and $M_{\text{H}_2\text{O}}$ is the molar mass of water, S_{O_2} is the solubility of oxygen in water and s_{sat} the supersaturation factor. While this model introduces supersaturation, its fixed value may not capture the observed nonlinear dependence of oxygen crossover on current density in large-scale systems, as will be shown in Section 3.4.1. We note that, unlike diffusion-driven models, the oxygen crossover model of Trinke et al.[30] as well as our extension do not contain an explicit membrane thickness term. In diffusion-based formulations, thickness enters as the transport length L in Fick's law (D/L). By contrast, in the framework of Trinke et al., oxygen transport is modeled via electro-osmotic drag, and the empirical parameter $k_{\text{MT,O}_2}$ describes transfer between the ionomer film and the bulk water phase, independent of membrane thickness. As a result, the three empirical expressions evaluated for $k_{\text{MT,O}_2}$ are formally thickness-independent. Dedicated experiments varying membrane thickness would be required to investigate thickness effects on oxygen crossover within this modeling framework.

3. **Proposed model incorporating effect of current density on supersaturation:**

   Our experimental results with the setup described in Section 3.2 revealed a nonlinear increase in oxygen crossover with current density (see Section 3.4.1), which is not captured by existing models. Thus we additionally propose the following modification of the model of Trinke et al. [30]: Instead of considering a constant supersaturation factor, we assume that the supersaturation increases with current density, as was done in the hydrogen crossover model of Trinke et al. [18] discussed in Section 3.3.3 (but not in their oxygen crossover model [30]).

   To derive the equations of this oxygen crossover model, we adapt the approach Trinke et al. [18] used to derive the supersaturation in their hydrogen model. Specifically,

we consider a mole balance around the ionomer film in the anode catalyst layer, in which oxygen is formed via Reaction (3.6), and which the oxygen can leave either via transfer to the bulk phase of water in the anode compartment, or through advective transport with water carried by electro-osmotic drag:

$$0 = \underbrace{\frac{J}{4F}}_{\mathrm{O_2\text{-}Evolution}} \underbrace{- k_{\mathrm{MT,O_2}}(c_{\mathrm{O_2}}^{\mathrm{super}} - c_{\mathrm{O_2}}^{\mathrm{Henry}})}_{\text{Mass transfer}} \underbrace{- \frac{\mathrm{TWK}\, J\, c_{\mathrm{O_2}}^{\mathrm{super}}}{F\, \frac{\rho_{\mathrm{H_2O}}}{M_{\mathrm{H2O}}}}}_{\text{Advection}}, \tag{3.21}$$

where $k_{\mathrm{MT,O_2}}$ is the mass transfer coefficient, and $c_{\mathrm{O_2}}^{\mathrm{super}}$ is the supersaturated molar concentration of oxygen in the ionomer film in the anode catalyst layer, which is unknown. The mass transfer coefficient $k_{\mathrm{MT,O_2}}$ is also not known a priori and may vary with operating conditions. To account for this, we evaluate different functional dependencies of $k_{\mathrm{MT,O_2}}$ on current density J, including constant, linear, and square-root forms, as part of the model validation (see Section 3.4.1).

Solving (3.21) for the supersaturated concentration yields:

$$c_{\mathrm{O_2}}^{\mathrm{super}} = \frac{\frac{J}{4F} + k_{\mathrm{MT,O_2}}\ c_{\mathrm{O_2}}^{\mathrm{Henry}}}{\frac{\mathrm{TWK}\, J}{F\, \frac{\rho_{\mathrm{H_2O}}}{M_{\mathrm{H_2O}}}} + k_{\mathrm{MT,\ O_2}}}, \tag{3.22}$$

with the Henry concentration defined as:

$$c_{\mathrm{O_2}}^{\mathrm{Henry}} = S_{\mathrm{O_2}}\, p_{\mathrm{anode,O_2}}. \tag{3.23}$$

Now the supersaturated molar concentration can be inserted into the advective transport term of Equation (3.21) to compute the crossover flux:

$$\dot{q}_{\mathrm{Crossover,O_2}} = \frac{\frac{J}{4F} + k_{\mathrm{MT,O_2}}\ S_{\mathrm{O_2}}\, p_{\mathrm{anode,\ O_2}}}{1 + \frac{F\, \rho_{\mathrm{H2O}}\, k_{\mathrm{MT,\ O_2}}}{M_{\mathrm{H2O}}\, \mathrm{TWK}\, J}}. \tag{3.24}$$

The three models differ fundamentally in how they capture the dependence of oxygen crossover on operating parameters:
The Schalenbach et al. model (Eq. (3.19)) is purely diffusive and predicts that crossover increases with oxygen partial pressure and decreases with membrane thickness. However, it is independent of current density and does not account for supersaturation effects, making it best suited for systems operating at low current densities.
The Trinke et al. model (Eq. (3.20)) incorporates a constant supersaturation factor and models crossover as an advective process driven by electro-osmotic drag. It predicts a linear increase in oxygen crossover with current density, but may underpredict crossover at high currents where supersaturation is more pronounced.
The proposed model (Eq. (3.24)) combines two mechanisms: electro-osmotic drag and current-dependent supersaturation. As current density increases, it captures the dual effect of increased water transport and increased oxygen solubility in the ionomer phase. This leads to a nonlinear rise in oxygen crossover, consistent with our experimental observations (see Section 3.4.1). Moreover, the mass transfer coefficient $k_{\mathrm{MT,O_2}}$ in this model can be treated as a function of current density, following the approach used for hydrogen

crossover in Trinke's earlier work [18], offering additional flexibility for parameter fitting and refinement.

Water Crossover Model In PEM electrolyzers with equal anode and cathode pressure, water is primarily transported across the membrane via electro-osmotic drag. This mechanism arises from the movement of H^+ ions through the membrane, which simultaneously carry water molecules from the anode to the cathode.

The resulting water crossover flux can be described by [47]:

$$\dot{q}_{\text{Crossover, } H_2O} = \frac{\text{TWK}\, J}{F}, \tag{3.25}$$

with TWK as the number of water molecules per H^+ ions transported across the membrane, J as the current density and F as the Faraday constant.

This water transport plays a central role in advective gas crossover, particularly for oxygen, as discussed in the preceding section. In this study, water crossover was included in the modeling framework via the electro-osmotic drag relation, but no experimental measurements of water crossover were performed with the available setup. As a result, the water crossover description was not validated against data and is treated as a modeled effect only.

3.3.4. Implementation

The crossover models were implemented in Aspen Custom Modeler (ACM), a platform well-suited for steady-state, equation-oriented modeling. ACM enables efficient handling of algebraic systems, parameter estimation, and numerical optimization, which aligns with the lumped-parameter approach and steady-state mole balances employed in this study.

Parameter estimation was carried out using ACM's built-in Newton-based solver combined with a least-squares fitting algorithm. This enabled the adjustment of key model parameters, such as permeability and mass transfer coefficients, to match experimental data across a range of operating pressures and current densities.

The implemented models are not publicly available due to intellectual property considerations.

3.4. Results & Discussion

The following section is divided into two main parts: The first part (Section 3.4.1) presents the validation and parameter estimation of the models, while the second part (Section 3.4.2) presents predictions made with the best-performing models regarding the effects of pressure and membrane thickness.

3.4.1. Validation and Parameter Estimation

To assess the predictive accuracy of the literature models, we compare them to experimental data obtained from the setup described in Section 3.2.

Empirical model parameters, primarily permeability coefficients, diffusion coefficients, and mass transfer coefficients related to gas transport from the ionomer phase, were considered. In our analysis, solubility and diffusivity coefficients were fixed to literature values, as they

are well established and less uncertain under the studied conditions. By contrast, the mass transfer coefficient $k_{\mathrm{MT,O_2}}$ from the anode ionomer film to the anode bulk liquid water was selected as the adjustable parameter because it directly controls the supersaturation level in our proposed oxygen model, and thereby determines the slope of the crossover–current density relationship. The main discrepancies between literature predictions and our measurements were observed in this slope, making $k_{\mathrm{MT,O_2}}$ the most effective parameter for calibration. This choice is consistent with the methodology of Trinke et al. [18].
Table 3.1 summarizes the model parameters used in this study, while Table 3.2 lists those subject to data fitting.

Table 3.1.: Model parameters and their values

Parameter	**Symbol**	**Value**
Faraday constant	F	$96\,485\,\mathrm{C\,mol^{-1}}$
Water density	$\rho_{\mathrm{H_2O}}$	$997\,\mathrm{kg\,m^{-3}}$
Water molar mass	$M_{\mathrm{H_2O}}$	$18\,\mathrm{g\,mol^{-1}}$
Volume fraction of water in the membrane	ϕ	0.37 [48]
Tortuosity	τ	1.5 [48]
Membrane thickness	d_{membrane}	9×10^{-5} m
Active area (per cell)	A	$300\,\mathrm{cm^2}$
Solubility of hydrogen in water	S_{H_2}	$7 \times 10^{-6}\,\mathrm{mol\,Pa^{-1}\,m^{-3}}$ [49]
Solubility of oxygen in water	S_{O_2}	$9.8 \times 10^{-6}\,\mathrm{mol\,Pa^{-1}\,m^{-3}}$ [17]
Diffusion coefficient of H_2 in PFSA	$D_{\mathrm{H_2}}$	$1.26 \times 10^{-8}\,\mathrm{m^2\,s^{-1}}$ [50]
Operating temperature	T	60 °C
Number of water molecules per H^+	TWK	2 [51]

While formal identifiability analysis was not performed, we limited the number of fitted parameters to avoid overparameterization and focused only on those directly influencing gas crossover. The fitted models reproduced the experimental trends well across all tested conditions, supporting both the practical identifiability and relevance of the selected parameters.

Hydrogen Crossover Models In this subsection, we evaluate the performance of the hydrogen crossover models described in Section 3.3.3 using experimental data at 1.15 and 8.5 bar. Figure 3.3 compares the measured and modeled hydrogen crossover flux under both conditions.
The Schalenbach et al. [44] model, which assumes purely diffusive transport and does not account for current density effects or pressure-induced supersaturation, predicts a constant crossover flux. As a result, it fails to capture the experimentally observed increase in hydrogen crossover with current density.

In contrast, the Trinke et al. [18] model, which accounts for the effects of current density, performs better overall in predicting hydrogen crossover. In particular, the model captures the increasing trend of hydrogen crossover flux with increasing current density. Qualitatively, the linear relationship assumed by the model aligns well with the shape of our experimental data, reinforcing its utility as a first-order approximation under varying operational regimes. However, slight deviations from linearity are observed at higher current densities, which may arise from pressure effects, local mass transport limitations, or recombination phenomena not explicitly captured by the original formulation.
Quantitatively, there is a noticeable difference in slope between the experimental data and predictions using the original parameter values from Trinke et al. [18]. This discrepancy may also reflect differences in mass transfer conditions, such as the interaction between the ionomer and bulk water in our setup compared to assumptions in the literature or more fundamentally, differences in the membrane material itself, including manufacturer, fabrication process, or membrane history. Notably, our setup uses a significantly thinner membrane (90 µm) than the 200 µm membranes employed by Trinke et al. [18], which affects diffusion resistance and overall gas transport. While such effects do not directly influence the intrinsic membrane permeability, we treat permeability as an effective fitting parameter that captures these system-level influences during model calibration.
To address this, we fitted both the permeability coefficient (ϵ_{H2}) and the mass transfer coefficient ($k_{\mathrm{MT,H_2}}$) to our experimental data, achieving a more accurate representation of gas crossover under our specific operating conditions. A comparison between the original and fitted parameter values highlights the importance of system-specific calibration (see Figure 3.3).
While the qualitative performance of the models is similar at both 1.15 and 8.5 bar, we further examined the model's ability to match elevated-pressure data. Figure 3.3b presents the simulation results at 8.5 bar, comparing predictions using the original literature parameters from Trinke et al. [18] with predictions using parameters refitted to our high-pressure measurements. The Trinke et al. [18] model, which incorporates the effect of current density on hydrogen crossover via supersaturation, shows a noticeable discrepancy when applied with the original mass transfer coefficient ($k_{\mathrm{MT,H_2}}$) from the literature, particularly in the slope of the crossover–current density relationship. By refitting this parameter to our experimental data, the model's agreement with the measurements improves significantly.
In both cases, the fitted values for $k_{\mathrm{MT,H_2}}$ differ from those reported in the literature (see Table 3.2), underscoring the sensitivity of empirical model parameters to operating conditions and system-specific factors. These deviations reinforce the need for pressure-specific calibration and, ideally, the development of more mechanistic models that can capture such dependencies without repeated empirical refitting. Notably, the membranes used in their experiments were more than twice as thick as the ones we employed, and such differences in membrane thickness increase the diffusion path length and thus the diffusion resistance, whereas membrane microstructure and fabrication can influence the intrinsic diffusion coefficient (D_{H2}). Additionally, variations in mass transfer conditions from the ionomer to bulk water may contribute to the discrepancies between their model predictions and our experimental results.

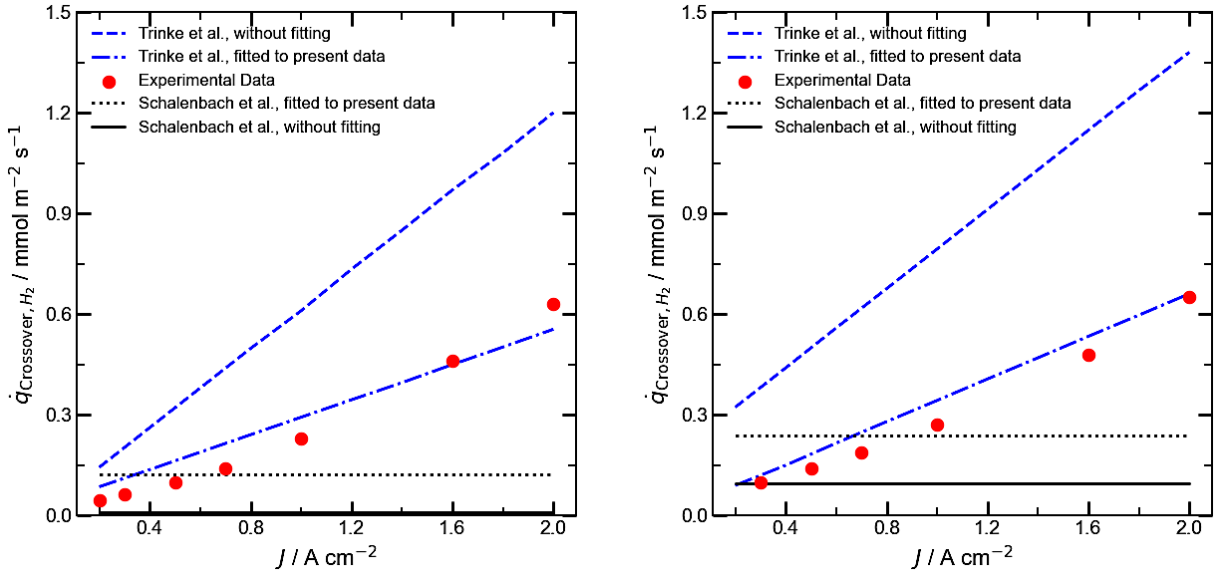

(a) Hydrogen crossover at 1.15 bar

(b) Hydrogen crossover at 8.5 bar

Figure 3.3.: Comparison of hydrogen crossover flux from Schalenbach et al. [44] and Trinke et al. [18] models with experimental data from the setup described in Section 3.2. The permeability coefficient in Schalenbach's model and the mass transfer coefficient in Trinke's model were also re-fitted to this experimental data.

Oxygen Crossover Models Following the hydrogen crossover validation, we now assess the predictive accuracy of the oxygen crossover models described in Section 3.3. As with hydrogen, we aim to evaluate whether these models capture the experimentally observed trends across varying current densities and pressures. To this end, we compare both the original formulations, with parameter values taken from literature, and versions calibrated to our own data through parameter fitting.

Before turning to the comparison between literature models and our proposed formulation, we first evaluated whether the mass transfer coefficient $k_{\mathrm{MT,O_2}}$ in our model should be treated as constant or current-dependent. Specifically, we tested constant, linear, and square-root dependencies, following the approach by Trinke et al. [18]. Among these, the linear form provided the best fit across both 1.15 and 8.5 bar. Details and a comparative visualization of the different fits are provided in Appendix B.

Figure 3.4a compares the oxygen crossover predictions at 1.15 bar using literature models and the proposed model with a linearly fitted mass transfer coefficient. The Schalenbach et al. model [44], which assumes purely diffusive transport and excludes any current dependence, significantly underpredicts crossover and fails to reflect the experimental trend. The Trinke et al. model [30], which includes a constant supersaturation factor and models crossover via electro-osmotic drag, captures the increase with current density, but fails to capture the nonlinear shape of the relationship.

In contrast, the proposed model aligns better with the data across all current densities and shows a nonlinear behavior more closely resembling the experimental observation. This is because of the dual effect of current density on crossover as discussed in Section 3.3.3: increasing current density increases both the supersaturation in the ionomer due to oxygen increased production, as well as the water drag through the membrane.

To evaluate the performance of the oxygen crossover models at elevated pressure, Figure 3.4b presents a comparison of predictions and measurements at 8.5 bar. The results are qualitatively consistent with the 1.15 bar case: the Schalenbach et al. model [44] again underestimates crossover due to its lack of current dependence and omission of advective transport. The Trinke et al. model [30], while more accurate than the Schalenbach model, does not fully capture the nonlinear shape of the experimental data.
In contrast, the proposed model shows improved agreement with the experimental data across the full current range, also at 8.5 bar, although some deviations remain. Table 3.2 summarizes the fitting parameters and root mean square (RMS) errors for all oxygen crossover models, evaluated at 1.15 bar and 8.5 bar.
To assess how well the models capture the pressure dependence of gas crossover, we performed separate parameter fits at 1.15 bar and 8.5 bar using the respective experimental datasets. In both cases, the resulting root mean square (RMS) errors were low (see Table 3.2), indicating that the model structures are robust across different pressures. For instance, the Trinke model for oxygen yielded RMS errors of 1.4×10^{-2} at 1.15 bar and 1.8×10^{-2} at 8.5 bar; for hydrogen, the errors were 5.1×10^{-2} and 5.9×10^{-2}, respectively. This close agreement suggests that the models successfully represent the dominant pressure-dependent transport mechanisms, such as changes in gas solubility, convective driving forces, and electro-osmotic drag, without requiring structural modification. While experimental data are only available at two discrete pressures, the consistently low errors support the conclusion that the models reliably capture crossover behavior across the tested pressure range.

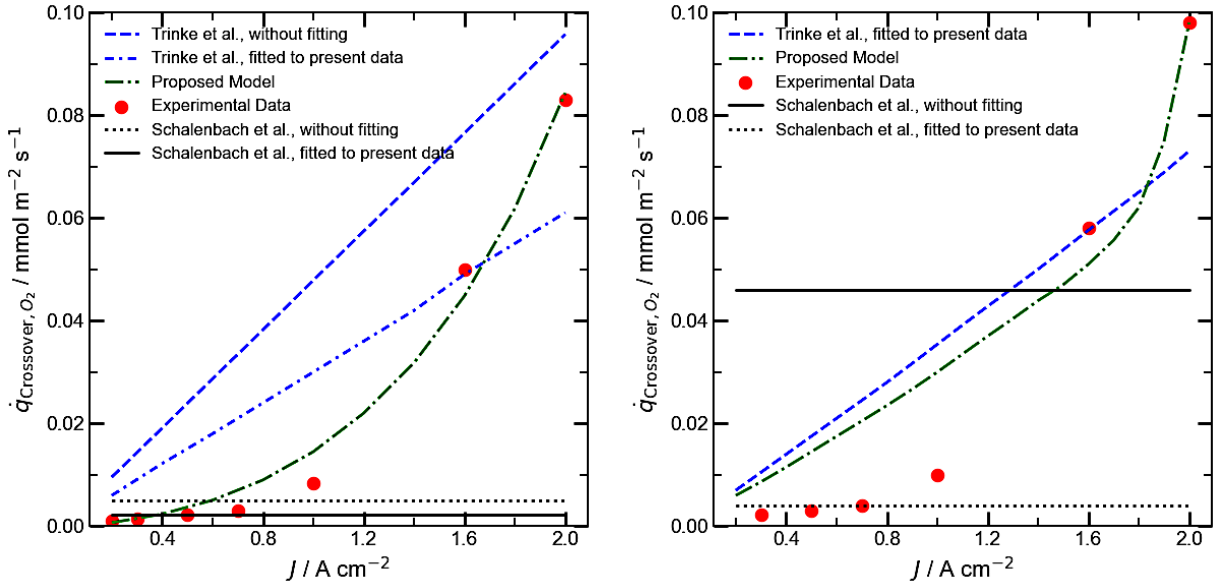

(a) Oxygen crossover at 1.15 bar.

(b) Oxygen crossover at 8.5 bar.

Figure 3.4.: Validation of the proposed oxygen crossover model (Eq.3.24) through comparison with the literature models of Schalenbach et al. [44] and Trinke et al. [30], fitted to experimental data at (a) 1.15 bar and (b) 8.5 bar. The Schalenbach model assumes purely diffusive transport and is independent of current density, while the Trinke model includes constant supersaturation. For clarity, the original (unfitted) Trinke model is excluded from panel (b) due to being significantly off-scale. Mass transfer coefficients in the fitted models are optimized to reflect system-specific conditions. Among the tested approaches, the proposed model provides the best agreement across both pressures. All simulation curves are interpolated between computed data points.

3.4.2. Parameter Study

In the following, we use the best-performing crossover models identified above to analyze the influence of key operating parameters on gas crossover behavior at varying current densities. Specifically, we investigate the effects of pressure, membrane thickness, and current density, which play dominant roles in determining gas crossover behavior. Pressure directly influences gas solubility (via Henry's law) and thereby the driving force for diffusive transport. While electro-osmotic drag is governed by current density (i.e., the water flux is pressure-independent under constant hydration), the advected O_2 still increases with pressure because the dissolved concentration in the liquid phase rises with p_{O_2} via Henry's law. Membrane thickness controls the effective transport resistance for both diffusion and electro-osmotic drag, and current density determines the rate of gas evolution and affects local saturation conditions. Together, these parameters are central to balancing performance, gas purity, and safety in PEM electrolyzers.

The investigated parameter ranges reflect values commonly encountered in industrial systems. Pressure was varied between 1.15 and 31 bar, covering typical operating conditions from ambient to elevated pressures used for high-density hydrogen storage and system integration. Membrane thickness was varied between 50 µm and 200 µm, encompassing commercially available PFSA membranes used in practice. Current density was varied

Table 3.2.: Fitting parameters and root mean square (RMS) errors for oxygen and hydrogen crossover models at 1.15 bar and 8.5 bar. The table includes parameter values from the original literature (*Literature Values*) and parameters obtained by fitting to our experimental data (*Fitted Values*). For the proposed model, the table reports the results of fitting using different approaches, assuming constant (no dependence), linear (proportional to current density), and square-root (proportional to the square root of current density) dependencies.

Model	Parameter(s)	Literature Value(s)	Fitted Value(s)		RMS Error	
			1.15 bar	8.5 bar	1.15 bar	8.5 bar
Schalenbach et al. (Hydrogen)	ϵ_{H_2} / $\mathrm{mol\,Pa^{-1}\,m^{-1}}$	$5.32 \cdot 10^{-11}$ [44]	-	-	$2.9 \cdot 10^{-1}$	$2.8 \cdot 10^{-1}$
Schalenbach et al. (Hydrogen, Fitted)	ϵ_{H_2} / $\mathrm{mol\,Pa^{-1}\,m^{-1}}$	-	$6.18 \cdot 10^{-10}$	$1.31 \cdot 10^{-10}$	$2.1 \cdot 10^{-1}$	$2.4 \cdot 10^{-1}$
Trinke et al. (Hydrogen)	k_{MT} / $\mathrm{m\,s^{-1}}$	$1 \cdot 10^{-3}$ [18]	-	-	$5.3 \cdot 10^{-1}$	$3.6 \cdot 10^{-1}$
Trinke et al. (Hydrogen, Fitted)	k_{MT} / $\mathrm{m\,s^{-1}}$	-	$6.72 \cdot 10^{-3}$	$9.87 \cdot 10^{-3}$	$5.1 \cdot 10^{-2}$	$5.9 \cdot 10^{-2}$
Schalenbach et al. (Oxygen)	ϵ_{O_2} / $\mathrm{mol\,Pa^{-1}\,m^{-1}}$	$2.52 \cdot 10^{-11}$ [44]	-	-	$3.56 \cdot 10^{-2}$	$4.54 \cdot 10^{-2}$
Schalenbach et al. (Oxygen, Fitted)	ϵ_{O_2} / $\mathrm{mol\,Pa^{-1}\,m^{-1}}$	-	$1.11 \cdot 10^{-11}$	$2.19 \cdot 10^{-12}$	$3.5 \cdot 10^{-2}$	$4.4 \cdot 10^{-2}$
Trinke et al. (Oxygen)	s_{sat} / -	15 [30]	-	-	$2.40 \cdot 10^{-2}$	$2.40 \cdot 10^{-2}$
Trinke et al. (Oxygen, Fitted)	s_{sat} / -	-	9.25	11.8	$1.4 \cdot 10^{-2}$	$1.8 \cdot 10^{-2}$
Proposed Model (Oxygen, Constant)	k_{MT} / $\mathrm{m\,s^{-1}}$	-	$5.47 \cdot 10^{-3}$	$1.66 \cdot 10^{-2}$	$5.88 \cdot 10^{-3}$	$1.61 \cdot 10^{-2}$
Proposed Model (Oxygen, Linear)	$a_{fitting}$, $b_{fitting}$ / $\mathrm{m^3\,s^{-1}\,A^{-1}}$, $\mathrm{m\,s^{-1}}$	-	$-3.36 \cdot 10^{-7}$, $1.17 \cdot 10^{-2}$	$-1.53 \cdot 10^{-1}$, $3.17 \cdot 10^{-1}$	$3.54 \cdot 10^{-3}$	$1.28 \cdot 10^{-2}$
Proposed Model (Oxygen, Square Root)	$a_{fitting}$ / $\mathrm{m^2/s/\sqrt{A}}$	-	$1.81 \cdot 10^{-9}$	$2.23 \cdot 10^{-9}$	$9.31 \cdot 10^{-3}$	$2.84 \cdot 10^{-2}$

between $0\,\mathrm{A\,cm^{-2}}$ and $2\,\mathrm{A\,cm^{-2}}$, capturing the full range of typical electrolyzer operation from low-load to high-load conditions.
For pressures where experimental data were available (1.15 and 8.5 bar), we used the corresponding pressure-specific parameter fits for the hydrogen and oxygen crossover models. For simulations at higher pressures (above 8.5 bar), we extrapolated using the parameter set fitted at 8.5 bar without further adjustment. This choice reflects the lack of experimental crossover data at pressures beyond 8.5 bar and the absence of a mechanistic model that fully captures the pressure dependence of transport phenomena such as gas solubility, membrane permeability, and electro-osmotic drag. We chose the 8.5 bar parameter set as the basis for extrapolation because it lies closer to the upper end of the investigated range and more likely reflects the nonlinear transport effects relevant to elevated-pressure operation. However, it is important to emphasize that predictions at pressures above 8.5 bar are extrapolations and should be interpreted with appropriate caution, particularly when used for quantitative design decisions.
While the models presented here were fitted separately to data at 1.15 bar and 8.5 bar, we did not evaluate whether a single parameter set could accurately predict crossover behavior across pressures. Such a test would provide a more rigorous assessment of whether the model structure itself captures pressure-dependent transport phenomena. However, due to the lack of experimental data at higher pressures, this evaluation could not be performed. Accordingly, extrapolations to pressures above 8.5 bar should be interpreted with additional caution. A more systematic evaluation of model generalization across pressure levels would require additional data and is beyond the scope of this study.

Hydrogen Crossover Behavior For hydrogen crossover, we employ the Trinke et al. [18] model (Eq. (3.18)), fitted to our measurement data. Here, we examine the concentration at the gas outlet of the separator, where both hydrogen and oxygen are present in the gas phase. To ensure safe operation, we set the acceptable concentration of hydrogen in oxygen below 2%, incorporating a safety margin relative to the 4% lower explosive limit [52].
Figure 3.5a illustrates the effect of pressure on hydrogen crossover, showing the predicted

molar fraction of hydrogen in the anode-side oxygen stream as a function of current density. At low current densities, hydrogen concentrations exceed the 2% safety threshold at nearly all pressure levels, except near atmospheric pressure. As current density increases, the relative hydrogen content decreases and eventually plateaus.

This trend is governed by two interacting effects. First, higher pressure enhances the diffusional driving force for hydrogen, thereby increasing crossover. Second, at low current densities, oxygen production is limited, amplifying the relative contribution of the crossover flux. Since hydrogen crossover declines only moderately with current, while oxygen production increases linearly, the relative hydrogen content remains disproportionately high at low loads.

Membrane thickness also strongly influences crossover behavior. As shown in Figure 3.5b, thinner membranes reduce diffusion resistance and lead to higher hydrogen concentrations, only the 50 µm membrane exceeds the 2% threshold at low current densities.

From a safety perspective, operating near atmospheric pressure or at sufficiently high current density is essential to avoid forming flammable mixtures. While thinner membranes improve efficiency by lowering ohmic losses, they also elevate gas crossover risks. Design strategies such as using thicker membranes can mitigate this trade-off, albeit at the cost of reduced electrical performance. These findings underscore the importance of balancing safety, efficiency, and gas purity through careful selection of membrane and operating conditions, particularly for industrial systems operating across a wide load range.

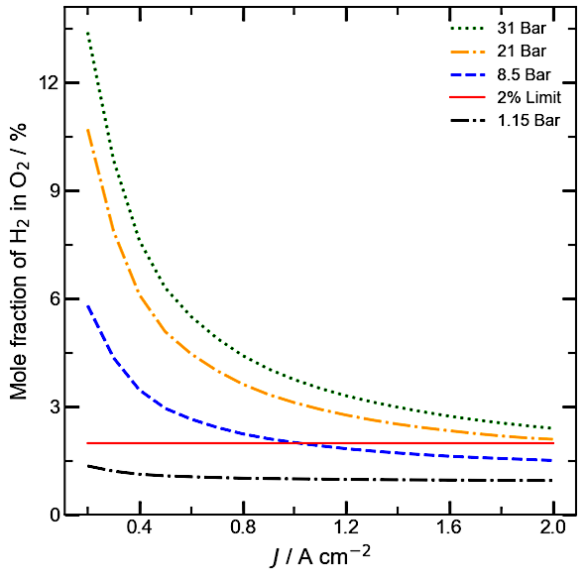

(a) Effect of pressure at constant membrane thickness (90 µm).

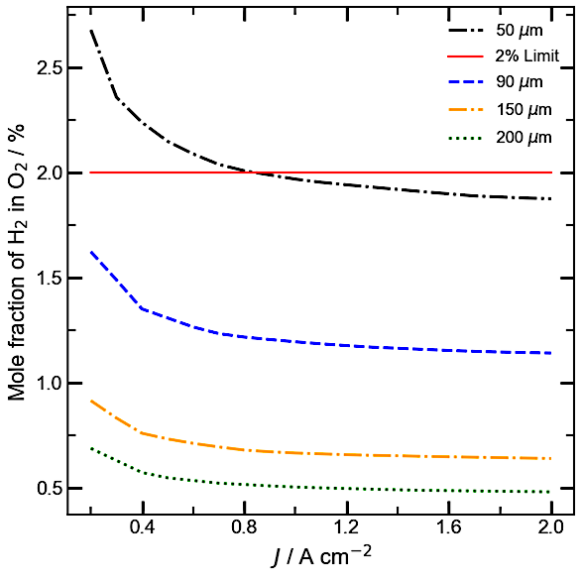

(b) Effect of membrane thickness at constant pressure (1.15 bar).

Figure 3.5.: Predicted molar percentage of H_2 in the O_2 gas leaving the separator using the Trinke et al. [18] model (Eq. (3.18)). Temperature is 60 °C; curves are interpolated between computed points. The horizontal line marks the 2 % safety limit for H_2 in O_2. Panel (a) uses parameters obtained by fitting to measurement data at both 1.15 bar and 8.5 bar. For simulations at pressures above 8.5 bar, the model employs the 8.5 bar fit without further adjustment. Panel (b) uses the parameter set fitted at 1.15 bar only. Hydrogen impurity in the oxygen outlet stream is reported in mol %, reflecting its safety relevance at the percent level.

Oxygen Crossover Behavior For oxygen crossover, we apply the model proposed herein (Eq.(3.24)), fitted to the measurement data. The goal is to minimize oxygen impurity in the product hydrogen stream, thereby avoiding costly purification processes and reducing membrane degradation associated with peroxide formation and subsequent Fenton reactions [11]. Unlike hydrogen in oxygen, small amounts of oxygen in hydrogen do not pose an immediate safety risk, as they remain well below flammability limits under typical operating conditions.

Figure 3.6 presents the simulated oxygen concentration in the cathode-side hydrogen stream as a function of anode pressure. At a fixed current density of, e.g., $0.2\,\mathrm{A\,cm^{-2}}$, oxygen concentrations rise steeply with increasing pressure, from a few hundred ppm at 1.15 bar to several thousand ppm at 31 bar. Notably, the dependence of oxygen concentrations in hydrogen on current density is opposite to that of hydrogen concentrations in oxygen: while hydrogen concentrations in oxygen decreases with increasing current density (see Section 3.4.2), oxygen concentration in hydrogen increases (see Figure 3.6). This difference arises from the distinct transport mechanisms governing each species. In the case of oxygen, higher current densities enhance electro-osmotic water drag, transporting larger amounts of dissolved oxygen across the membrane. As this convective flux scales with both current density and the local oxygen concentration, the resulting oxygen crossover increases nonlinearly with current density, whereas hydrogen production increases only linearly.

At elevated pressures, the solubility of oxygen increases, leading to a further nonlinear increase in crossover with pressure. This compounds the current density effect and underscores the importance of jointly considering both variables when evaluating oxygen impurity levels.

These findings highlight a key challenge: minimizing oxygen impurity in the hydrogen product stream under high-pressure operation, where gas separation becomes more costly and less efficient. For industrial applications, reducing oxygen crossover is critical to avoid downstream purification steps and to limit membrane degradation. The results presented here suggest that operating at lower anode pressures or employing thicker membranes may mitigate crossover, but must be weighed against efficiency penalties. The proposed model provides a valuable tool for guiding electrolyzer design trade-offs involving pressure, current density, membrane characteristics, and downstream purification requirements.

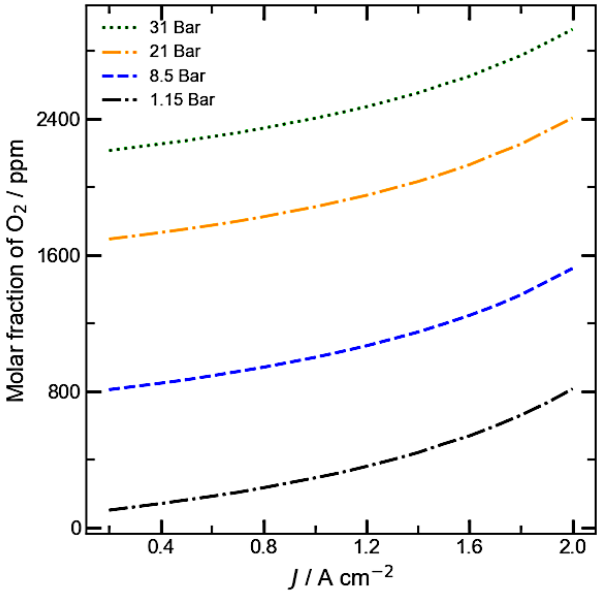

Figure 3.6.: Prediction of the molar fractions of oxygen in the hydrogen gas leaving the system, using the model proposed herein (Eq. (3.24)). The predictions are made by varying the pressure at a temperature of 60°C. Lower oxygen concentrations in the hydrogen product gas reduce the effort required for oxygen removal, which is achieved more effectively at lower anode pressures and current densities. Curves are interpolated between computed points. Parameters for both the 1.15 bar and 8.5 bar cases were obtained by fitting to measurement data. For simulations at pressures above 8.5 bar, the model uses the 8.5 bar fit without further adjustment. Oxygen impurity in the hydrogen outlet stream is reported in ppm, reflecting the different order of magnitude compared to hydrogen impurity in oxygen, as well as its relevance for product purity rather than safety considerations.

3.5. Conclusion & Outlook

In this chapter, hydrogen and oxygen crossover models are evaluated using experimental data obtained from a large-scale, high-pressure laboratory PEM electrolyzer operated under industrially-relevant conditions. While established hydrogen crossover models generally captured the observed trends, they fail to capture the observed nonlinear increase of oxygen crossover with current density, leading to under- or overestimation depending on the operating point.

To resolve this limitation, we proposed an oxygen crossover model that combines current density-dependent supersaturation in analogy to an existing H_2 crossover model with electro-osmotic water transport. The model demonstrated generally good agreement with the experimental data across the considered pressures and current density range, though deviations remained. Compared to existing approaches, the new formulation more accurately reproduces the nonlinear increase of crossover with increasing current density observed in the present experiments.

Overall, reliable crossover models enable more informed electrolyzer design by quantifying the trade-offs between gas purity, membrane thickness, operating pressure, and efficiency. In particular, they provide a means for identifying safe operating regions where gas crossover remains within acceptable limits without compromising energy performance.

These improvements in modeling may also help optimize the operation and maintenance of industrial electrolyzers by enabling more accurate monitoring and adjustment of operating conditions.
A limitation of this study lies in the treatment of temperature and pressure. All experiments were performed at a single temperature (60 °C), and the presented models therefore do not include explicit temperature dependence. Extending the dataset and model validation to variable-temperature conditions represents an important avenue for future work. In addition, although model parameters were fitted and validated separately at 1.15 bar and 8.5 bar, we did not assess whether a single set of parameters could reproduce crossover behavior across a wider pressure range. This is primarily due to the lack of experimental data at higher pressures, which prevents a systematic evaluation of model generalizability. As a result, extrapolations to higher pressures, beyond the validated range, should be interpreted with caution. Another limitation of this work is that water crossover was modeled but not experimentally validated. Future work should include direct measurement of water transport to complement the validation of hydrogen and oxygen crossover models.
Future work should also aim to incorporate gas recombination kinetics into the modeling framework to better capture losses due to catalytic reactions at the opposite electrode. Moreover, extending the model to one-dimensional spatial resolution could help resolve local gradients near the catalyst layer, especially under dynamic operating conditions. Further research should examine how electrolyzer components such as membrane thickness can be optimized to balance crossover, efficiency, and system-level trade-offs. For instance, thicker membranes reduce crossover but increase ohmic resistance, while higher pressures and current densities can intensify crossover but reduce compression costs. Balancing these factors is essential for achieving optimal electrolyzer performance.
Extending crossover models to also incorporate transport through hydrophobic domains, as suggested by Schalenbach et al. [42], represents a worthwhile direction for future work, particularly when considering low-hydration operating conditions. Finally, future studies should include experimental validation at elevated pressures and the development of models that capture pressure effects without requiring parameter re-fitting, thereby enabling broader predictive capability.
The crossover analysis in this chapter quantifies the hydrogen and oxygen transport across the membrane, as a function of the operating conditions. This transport affects gas purity, safety margins, and the availability of oxidizing species. As discussed in Chapter 2, chemical membrane degradation in PEM electrolyzers is governed by radical-driven pathways that require both an oxidant source (e.g., H_2O_2 formed from oxygen crossover) and catalytic metal ions. The following chapter therefore focuses on ion exchange as a system-level approach to control dissolved iron impurities and mitigate Fenton-type degradation mechanisms.

4. Multi-Species Ion Exchange Modeling for Iron Removal

4.1. Introduction

As shown in Chapter 2, chemical membrane degradation in PEM electrolyzers is governed by radical-driven pathways, with the Fenton reaction playing a central role. While Chapter 3 quantified hydrogen and oxygen crossover, which governs the availability of oxidizing species relevant to radical formation, the presence of catalytic metal ions remains an independent and critical factor controlling degradation intensity.

In practical PEM electrolyzer systems, iron ions enter the process water due to corrosion of metallic components in the cell hardware and balance-of-plant. Once present in the membrane environment, dissolved Fe^{2+}/Fe^{3+} ions catalyze the decomposition of hydrogen peroxide into highly reactive radicals, thereby accelerating chemical membrane degradation. Controlling iron contamination is therefore a necessary complement to managing gas crossover when aiming to mitigate Fenton-type degradation mechanisms.

This chapter focuses on ion exchange as a system-level strategy to remove dissolved iron impurities from the process water of PEM electrolyzers. A mechanistic ion exchange model is developed to describe the competitive adsorption and transport of Fe^{2+} and Fe^{3+} ions, providing a quantitative framework for assessing impurity removal performance and its implications for long-term membrane durability.

Ion exchange is a widely applied end-of-pipe water treatment technique for removing dissolved metal ions from aqueous streams. Ion exchangers consist of porous matrices bearing functional groups that selectively bind ionic species from solution, enabling targeted removal of impurities such as iron ions from electrolyzer process water [53].

The kinetics of ion exchange processes are described by the capacity of the ion exchange materials (i.e., the mass of currently adsorbed adsorbate per mass of adsorbent), which is calculated using adsorption rate constants and equilibrium via the adsorption isotherm [54, 55]. At a low capacity, the functional groups are charged with compensating ions. When ions from a solution come into contact with the adsorbent, one or more balancing ions may be released as the adsorbed ion establishes a connection with the new free space [53]. Multicharged ions can form chelating bonds with multiple active groups. Temperature affects the kinetics of the process and the equilibrium by influencing adsorption and desorption rates [56]. The hydrogen ion concentration (which determines pH) affects the maximum capacity, since hydrogen ions interact with the functional groups of cation exchangers [57].

Despite the widespread use of ion exchangers for water purification, current models do not adequately capture the specific dynamics of iron ion removal in PEM electrolyzer systems. Most existing ion exchange models focus on single-species behavior or generic multi-species systems, and do not reflect the transient, competitive adsorption processes between Fe^{2+} and Fe^{3+} ions under electrolysis conditions. Furthermore, these models often omit the dy-

namic oxidation of Fe^{2+} to Fe^{3+} and their spatial displacement within the ion exchange bed. To address this gap, we develop and validate a dynamic and spatially resolved multi-species ion exchange model that explicitly captures the competitive adsorption and replacement of Fe^{2+} by Fe^{3+}. The model is tailored to conditions relevant for PEM water electrolysis and is calibrated against new experimental data to ensure practical applicability.

To examine and predict the specific adsorption behavior, numerical simulations based on mathematical models are useful. In batch experiments, pseudo-first-order and pseudo-second-order rate equations are commonly employed to describe the change in adsorption capacity over time, where the ion concentration in the liquid phase is measured periodically. Typically, kinetic rate constants are fitted to experimental data [55]. Azizian's work [58] offers a theoretical approach to derive kinetic rate constants for pseudo-first and pseudo-second order reactions, combining adsorption and desorption rates. The theory aligns well with experimental data.

In a continuous ion exchange process, the ion exchange material is filled in a packed bed. Concentration and capacity gradients occur as a result of ion adsorption. For single-species adsorption, the Thomas model [59] can be used to predict the breakthrough curve [60].

While most models in the open literature are designed to simulate the removal of a single ion, Melis et al. [21] introduced a model to address the competitive adsorption of multiple species in multi-species systems which, after fitting, showed good agreement to experiments. Van Assche et al. [22] improved the extended Langmuir multi-species model by accounting for the effect of the size of the adsorbate molecules for species with Langmuir adsorption behavior. This model can be used to simulate multi-species behavior. Both models provide valuable foundations for capturing competition among multiple ionic species, yet neither focuses on iron speciation relevant to PEM electrolysis, nor the unique replacement dynamics of Fe^{2+} by Fe^{3+} ions.

In this work, we extend these concepts and specifically incorporate the replacement of weaker Fe^{2+} ions by the stronger Fe^{3+} ions in the context of water refinement loops for PEM electrolyzers. Existing multi-species models have not been specifically tailored or validated for ion exchangers operating under conditions relevant to PEM electrolyzer systems. PEM electrolyzers present distinct challenges, such as fluctuating concentrations of Fe^{2+} and Fe^{3+} ions due to dynamic corrosion and oxidation processes, which are not adequately captured by current models. In particular, they do not capture the competitive adsorption behavior of Fe^{2+} and Fe^{3+} ions, including the process where Fe^{2+} ions are displaced by Fe^{3+} ions over time. This competitive adsorption affects the dynamic interactions between an electrolyzer and an ion exchanger, where the ion input fluctuates, and Fe^{2+} ions enter through corrosion and are oxidized to Fe^{3+}. Both ions contribute to degradation reactions inside the cell, impacting overall efficiency and lifespan.

Thus, a model is needed to capture the dynamic and spatial behavior within the ion exchanger, as well as to account for the competitive adsorption of Fe^{2+} and Fe^{3+} ions, which influence each other's adsorption and affect the ion concentrations in the system. This type of model can predict key characteristics such as breakthrough curves, time until exhaustion, and performance under various operating conditions. To the best of our knowledge, no existing ion exchanger models specifically address the removal of Fe^{2+} and Fe^{3+} ions in the context of PEM electrolysis or adequately describe their interactions with the ion exchange material used in this study.

To address this challenge, we present a model that captures the interactions between iron ions and the ion exchange material under conditions relevant to PEM electrolyzer

systems. Our ion exchanger model is developed by extending the single-species Thomas model [59] using the multi-species Langmuir model [61], enabling us to simulate the competitive adsorption and dynamic replacement of weaker ions (Fe^{2+}) by stronger ions (Fe^{3+}). In contrast, while the approaches of Melis et al. [21] and Van Assche et al. [22] also address multi-species Langmuir systems, they do not explicitly capture the replacement of weaker ions by stronger ions.

We calculated key adsorption parameters based on measurements (e.g., Langmuir constants and maximum capacities) specifically for Fe^{2+} and Fe^{3+} removal using commonly used ion exchanger materials, like Lewatit TP 207®, providing previously unavailable data on the interaction between this material and Fe^{2+} and Fe^{3+} ions. To further refine the model, we fitted the surface diffusivity parameters to our experimental data, as described in detail in Section 4.3. The fitting showed good agreement between the simulated and observed results. By integrating this enhanced ion exchange model with a simplified iron ion concentration source term that accounts for the amount of Fe-ions added to the stream by the electrolyzer, we can analyze ion dynamics without the need for a full-blown electrolyzer model. In other words, the electrolyzer model does not consider electrochemical reactions, such as hydrogen (H_2) and oxygen (O_2) production. This targeted simplification increases the model's computational efficiency by focusing solely on the ion exchange processes critical for Fe^{2+} and Fe^{3+} removal. The omission of these electrochemical reactions introduces only a negligible error because they have minimal impact on the overall iron ion dynamics within the system under the operating conditions studied.

The ion exchange process is modeled under constant flow conditions with ideal mixing in the liquid phase, assuming adsorption behavior dictated by multi-species Langmuir isotherms. The ion exchanger is axially discretized into sections using the 1D finite volume method to capture the spatial distribution of ions. By combining the ion exchanger model with a model for the iron ion source in electrolyzer, we capture the dynamics of ion concentration and the interactions between these species within the PEM electrolyzer system. This approach, also considering the effects of temperature, pH, and ion selectivity on the ion exchange process.

The experimental setup, which used Lewatit TP 207® as the ion exchange material, maintained a constant temperature and flow rate to replicate the conditions within the electrolyzer system. Corrosion and oxidation rates were based on literature, providing the basis for simulating iron ion input and interaction within the system. These boundary conditions allowed for accurate simulation of breakthrough curves, offering insights into the design and operation of the ion exchanger in combination with the electrolyzer, enhancing performance predictions and operational lifespan estimations.

The remainder of this chapter is organized as follows: Section 4.2 describes the development of the multi-species ion exchanger model and the model for the iron ion source in the electrolyzer. Section 4.3 outlines the experiments conducted, and explains how the model was fitted to the experimental data. In Section 4.4, simulation results are presented for a case study examining the performance of ion exchange within an electrolyzer system. This section includes simulations of breakthrough curves to analyze the competitive adsorption behavior of Fe^{2+} and Fe^{3+} ions, a sensitivity analysis to determine the effect of varying operating parameters (such as flow rate, initial loading, and corrosion intensity) on the ion exchange process, and simulations of long-term performance to predict the ion exchanger's behavior under continuous operation over time. Finally, Section 4.5 concludes the chapter with a summary and outlook.

4.2. Model Description

This section presents the multi-species ion exchange model, adapted from existing models and integrated with a simplified iron ion source. It aims to predict key characteristics of the ion exchanger, such as breakthrough curves and time until exhaustion, while also enhancing the understanding of the competitive adsorption behavior between Fe^{2+} and Fe^{3+} ions. The model's surface diffusivity parameters were fitted to our experimental data, ensuring its suitability for the specific interactions of Fe^{2+} and Fe^{3+} ions with the ion exchanger material. The model has been implemented in Python.

The overall system model consists of two main components: a simplified iron ion source representing the electrolyzer (index E) and an ion exchanger model (index IE), focusing on ion dynamics specific to the integration of these systems, as shown in Figure 4.1.

A stream of water with a volumetric flow rate, $\dot{V}$, containing Fe^{2+} and Fe^{3+} ions, flows from the electrolyzer to the ion exchanger and vice-versa. The volumetric flow rate $\dot{V}$, is assumed to remain constant throughout the system (inlet equals outlet), as the concentration of iron ions is small and does not significantly alter the density of the water. In the ion exchanger, the competitive adsorption of Fe^{2+} and Fe^{3+} ions is modeled, and a portion of these ions is removed. As a result, the flow returning to the electrolyzer has reduced levels of Fe^{2+} and Fe^{3+} ions. The model captures the time-variable behavior of the ion concentrations within the ion exchanger, allowing for predictions of iron ion levels across different sections of the ion exchanger and the influence of process parameters on adsorption efficiency.

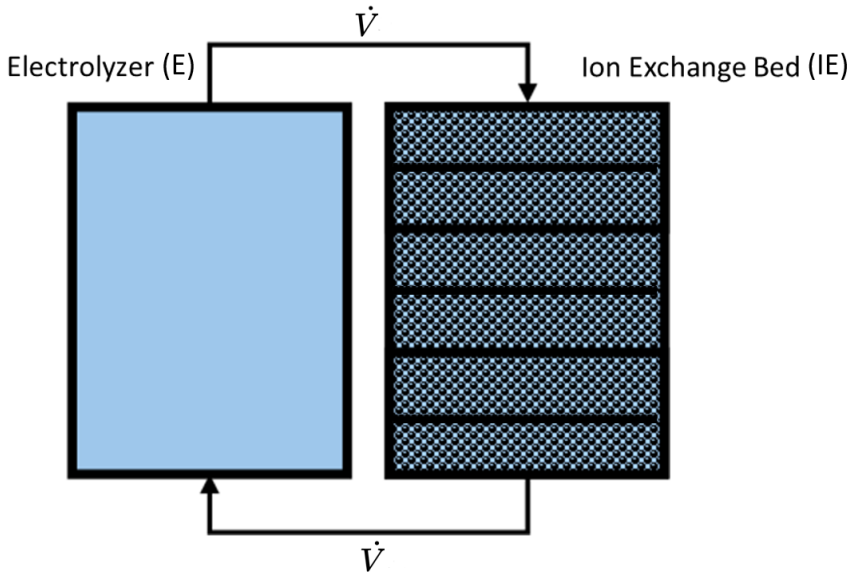

Figure 4.1.: General model structure: On the left, the model for the iron ion source in electrolyzers, and on the right, the ion exchanger model divided into sections. Water, containing iron ions, flows from the electrolyzer to the ion exchanger at a volumetric flow rate $\dot{V}$ and then returns to the electrolyzer.

4.2.1. Modeling of the Iron Ion Source in Electrolyzers

The model for the iron ion source in electrolyzers is a simplified approach only designed to capture the changes in iron concentration within the electrolyzer. The electrolyzer is treated as a single control volume representing the liquid phase, where iron ions are ideally mixed in a fixed water volume, V_{E}; this simplification is due to the lack of detailed geometrical information about the electrolyzer. It allows the model to focus on average concentration changes rather than resolving spatial variations, which are not essential for this analysis. By using such a lumped-parameter model, the overall behavior of the system is captured.

The model includes a source term for Fe^{2+} ions, representing corrosion occurring on the surfaces of pipes, tanks, and other stainless steel components. The corrosion rate is based on the literature, with the surface area for corrosion estimated based on an equivalent pipe surface area. Additionally, Fe^{2+} ions are oxidized to Fe^{3+} ions within the electrolyzer cell, modeled by an oxidation term. The model excludes other species and electrochemical processes within the cell. Corrosion rates for stainless steel, including both non-welded and gas tungsten arc welded (GTAW) conditions, are based on measurements reported by Bernardi et al. [62]. These corrosion rates r_c are used in the sensitivity analysis, ranging from 2.14 to 10.36 $\mu\mathrm{m\,yr}^{-1}$.

According to Benson et al. [63], corrosion primarily releases Fe^{2+} ions into the solution, with OH^- ions also generated to maintain electrochemical neutrality. The source term for Fe^{2+} inside the electrolyzer control volume is calculated via

$$R_{\mathrm{Fe^{2+},cr}} = A_{\mathrm{pipes}} r_c \rho_{\mathrm{316L}},$$

with the specific pipe surface area per water volume A_{pipes}, corrosion rate r_c and density $\rho_{\mathrm{316L}} = 7.9\,\mathrm{kg\,L}^{-1}$ for common stainless steel 316L [64]. The specific pipe surface area is calculated via the ratio of surface to volume $A_{\mathrm{pipes}} = \frac{4}{d_{\mathrm{pipes}}}$ assuming a cylinder with an estimated average pipe diameter of $d_{\mathrm{pipes}} = 0.5\mathrm{m}$, taking into account the different sizes of equipment and pipe diameters in typical electrolyzers. The oxidation of Fe^{2+} ions to Fe^{3+} inside the system is simplified here by calculating the oxidation rate constant via [63]

$$k_{\mathrm{ox}} = \begin{cases} 10^{-3.9}\,\mathrm{d}^{-1}, & \mathrm{pH} < 3.75 \\ 10^{\;2.02\mathrm{pH}\,-\,11.77}\,\mathrm{d}^{-1}, & \mathrm{pH} \geq 3.75. \end{cases}$$

Based on the corrosion term for Fe^{2+} and the oxidation term for Fe^{3+} formation, the overall source terms for the iron ions in the electrolyzer are:

$$R_{\mathrm{Fe^{2+},E}} = R_{\mathrm{Fe^{2+},cr}} - k_{\mathrm{ox}}\, c_{\mathrm{Fe^{2+},E}},$$
$$R_{\mathrm{Fe^{3+},E}} = k_{\mathrm{ox}}\, c_{\mathrm{Fe^{2+},E}},$$

where $c_{i,\mathrm{E}}$ denotes the concentration of ion i in the electrolyzer system.

The source terms in this model thus depend on the concentrations in the electrolyzer. These in turn are also influenced by the volumetric flow rate of water $\dot{V}$ (assumed constant) coming from the ion exchanger, as well as the concentrations of the ions i at the outlet of the ion exchanger (c_i, IE). Thus, the iron ion concentrations in the electrolyzer, $c_{i,\mathrm{E}}$, are calculated by a mass balances assuming ideal mixing:

$$\frac{dc_{i,\mathrm{E}}}{dt} = \frac{\dot{V}}{V_{\mathrm{L,E}}} \left(c_{i,\mathrm{IE}} - c_{i,\mathrm{E}}\right) + R_{i,\mathrm{E}}, \tag{4.1}$$

with the liquid volume in the electrolyzer $V_{\mathrm{L,E}}$, exchange volumetric flow rate $\dot{V}$ and the concentration $c_{i,\mathrm{IE}}$ in the stream coming from the ion exchanger for the iron ions $i = \mathrm{Fe}^{2+}, \mathrm{Fe}^{3+}$.

4.2.2. Modeling of the Ion Exchange Bed

To model the ion exchange process, it is essential to consider both the solid and liquid phases. As shown in Figure 4.2, the model accounts for the volume of ion exchange particles V_{IE}, the fluid volume within the voids V_{L}, and the superficial fluid velocity v_{super}, which represents the volumetric flow rate of the fluid per unit cross-sectional area of the exchanger, i.e, $v_{\mathrm{super}} = \frac{\dot{V}}{A}$, where A is the cross-sectional area, including both liquid and solid phases.

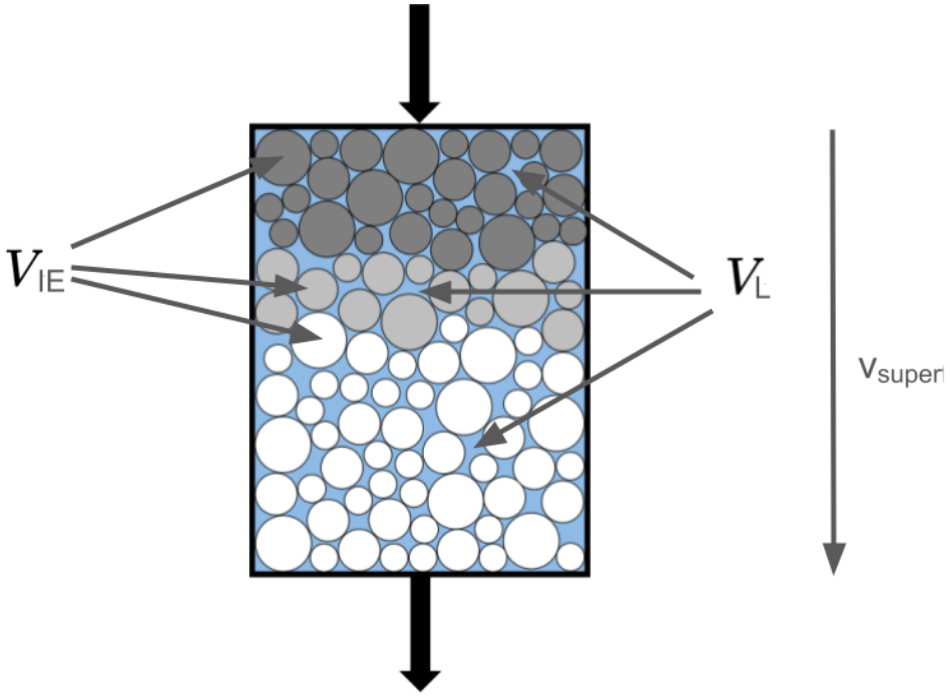

Figure 4.2.: Schematic representation of the ion exchange bed model. V_{IE} denotes the volume of the ion exchange particles, V_{L} represents the volume of fluid within the void spaces, and v_{super} is the superficial fluid velocity. The darker ion exchange particles represent full saturation with adsorbate, the lighter ones partial saturation with remaining capacity, and the white ones no loading; overall the figure illustrates a saturation gradient where particles near the inlet saturate first.

The key underlying phenomena in the liquid phase are advection and interaction with the adsorbent phase. We model the ion exchange bed by dividing it into multiple dynamic control volumes (sections) along its length, each representing a segment of the bed where ion concentrations and adsorption/desorption processes are monitored. The one-dimensional representation is motivated by the need to reduce computational complexity, as 2D or 3D modeling would be too resource-intensive for the simulation. The justification for focusing on axial transport is the slow, steady flow typical in ion exchangers, resulting in longer ion exchange times. In a specific packed bed setup, ion removal happens uniformly across

many small granules throughout the bed, not just at the walls, which minimizes radial gradients. In the following, we first outline the standard techniques for related transport phenomena and adsorber modeling that are common for single-species systems, before deriving the extension to multi-species systems that is required for our application.

4.2.2.1. Single-species Systems

We begin with the total mass balance equation, which inherently accounts for both the liquid and solid phases. Following Sherwood [65], the overall mass balance is given in the differential form:

$$\epsilon_b \frac{\partial c_i}{\partial t} + \rho_\mathrm{b} \frac{\partial q_i}{\partial t} + v_\mathrm{super} \frac{\partial c_i}{\partial z} = 0, \tag{4.2}$$

where $c_i(t, z)$ denotes the mass concentration of ion i (i.e., Fe^{2+} or Fe^{3+}) in the liquid phase as a function of time t and position z, and $q_i(t, z)$ represents the adsorbed capacity (i.e., the mass of adsorbed ions per mass of adsorbent) also as a function of time t and position z. The bulk density of the adsorbent bed, ρ_b, represents the mass of the adsorbent per total bed volume (V_IE+V_L). The bed porosity ϵ_b is defined as $\epsilon_b = \frac{V_\mathrm{L}}{V_\mathrm{IE}+V_\mathrm{L}}$.
Since the total mass balance already represents both the liquid and solid phases, it forms the primary governing equation. To close the system, we use the exchange rate R_i that links the change in the solid loading q_i to the overall balance. This ensures that both c_i and q_i evolve consistently. For each ion i, the solid-phase relation is given by:

$$\rho_b \frac{\partial q_i}{\partial t} = R_i, \tag{4.3}$$

where $R_i(t, z)$ is the exchange rate of ion i, i.e., the net rate at which ions are adsorbed onto or desorbed from the solid phase at time t and position z. By substituting $\rho_b \frac{\partial q_i}{\partial t} = R_i$ back into the total mass balance equation (4.2), we express the governing equation in terms of c_i and R_i. Although the resulting equation appears to focus primarily on the liquid-phase concentration c_i, it still represents total mass conservation since R_i inherently accounts for the solid phase. By keeping R_i as an algebraic variable, we retain the flexibility to modify it later (e.g., for multi-species systems). Together with the solid-phase balance (4.3), this formulation yields a coupled system that captures the dynamics of both phases.
To approximate R_i under the given conditions, we use the Thomas model [59], which provides a constitutive relationship for the kinetics of ion adsorption and desorption:

$$R_i = k'_\mathrm{kin} \left(c_i \left(q_{\mathrm{max},i} - q_i \right) - \frac{q_i}{K_{\mathrm{L},i}} \right), \tag{4.4}$$

where k'_kin is the adsorption rate constant, $c_i(t, z)$ is the concentration of the adsorbate in the liquid, $q_{\mathrm{max},i}$ is the maximum adsorption capacity of the given adsorbent material, $q_i(t, z)$ is the capacity and $K_{\mathrm{L},i}$ is the Langmuir constant. While the Thomas model is limited to single-species systems, it forms the basis for our work and is adapted in Section 4.2.2.2 to capture multi-species dynamics, incorporating competitive adsorption effects. A detailed derivation of the adsorption rate constant and associated transport parameters is provided in Appendix C.

4.2.2.2. Extension to Multi-species Systems

While multi-species adsorption has been studied by Melis et al. [21] and Van Assche et al. [22], these approaches do not explicitly consider the continuous replacement of weaker ions (Fe^{2+}) by stronger ions (Fe^{3+}), which is crucial in PEM electrolyzer systems. In the present system, the strong Fe^{3+} ions have a higher equilibrium capacity and their adsorption is thermodynamically preferred to that of the weak Fe^{2+} ions. Initially, the strong ions are adsorbed in the first parts near to the inlet of the ion exchanger, blocking the adsorption sites for the weak ions. The weak ions are thus initially adsorbed further downstream in the ion exchanger. Over time, if the influx of new strong ions does not stop, these weak ions are replaced by strong ions. During this replacement, more weak ions are replaced in the last sections of the bed and more weak ions are released than adsorbed for a short time, causing the outlet concentration to temporarily exceed the inlet concentration and resulting in a peak for the breakthrough curve of Fe^{2+} ion [66].
To the best of our knowledge, there are no models that can be used in the case of iron ion exchangers to include multi-species adsorption and accurately capture the replacement of weak ions by strong ones. To fill this gap, we take the fundamental Thomas model, which is designed for the adsorption of single species, and extend this model to the simultaneous adsorption of multiple ions (Fe^{2+} and Fe^{3+}), including the competitive adsorption behavior. To develop the multi-species adsorption model, we start from the multi-species Langmuir equilibrium model [61]:

$$q_{\mathrm{e},i} = q_{\mathrm{max},i} \frac{K_{\mathrm{L},i} c_i}{1 + K_{\mathrm{L},i} c_i + \sum_{j \neq i} (K_{\mathrm{L},j} c_j)}, \tag{4.5}$$

where $q_{\mathrm{e},i}(t, z)$ is the equilibrium capacity. To simplify the examination of the upcoming modifications, especially weak ion replacement, we reorganize Equation (4.5) to obtain:

$$q_{\mathrm{e},i} \left(\frac{1}{K_{\mathrm{L},i}} + c_i + \frac{1}{K_{\mathrm{L},i}} \sum_{j \neq i} (K_{\mathrm{L},j} \mathrm{c}_j) \right) = q_{\mathrm{max},i} c_i,$$

and further into:

$$0 = c_i (q_{\mathrm{max},i} - q_{\mathrm{e},i}) - \frac{q_{\mathrm{e},i}}{K_{\mathrm{L},i}} - \frac{q_{\mathrm{e},i}}{K_{\mathrm{L},i}} \sum_{j \neq i} (K_{\mathrm{L},j} c_j). \tag{4.6}$$

The first two terms are equivalent to the driving-force term in the single-species Thomas model, cf. right-hand side of (4.4), except that (4.6) uses the equilibrium capacity $q_{e,i}$ while (4.4) uses the actual (potentially non-equilibrium) capacity q_i. The last term in Equation (4.6) includes the effect of competitive adsorption in multi-species systems. Based on this, a straightforward extension of the Thomas model to multi-species systems would be:

$$R_i = k'_{\mathrm{kin}} \left(c_i (q_{\mathrm{max},i} - q_i) - \frac{q_i}{K_{\mathrm{L},i}} - \frac{q_i}{K_{\mathrm{L},i}} \sum_{j \neq i} (K_{\mathrm{L},j} c_j) \right) \tag{4.7}$$

However, such a model cannot adequately describe the replacement of weak ions (e.g., Fe^{2+}) by strong ions (e.g., Fe^{3+}), as it assumes equal probabilities of site occupancy for all ions, regardless of their binding strength. Strong ions, such as Fe^{3+}, exhibit preferential adsorption due to their higher charge density and greater electrostatic attraction to exchange sites. This behavior arises from differences in ion hydration energies and

charge-to-radius ratios, which influence the thermodynamics of ion exchange. Competitive adsorption processes like this are well-described in studies on Langmuir adsorption and ion exchange thermodynamics [61, 67].
Therefore, we propose a modification of the driving force term of the following form:

$$R_i = k'_{\mathrm{kin}} \left(c_i \left(q_{\mathrm{max},i} - q_i \right) - \frac{q_i}{K_{\mathrm{L},i}} - K_{\mathrm{BC}} \frac{q_i}{K_{\mathrm{L},i}} \sum_{j \neq i} K_{\mathrm{L},j} c_j \right) \tag{4.8}$$

by introducing the *replacement factor* K_{BC}, which is a function of the capacities $q_i(t, z)$. For the functional form of K_{BC}, we use the boundary conditions that $K_{\mathrm{BC}} \approx 0$ for low capacities, where competition is irrelevant since there are many available free adsorption positions, and $K_{\mathrm{BC}} = 1$ at equilibrium, where competition is governed by the multi-species equilibrium according to (4.6). More specifically, based on schematic diagrams from theoretical studies [66], which illustrate the typical behavior of competitive adsorption between weaker and stronger ions, we assume the following functional form:

$$K_{\mathrm{BC}} = \left(\frac{\sum_i q_i}{\sum_i q_{\mathrm{e},i}} \right)^{n_{\mathrm{BC}}} \tag{4.9}$$

$$n_{\mathrm{BC}} = n_{\mathrm{BC},0} \left(1 - \frac{\sum_i q_i}{\sum_i q_{\mathrm{e},i}} \right), \tag{4.10}$$

with $n_{\mathrm{BC},0}$ as an adjustable parameter. This form of K_{BC} is motivated by its ability to capture the nonlinear progression of competitive adsorption observed in theoretical replacement curves [66], which show a transition from negligible competition at low adsorbent loading to full competition as equilibrium is approached. To reproduce this characteristic shape in simulations, we introduced a dynamically decreasing exponent n_{BC} that modulates the replacement intensity as a function of current versus equilibrium loading.
Initial trials with simpler alternatives, such as a constant exponent or a linear scaling of K_{BC}, were unable to match both the steep onset of competition and its saturation near equilibrium. In particular, a constant n_{BC} could not replicate the overshoot of Fe^{2+} breakthrough curves, which depend on localized replacement dynamics. The selected formulation introduces only a single adjustable parameter $n_{\mathrm{BC},0}$ while respecting the correct boundary behavior, and thus provides the minimal nonlinear structure necessary to capture the observed and theoretical dynamics of competitive ion replacement.
Table 4.1 summarizes the main model equations and assumptions for clarity and quick reference. Additional components, including corrosion, oxidation, and adsorption kinetics, are detailed in Section 4.2.1 and Appendix C.

Table 4.1.: Main equations and modeling assumptions used in the ion exchange system model.

Model Component	Equation or Assumption
Electrolyzer mass balance	$\frac{dc_{i,\mathrm{E}}}{dt} = \frac{\dot{V}}{V_{L,\mathrm{E}}}(c_{i,\mathrm{IE}} - c_{i,\mathrm{E}}) + R_{i,\mathrm{E}}$ (Eq. 4.1)
1D mass balance in exchanger	$\epsilon_b \frac{\partial c_i}{\partial t} + \rho_b \frac{\partial q_i}{\partial t} + v_{\mathrm{super}} \frac{\partial c_i}{\partial z} = 0$ (Eq. 4.2)
Solid-phase loading balance	$\rho_b \frac{\partial q_i}{\partial t} = R_i$ (Eq. 4.3)
Single-species exchange rate	$R_i = k'_{\mathrm{kin}} \left(c_i(q_{\mathrm{max},i} - q_i) - \frac{q_i}{K_{\mathrm{L},i}} \right)$ (Eq. 4.4)
Multi-species Langmuir equilibrium	$q_{\mathrm{e},i} = q_{\mathrm{max},i} \frac{K_{\mathrm{L},i} c_i}{1 + K_{\mathrm{L},i} c_i + \sum_{j \neq i} K_{\mathrm{L},j} c_j}$ (Eq. 4.5)
Extended Thomas model (multi-species)	$R_i = k'_{\mathrm{kin}} \left(c_i(q_{\mathrm{max},i} - q_i) - \frac{q_i}{K_{\mathrm{L},i}} - K_{\mathrm{BC}} \frac{q_i}{K_{\mathrm{L},i}} \sum_{j \neq i} K_{\mathrm{L},j} c_j \right)$ (Eq. 4.8)
Replacement factor	$K_{\mathrm{BC}} = \left(\frac{\sum_i q_i}{\sum_i q_{\mathrm{e},i}} \right)^{n_{\mathrm{BC}}}$ (Eq. 4.9)
	$n_{\mathrm{BC}} = n_{\mathrm{BC},0} \left(1 - \frac{\sum_i q_i}{\sum_i q_{\mathrm{e},i}} \right)$ (Eq. 4.10)

Modeling Assumptions

The ion exchanger is modeled in one dimension along the axial direction.

The volumetric flow rate $\dot{V}$ is uniform across the entire system.

The electrolyzer is assumed to be ideally mixed with no spatial gradients.

Electrochemical reactions such as H_2 and O_2 generation are not included.

Only Fe^{2+} and Fe^{3+} ions are considered in the model.

4.2.3. Model Implementation and Discretization

The model of the overall system consists of the iron ion source in electrolyzers and the ion exchanger model. It contains ordinary differential equations (ODEs) for the iron ion concentration in the electrolyzer and both ordinary and partial differential equations (PDEs) for the ion exchanger.

To solve the partial differential equations in the ion exchanger, we use the method of lines by discretizing the spatial domain of the ion exchanger into N sections using a 1D finite volume approach. This transforms the partial differential equations governing mass transport and adsorption into a system of ordinary differential equations. These are then solved together with the ordinary differential equations of the electrolyzer.

The method of lines with finite volume discretization is a classical and robust approach for one-dimensional reactive transport problems and provides stable and accurate results for the current application. As the primary focus of this work is the development and validation of the multi-species ion exchange model, rather than numerical solution strategies,

more advanced discretization methods were not pursued. For discussions on numerical stiffness, solver stability, and alternative schemes such as nonstandard finite difference methods or finite element methods, we refer interested readers to standard textbooks on numerical methods [68] and, for the foundational development of nonstandard finite difference (NSFD) schemes, to the monograph by Mickens [69], as well as representative expository works [70, 71].
In the implementation, we start from the total mass balance equation (4.2), which inherently accounts for both the liquid and solid phases. Discretizing it along the length coordinate z of the ion exchanger, for each species i and section k, we obtain:

$$A\,\Delta z\,\epsilon_{\mathrm{b}}\frac{dc_{i,k}}{dt} + \rho_{\mathrm{b}}\,A\,\Delta z\,R_{i,k} + \dot{V}(c_{i,k} - c_{i,(k-1)}) = 0, \tag{4.11}$$

where A is the cross-sectional area of the ion exchanger, and Δz is the length of the finite volume in the z-direction. To ensure stability and accuracy in advection-dominated flow, we apply the upwind scheme to the convective term from Eq. (4.2). Additionally, the solid-phase mass balance (4.3) is discretized for each species i and section k as

$$\frac{dq_{i,k}}{dt} = \frac{R_{i,k}}{\rho_b}. \tag{4.12}$$

In both (4.11) and (4.12), the rate $R_{i,k}$ is determined from the chosen kinetic model, especially (4.8), with the local $q_{i,k}$, $c_{i,k}$.
To solve the set of ordinary differential equations (4.1), (4.11) and (4.12), we use the Forward Euler method. Although the Forward Euler method is not the best method for solving ODEs [72], it was chosen for its ease of implementation. To ensure numerical stability and accuracy, we started with a Courant–Friedrichs–Lewy number of 1, resulting in an upper time step bound of $\Delta t = \frac{A\Delta z}{\dot{V}}$, ensuring that the entire liquid volume is exchanged in each discrete step. A step size study was conducted (not shown here for brevity), in which the number of steps per minute was increased by factors of 2, 3, and up to 10. The results indicated that beyond a factor of 9, the solution changed by less than 1%, so a factor of 9 was used in all subsequent simulations.

4.3. Experiments and Parameter Fitting

This section outlines the experimental procedures used to study the adsorption of Fe^{2+} and Fe^{3+} ions on the adsorbent material Lewatit TP 207 ®. It was chosen due to its excellent adsorption properties for iron ions, availability, and the research team's prior laboratory experience with it. In the following, we first describe our equilibrium experiments to determine Langmuir constants and maximum capacity of the Lewatit TP 207 ® adsorbent. Afterwards, we discuss the measurement of breakthrough curves and results of fitting our model to this data.

4.3.1. Equilibrium Experiments

In this experiment, we determined the equilibrium capacity of Lewatit TP 207 ® for Fe^{2+} and Fe^{3+} at a temperature of 60°C. The Lewatit TP 207 ® was pretreated with strong acid to ensure its functional groups are fully protonated. First, we mixed a certain amount of iron sulfate with ultra pure water for 30 minutes. Then we made a first measurement of conductivity and pH using an EC meter (ISM 3/4" NPT 0.1C Ti 34mm, 2-Pol-LF sensor) and a pH meter (InPro3100i/SG/120), both normalized to 25°C. In a next step, Lewatit TP 207 ® in the form of solid beads was added to the solution. After a few minutes, the experiments showed a color change of the Lewatit TP 207 ®, indicating an exchange of ions, which is consistent with previous findings by Ahmetli et al. [73]. After 24 hours, measurements showed that there was no more change in conductivity, so we assume that the equilibrium conductivity had been reached. The results of these batch experiments after 24 hours, including initial and equilibrium conductivity and pH, are presented in Table 4.2.

Table 4.2.: Measured initial conductivity σ_0, conductivity at equilibrium state σ_e and pH in equilibrium state for 0.5 g of Lewatit TP 207 ® in 500 mL of ultrapure water (UPW) with the given initial iron ion concentrations. The total experimental error is estimated to be 1%.

		UPW	**Fe^{2+}**		**Fe^{3+}**	
			$50\,mg\,L^{-1}$	$500\,mg\,L^{-1}$	$50\,mg\,L^{-1}$	$500\,mg\,L^{-1}$
σ_0	$\mu S\,cm^{-1}$	0	223	1405	672	3085
σ_e	$\mu S\,cm^{-1}$	9.5	511	1806	764	3806
pH	-	4.7	2.96	2.73	2.68	1.99

From this measurement data, equilibrium concentrations of iron ions in the solution were computed using aqion® [74], an aqueous chemistry software package. Input parameters included the measured pH, measured conductivity values and the calculated molar concentrations of sulfate ions based on the initial amounts of dissolved iron salts. We iteratively adjusted the iron ion concentrations in the model until the charge neutrality condition was satisfied within an acceptable error margin (below 0.3%). The computed equilibrium concentrations and corresponding capacities are presented in Table 4.3.

Table 4.3.: Computed iron ion concentrations in the solution at equilibrium state $c_{e,i}$ and computed equilibrium capacities $q_{e,i}$ for Lewatit TP 207®in $500\,\mathrm{mL}$ UPW with the given initial iron ion concentrations via aqion®, open CO_2 system with its default parameter for partial pressure calculation of $pCO_2 = 3.408$. For the computation of the iron concentrations, the pH and conductivity values are taken from our measurements.

		$\mathbf{Fe^{2+}}$		$\mathbf{Fe^{3+}}$	
		$50\,\mathrm{mg\,L^{-1}}$	$500\,\mathrm{mg\,L^{-1}}$	$50\,\mathrm{mg\,L^{-1}}$	$500\,\mathrm{mg\,L^{-1}}$
$c_{e,i}$	$\mathrm{mg\,L^{-1}}$	13	388	3	170
$q_{e,i}$	$\mathrm{mg\,g^{-1}}$	37	112	47	330

To compute the maximum equilibrium capacity and Langmuir constants, the equilibrium concentration and capacity data points from Table 4.3 were inserted into the Langmuir model:

$$q_{e,i} = \frac{q_{max,i}\, K_{L,i}\, c_{e,i}}{1 + K_{L,i}\, c_{e,i}}.$$

This yields two equations each for Fe^{2+} and Fe^{3+} that can then be solved for the $K_{L,i}$ and $q_{max,i}$. The results are presented in Table 4.4 and illustrated in Figure 4.3.

Table 4.4.: Maximum capacities $q_{max,i}$ and Langmuir constants K_L calculated for Lewatit TP 207 ® from the equilibrium concentrations in Table 4.3.

		$\mathbf{Fe^{2+}}$	$\mathbf{Fe^{3+}}$
$q_{max,i}$	$\mathrm{mg\,g^{-1}}$	120	370
$K_{L,i}$	$\mathrm{L\,mg^{-1}}$	0.034	0.048

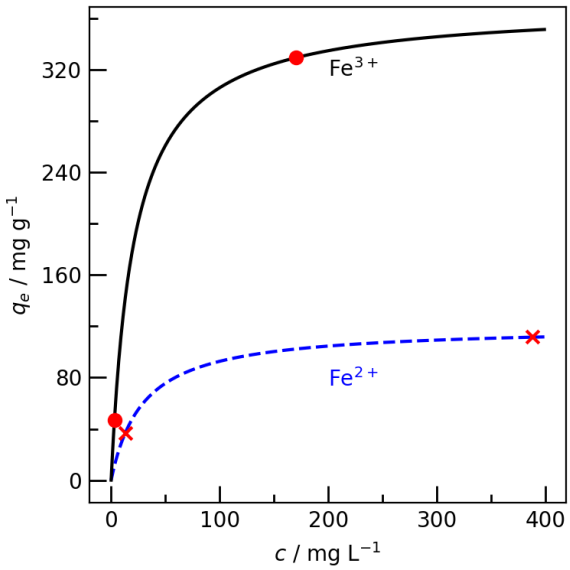

Figure 4.3.: Langmuir isotherms (lines) and equilibrium data points computed using parameters from Table 4.4, based on experimental results in Table 4.3.

In this step, we did not perform a detailed identifiability analysis, which can be found in classic parameter-estimation literature (e.g., [75, 76]).

4.3.2. Continuous Experiments and Parameter Fitting

The ion exchange model contains parameters, such as surface diffusivities, that are missing and difficult to measure directly. To address this, the parameters were estimated by fitting the model to experimental data. For this purpose, a simplified experimental setup was designed to replicate the processes occurring in the refinement loop of a PEM electrolyzer. In this setup, water is pumped from a tank into the ion exchange cartridge, with conductivity and pH measured before the cartridge inlet using an EC meter (ISM 3/4" NPT 0,1C Ti 34mm, 2-Pol-LF sensor) and a pH meter (InPro3100i/SG/120), both normalized to 25 °C. The entire system is housed within an oven to maintain a constant temperature of 60 °C, ensuring consistent operating conditions during the experiment.
The inlet stream passes through a backflow filter (consisting of two layers of fine mesh secured by sealing rings) before entering the cartridge, where the ion exchange particles reside. This design prevents ion exchange particle backflow when the pump is stopped. The flow moves through the cartridge, proceeds upward, and finally exits the cartridge.
A solution containing 50 mg L^{-1} each of Fe^{2+} and Fe^{3+} in 2 L of UPW was circulated with the ion exchange cartridge in bypass mode until the process temperature of 60°C was reached.
To validate the model described in Section 4.2, the material properties, experimental design data, and measured values are used to match the simulation to the experiment and the ion exchange material used. The corresponding parameter values are listed in Table 4.5.

Table 4.5.: Parameters values used for the fitting of the ion exchange model to experimental data.

Parameter	Symbol	Value
Effective particle diameter	d_p	550 µm [77]
Ion exchanger height	h	0.06 m
Langmuir constants	$K_\mathrm{L}^{\mathrm{Fe}^{2+}}$	$0.034\,\mathrm{L\,mg^{-1}}$
	$K_\mathrm{L}^{\mathrm{Fe}^{3+}}$	$0.048\,\mathrm{L\,mg^{-1}}$
Maximum capacity	$q_{\mathrm{max,Fe^{2+}}}$	$120\,\mathrm{mg\,g^{-1}}$
	$q_{\mathrm{max,Fe^{3+}}}$	$370\,\mathrm{mg\,g^{-1}}$
Particle density	ρ_p	$1\,170\,\mathrm{g\,L^{-1}}$ [77]
Bulk density	ρ_b	$720\,\mathrm{g\,L^{-1}}$ [77]
Molecular diffusivities	$D_0^{\mathrm{Fe}^{2+}}$	$7.19 \times 10^{-10}\ \mathrm{cm^2\,s^{-1}}$ [78]
	$D_0^{\mathrm{Fe}^{3+}}$	$6.04 \times 10^{-10}\ \mathrm{cm^2\,s^{-1}}$ [78]
Total particle mass	m_p	8.835 g
Volumetric flow rate	$\dot{V}$	$40\,\mathrm{mL\,min^{-1}}$
Initial pH	pH	3.28

The ion exchange cartridge was modeled as an axial cylinder, with additional process parameters determined in accordance with Section 4.2. In our scope, it is not possible to accurately measure the concentrations of iron ions (Fe^{2+} and Fe^{3+}) and thus the specific ion exchange rates. Since direct measurement of iron ion loading is challenging in continuous systems, we used pH as an indirect proxy for iron ion exchange. Therefore, the change in pH value is utilized for parameter estimation. During the ion exchange process, H^+ ions are released, which influences the pH. However, pH is affected by other species and interactions in the solution. Therefore, while pH serves as an indirect indicator of ion exchange dynamics, it may not exclusively reflect H^+ ion release from the ion exchange material. The experimental data of the change of the pH in a continuous ion exchange process is shown in Figure 4.4. The graph presented begins at the point where iron ions are added to the experiment. This coincides with a period of stable pH following an initial decrease (not shown in Figure 4.4), after the ion exchange material is brought into contact with the water. We have intentionally excluded this initial pH drop from our analysis. This exclusion is based on the assumption that this initial change likely reflects the self-dissociation of the protonated active groups within the ion exchange material upon contact with water, which is not included in our model.
In the first minutes after the addition of the iron ions, a sharp drop in pH can be observed. Subsequently, the pH decreases steadily and levels off toward the end of the experiment.
To achieve a suitable fit for the pH curve, surface diffusivities $D_{s,Fe^{2+}}$ and $D_{\mathrm{s},Fe^{3+}}$ (Equation (C.1)) were estimated. For simplicity, we assumed a priori that the surface diffusivities of Fe^{2+} and Fe^{3+} are equal. This is based on their similar ionic sizes and charges. The value

of these surface diffusivities was then determined by least-squares regression under two conditions: charge neutrality (cn), where two or three H^+ ions are released per adsorbed Fe^{2+} and Fe^{3+} ion, respectively, and the condition (c2), where two H^+ ions are released per adsorbed iron ion. For the charge neutrality condition (cn), the surface diffusivities were estimated to be $D_{s,Fe^{2+}} = D_{s,Fe^{3+}} = 0.15 \cdot 10^{-15} \mathrm{cm}^2\,\mathrm{s}^{-1}$. For the two H^+ ions release condition (c2), the estimated value was found to be $D_{s,Fe^{2+}} = D_{s,Fe^{3+}} = 0.3 \cdot 10^{-15} \mathrm{cm}^2\,\mathrm{s}^{-1}$. However, the estimated diffusivities fall outside the range reported for anion exchange material surface diffusivities in the literature [79]. This discrepancy suggests that the fitted parameter may be compensating for unmodeled factors such as channeling, dead zones, or uneven flow distribution. These low fitted values arise in part due to model assumptions: the surface diffusivity used here is an effective parameter that lumps together several transport resistances, including intraparticle diffusion, film diffusion, and any nonidealities in flow or particle packing. The model assumes homogeneous porosity and does not explicitly resolve spatial distributions of voidage or channeling effects. As such, the fitted diffusivity compensates for these unmodeled factors by appearing lower than literature values for idealized systems.

In addition, the observed deviation from typical diffusivity ranges may also reflect characteristics of anomalous diffusion, as commonly reported in packed beds and porous media [80, 81]. In such systems, effective transport is reduced due to pore structure effects such as tortuosity, dead-end pores, and constricted channels, which lead to sub-Fickian behavior. These effects are not captured explicitly in the present model but are known to significantly reduce apparent diffusivity even when molecular transport remains unchanged. Moreover, the breakthrough curve shape was found to be sensitive to the value of D_s, particularly influencing the steepness of the front and the timing of iron ion breakthrough. This sensitivity supports the relevance of the chosen fitted value and highlights the importance of D_s in accurately capturing the system dynamics.

The fitting in Figure 4.4 indicates that the case cn agrees better with the experimental data. Consequently, the cn case is used as a base case for the subsequent simulations.

It should be noted that while pH provides a sensitive and time-resolved indicator of overall ion exchange dynamics, it does not allow for species-specific resolution of Fe^{2+} and Fe^{3+} adsorption. Direct measurements of individual iron ion concentrations would provide a more accurate basis for model validation in the future.

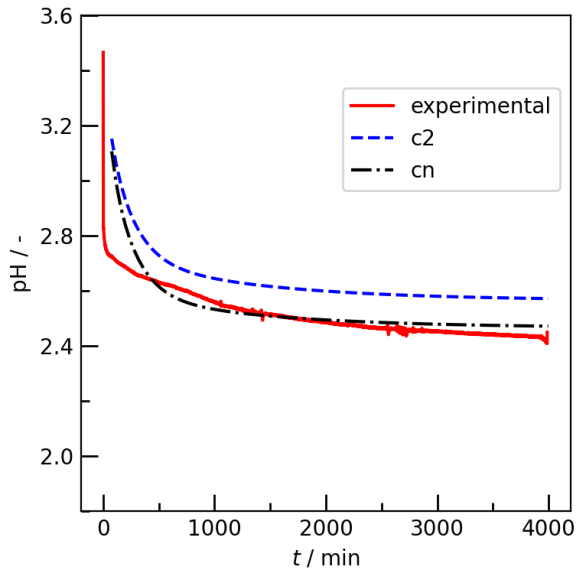

Figure 4.4.: Comparison of measured and simulated pH values in a continuous ion exchange process. The pH measurements were taken at very short intervals, allowing for a near-continuous representation of the data. The simulated pH curves are fitted assuming two scenarios: release of two compensating ions per iron ion (c2) and charge neutrality (cn), where release of three ions per Fe^{3+} ion is assumed. The cn scenario shows a better fit with the experimental data.

4.4. Sensitivity Analysis and Long-Term Performance

In this section, we first use the model developed in the previous sections to predict breakthrough curves at constant inlet concentrations and analyze the effect of the exponent n_{BC} for the exchange factor K_{BC} and various gradients within the ion exchanger. This is followed by a sensitivity analysis to investigate how different factors—such as the refinement volumetric flow rate, initial concentrations of Fe^{2+} and Fe^{3+}, and corrosion rate—affect the breakthrough curves. Finally, we examine the long-term adsorption behavior to estimate the time until exhaustion of the ion exchange bed and determine the appropriate intervals for its replacement.

The current model implementation and parameterization are specifically tailored to the experimental data obtained for Lewatit TP 207® under conditions of pH = 4 and T = 60 °C. These operating parameters were selected based on typical conditions in PEM electrolyzer systems and matched to the available laboratory setup. As such, the fitted adsorption parameters (e.g., Langmuir constants, surface diffusivity) are valid only within this operating window. Adsorption capacity and ion exchange kinetics are known to be sensitive to both pH and temperature, due to effects on ionization equilibria and surface interactions. Therefore, the model's predictive accuracy outside of these conditions has not been validated and requires further experimental study. In particular, generalization to other exchanger resins or strongly acidic/alkaline conditions may require re-fitting of equilibrium and transport parameters.

4.4.1. Simulation of Breakthrough Curves

In this subsection, the primary objective is to verify whether our modified Thomas model can capture the competitive adsorption of Fe^{2+} and Fe^{3+} and in particular the replacement effect described in Section 4.2.2.2. To that end, we analyze the impact of varying the parameter $n_{BC,0}$ in Eq. (4.10) on the shape of the weak ion displacement curve using simulations of the ion exchanger with a fixed iron ion concentration input, i.e., excluding the model for the iron ion source in electrolyzers. The most suitable value of $n_{BC,0}$ is then used for simulations including the model for the iron ion source in electrolyzers. Table 4.6 includes the parameters used for the simulation of the breakthrough curves.

Table 4.6.: Parameters utilized in the simulation of breakthrough curves for the ion exchange process.

Parameter	Symbol	Value
Temperature	T	333.15 K
pH	pH	4
Number of ion exchange particles	n_p	10^9 (63 kg)
Ion exchanger height	h	1 m
Sections	N	5
Inlet iron concentration	$c_{in,Fe^{2+}}$	$50\,mg\,L^{-1}$
	$c_{in,Fe^{3+}}$	$50\,mg\,L^{-1}$
Volumetric flow rate	$\dot{V}$	$25\,BV\,h^{-1}$ ($104\,L\,min^{-1}$)
Langmuir constants	$K_L^{Fe^{2+}}$	$0.034\,L\,mg^{-1}$
	$K_L^{Fe^{3+}}$	$0.048\,L\,mg^{-1}$
Initial capacity	$q_{Fe^{2+},0}$	$0\,mg\,g^{-1}$
	$q_{Fe^{3+},0}$	$0\,mg\,g^{-1}$

In Figure 4.5, we examine the impact of the parameter $n_{BC,\,0}$ in the range [0, 2]. We simulate the breakthrough ratio for different values of $n_{BC,\,0}$. When $n_{BC,0} = 0$, which represents the case without our modification (where $K_{BC} = 1$, as in Equation (4.7)), there is no significant peak in the ratio of outlet to inlet concentrations for the weak species (Fe^{2+}). In contrast, a pronounced peak in the ratio for Fe^{2+} is observed at $n_{BC,0} = 2$, where the ratio exceeds 1. This indicates that more Fe^{2+} ions are exiting the ion exchanger than entering. This behavior occurs because, initially, Fe^{2+} accumulates in the downstream sections. Over time, as the sections near the inlet become depleted of adsorbed Fe^{3+}, the preferential adsorption of Fe^{3+}, driven by its higher Langmuir constant and greater maximum adsorption capacity, at the downstream sections displaces the accumulated Fe^{2+}. This displacement leads to a peak release of Fe^{2+} as it exits the ion exchanger.
These simulations aim to capture the qualitative behavior observed in the system. We do not currently have quantitative data to validate or fit the model, and the purpose

of this analysis is to explore and understand the mechanisms driving this phenomenon. Qualitatively, we observe that the peak length and height increase with increasing $n_{\mathrm{BC},0}$, leading to improved agreement with the shape of the multi-species breakthrough curves observed in the work of Hu et al. [66], and these curves become more similar at higher $n_{\mathrm{BC},0}$. Therefore, for the following simulations, $n_{\mathrm{BC},0} = 2$ is chosen.

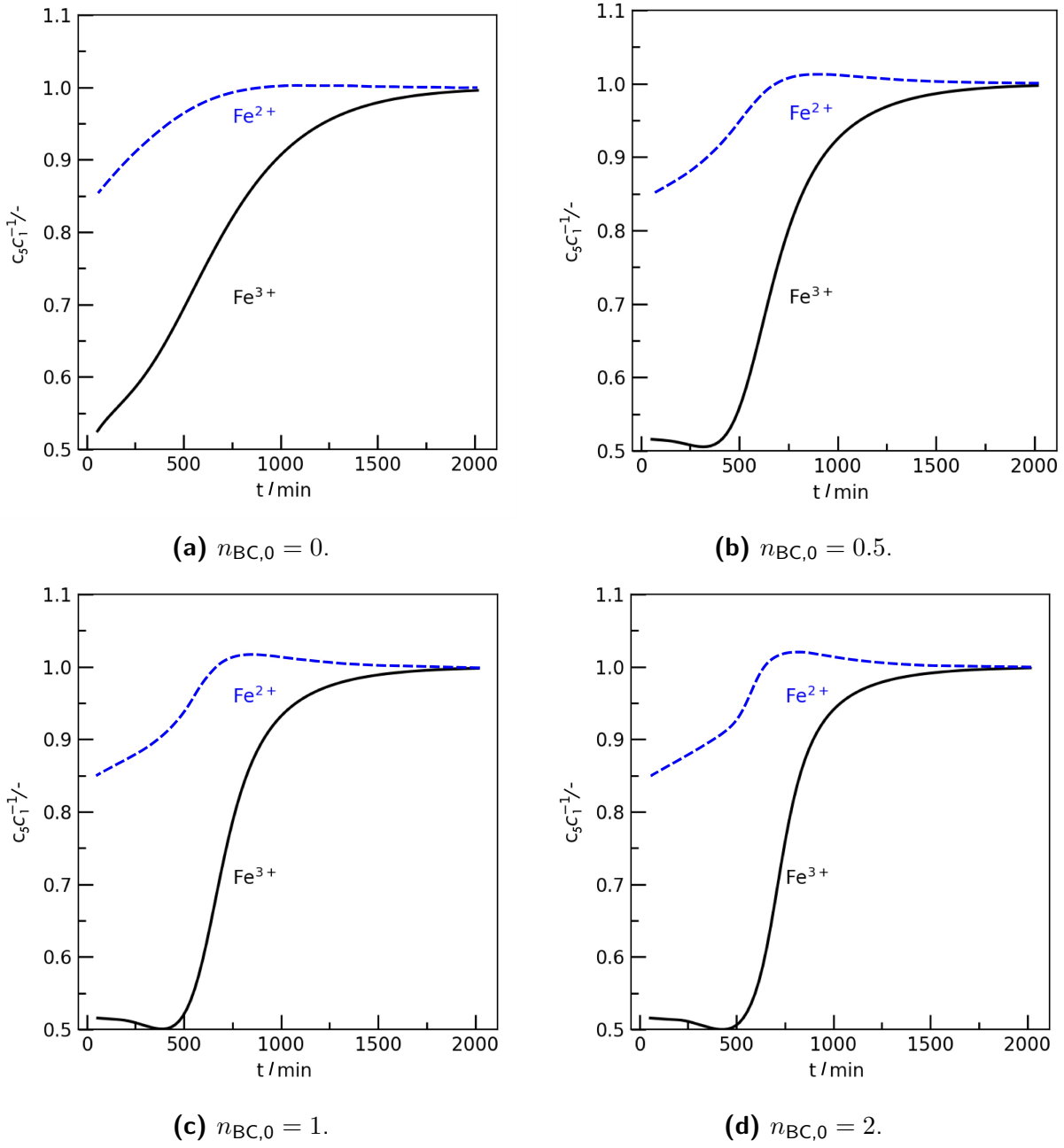

(a) $n_{\mathrm{BC},0} = 0.$ **(b)** $n_{\mathrm{BC},0} = 0.5.$

(c) $n_{\mathrm{BC},0} = 1.$ **(d)** $n_{\mathrm{BC},0} = 2.$

Figure 4.5.: Influence of the parameter $n_{\mathrm{BC},0}$ on the outlet-to-inlet concentration ratio of Fe^{2+} and Fe^{3+} ions in the ion exchanger. The exponent n_{BC} governs the competitive adsorption behavior and the replacement effect, where weak ions are displaced by strong ions. As $n_{\mathrm{BC},0}$ increases, the Fe^{2+} concentration at the outlet temporarily exceeds the inlet concentration, indicating a competitive adsorption-replacement mechanism. This transient peak occurs as Fe^{3+} ions, which have a stronger affinity, displace Fe^{2+} ions from the exchanger, causing a short-term increase in Fe^{2+} concentration before it declines.

4.4.2. Sensitivity Analysis for Ion Removal in the Electrolyzer System

In this and the following sections, the model for the iron ion source in electrolyzers is combined with the ion exchanger model. The standard parameters for the system are defined in Table 4.7. First, we conduct a sensitivity analysis of the ion exchange process, examining the effects of various parameters, such as the volumetric flow rate, corrosion rate, initial concentration and initial capacity (to investigate the impact of regenerated ion exchange material). The system is simulated for a 24-hour period, and the total iron concentrations in the electrolyzer are compared. This analysis aims to assess the robustness of the ion exchange process under different conditions and understand the critical parameters that significantly influence the system's performance.
There are no available measurement data for the influence of pH and temperature on the maximum capacity of the ion exchange material used in this study. Consequently, sensitivity studies for these variables could not be performed. However, both pH and temperature generally have an impact on ion exchange processes. High pH typically facilitates ion removal due to decreased repulsion of H^+ ions from the adsorbent sites. Similarly, temperature can affect the kinetics of ion adsorption and desorption, potentially altering the equilibrium capacities.

Table 4.7.: Standard parameters for the sensitivity analysis.

Parameter	**Symbol**	**Value**
Temperature	T	298.15 K
pH	pH	4
Corrosion rate	r_c	$10.36\,\mu m\,yr^{-1}$
Electrolysis system water volume	$V_{L,E}$	10,000 L
Number of ion exchange particles	n_p	10^9 (63 kg)
Sections	N	5
Initial iron concentration (Fe^{2+} and Fe^{3+})	$c_{Fe,0}$	$10^{-3}\,mg\,L^{-1}$
Volumetric flow rate	$\dot{V}$	$25\,BV\,h^{-1}$ (approx. $104\,L\,min^{-1}$)
Langmuir constants	$K_L^{Fe^{2+}}$	$0.034\,L\,mg^{-1}$
	$K_L^{Fe^{3+}}$	$0.048\,L\,mg^{-1}$
Initial capacity	$q_{Fe^{2+},0}$	$0\,L\,mg^{-1}$
	$q_{Fe^{3+},0}$	$0\,L\,mg^{-1}$

4.4.2.1. Effect of Volumetric Flow Rate on Ion Exchange

The influence of the volumetric flow rate on the ion exchange process was investigated within the range of 10 to $40\,BV\,h^{-1}$, with a step size of $10\,BV\,h^{-1}$ (Figure 4.6). The initial concentration of iron ions in the electrolyzer is low, and over time the Fe^{2+} and Fe^{3+} concentration increases until both slow down. However, the Fe^{3+} concentration stays

significantly lower. Since the rate of formation of Fe^{3+} is kinetically controlled by the concentration of Fe^{2+} as well as the rate constant of its oxidation, which is low, the Fe^{3+} concentration remains low. In contrast, for Fe^{2+}, the corrosion rate is high compared with the oxidation rate of Fe^{2+} to Fe^{3+}. In the considered range of volumetric flow rate, a higher flow rate results in a shorter residence time, so that the ions spend less time in all sections of the ion exchanger. This results in a decrease in the uptake of ions from the mobile phase per pass through the ion exchanger, and thus an increase in the ion concentrations in the system.

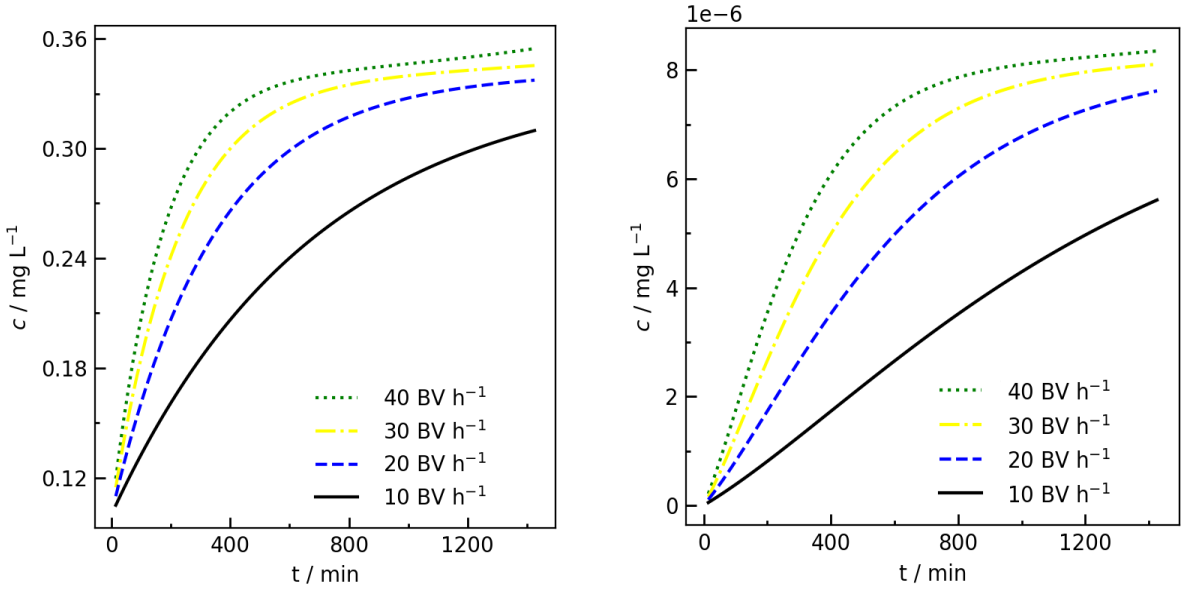

(a) Effect of volumetric flow rate on Fe^{2+} concentrations in the electrolyzer. The Fe^{2+} concentration increases over time until reaching a limit, with higher flow rates generally resulting in higher Fe^{2+} levels.

(b) Effect of volumetric flow rate on Fe^{3+} concentration in the electrolyzer. The Fe^{3+} concentration increases over time until leveling off, with higher flow rates generally resulting in higher Fe^{3+} levels.

Figure 4.6.: Fe^{2+} and Fe^{3+} concentrations in the electrolyzer for varying volumetric flow rate. All other model parameters were held constant according to Table 4.5. The figure illustrates the influence of corrosion rate on ion breakthrough timing and concentration levels.

4.4.2.2. Impact of the Initial Iron Concentration

The effect of the initial concentrations of Fe^{2+} and Fe^{3+} in the electrolyzer on the ion exchange process was examined within a range of 10^{-3} mg L^{-1} to 1 mg L^{-1}. Higher initial concentrations of Fe^{2+} led to a greater degree of oxidation to Fe^{3+}. Since the equilibrium state depends on concentration, increased ion concentrations resulted in increased equilibrium capacities and enhanced ion removal. As shown in Figure 4.7, the iron ion concentration decreases over time for high initial concentrations of Fe^{2+} and all initial concentrations of Fe^{3+}, and increases for low initial concentrations of Fe^{2+}. Due to the initial high uptake of iron ions, the capacity is higher for higher initial ion concentrations, which subsequently accelerates the desorption process.

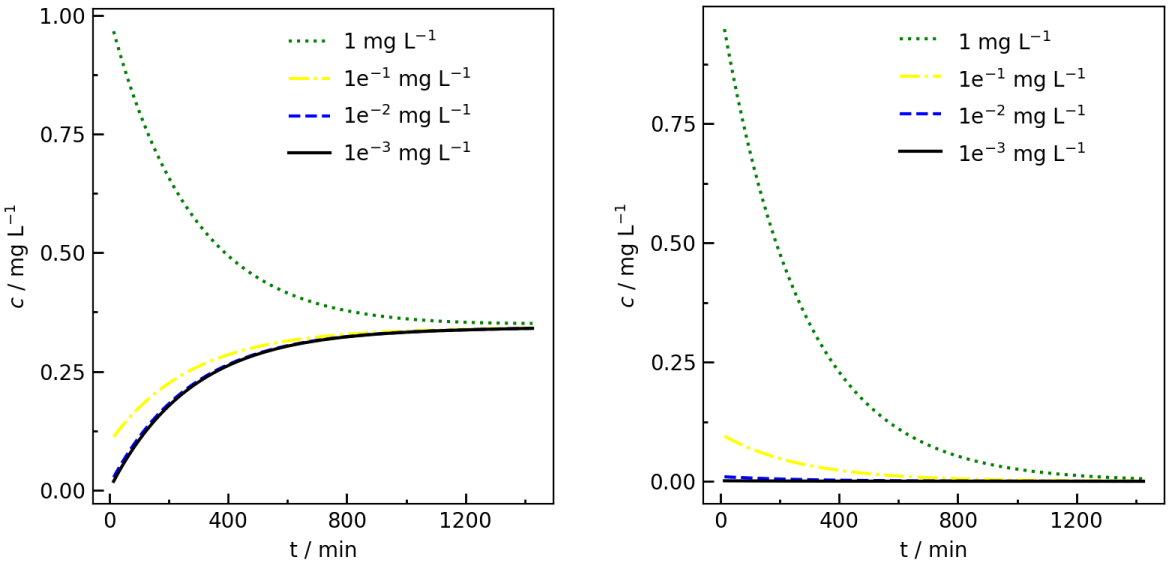

(a) Effect of the initial Fe^{2+} concentration on the time-dependent concentration in the electrolyzer. The concentration of Fe^{2+} initially increases for low initial concentrations due to corrosion, as the ion exchange process is not sufficiently efficient to remove Fe^{2+} ions from the solution. This leads to a continuous addition of Fe^{2+} ions until the system reaches equilibrium, where the rate of ion addition by corrosion balances the rate of removal by the ion exchanger. Conversely, at higher initial Fe^{2+} concentrations, the ion exchange process becomes more effective, resulting in a gradual decrease in Fe^{2+} as it is converted to Fe^{3+}.

(b) Effect of the initial Fe^{3+} concentration on the time-dependent concentration in the electrolyzer. Regardless of the initial concentration, Fe^{3+} levels decrease over time, highlighting the removal efficiency of the ion exchange process. Higher initial concentrations lead to a steeper decline in Fe^{3+} concentration.

Figure 4.7.: Fe^{2+} and Fe^{3+} concentrations in the electrolyzer for varying initial iron concentrations. All other model parameters were held constant according to Table 4.5. The figure illustrates the influence of corrosion rate on ion breakthrough timing and concentration levels.

4.4.2.3. Impact of Corrosion Rate

The corrosion rate was varied within the range of 2 to 10 $\mu m\,yr^{-1}$ [62], corresponding to different materials and fabrication processes used in stainless steel components for balance of plant systems in electrolyzers, including both non-welded and gas tungsten arc welded joints. As discussed in Section 4.2.1, this changes the Fe^{2+} production rate while maintaining a constant oxidation rate constant for the conversion of Fe^{2+} to Fe^{3+} according to Benson et al. [63]. A higher corrosion rate leads to a higher Fe^{2+} concentration, while having little effect on the Fe^{3+} concentration, as shown in Figure 4.8. This occurs because the corrosion rate primarily affects the Fe^{2+} concentration, and at low Fe^{2+} concentrations, the ion exchange process is less efficient at removing Fe^{2+}. Consequently, Fe^{2+} accumulates until the system reaches equilibrium, where the rate of Fe^{2+} addition by corrosion balances its removal by ion exchange. The ion exchanger efficiently removes Fe^{3+}, ensuring that its concentration remains relatively stable despite variations in Fe^{2+} levels.

As shown in Figure 4.8b, the Fe^{3+} concentration remains stable across different corrosion rates, highlighting the effectiveness of the ion exchanger.
Although no formal sensitivity ranking was conducted, the results of the parametric simulations in this section provide qualitative insights into the influence of individual parameters. These trends can inform operational priorities; for instance, the corrosion rate appears to have a stronger impact on Fe^{2+} accumulation than the initial concentrations under typical PEM conditions.

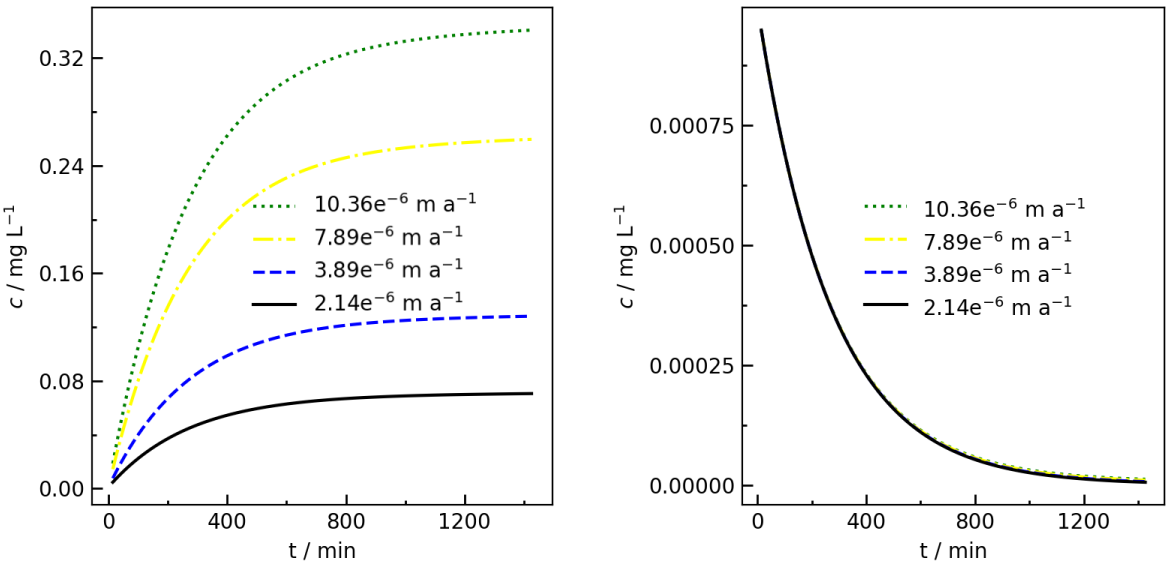

(a) The effect of corrosion rate on the Fe^{2+} concentration in the electrolyzer. As the corrosion rate increases from 2 to 10 $\mu m\,yr^{-1}$, the concentration of Fe^{2+} also increases. This is due to the higher production rate of Fe^{2+} from the enhanced dissolution of iron at higher corrosion rates, as discussed in Section 4.2.1. The graph indicates a direct relationship between the corrosion rate and the Fe^{2+} concentration in the system.

(b) The effect of corrosion rate on the Fe^{3+} concentration in the electrolyzer. Unlike Fe^{2+}, the Fe^{3+} concentration remains relatively stable across different corrosion rates. This stability is due to the ion exchanger's efficient removal of Fe^{3+}, which offsets its formation from Fe^{2+}. Consequently, even as higher corrosion rates increase the production of Fe^{2+}, the Fe^{3+} concentration does not significantly rise because the ion exchanger effectively removes the newly formed Fe^{3+}. Without the ion exchanger, higher Fe^{2+} levels would lead to proportionally higher Fe^{3+} concentrations, as the formation rate of Fe^{3+} is dependent on the Fe^{2+} concentration.

Figure 4.8.: Fe^{2+} and Fe^{3+} concentrations in the electrolyzer for varying corrosion rate. All other model parameters were held constant according to Table 4.5. The figure illustrates the influence of corrosion rate on ion breakthrough timing and concentration levels.

4.4.3. Simulation of Long-Term Ion Exchange

The long-term ion exchange is simulated to investigate the ion removal over the service-time of the ion exchanger. The key parameters used in the simulation are summarized in

Table 4.8.

Table 4.8.: Parameters for the long-term ion exchange simulation.

Parameter	**Symbol**	**Value**
Temperature	T	$298.15\,\mathrm{K}$
pH	pH	4
Corrosion rate	r_c	$10.36\,\mu\mathrm{m\,yr^{-1}}$
Electrolyzer water volume	$V_{\mathrm{L,\,E}}$	$10000\,\mathrm{L}$
Ion exchange particles	m_p	$10^{\,9}$ (approx. $191\,\mathrm{kg}$)
Sections	N	5
Initial iron concentration (Fe^{2+} and Fe^{3+})	$c_{\mathrm{Fe},0}$	$0.01\,\mathrm{mg\,L^{-1}}$
Volumetric flow rate	$\dot{V}$	$25\,\mathrm{BV\,h^{-1}}$ (approx. $104\,\mathrm{L\,min^{-1}}$)
Langmuir constants	$K_\mathrm{L}^{\mathrm{Fe^{2+}}}$	$0.034\,\mathrm{L\,mg^{-1}}$
	$K_\mathrm{L}^{\mathrm{Fe^{3+}}}$	$0.048\,\mathrm{L\,mg^{-1}}$
Initial capacity	$q_{\mathrm{Fe^{2+},0}}$	$0\,\mathrm{mg\,g^{-1}}$
	$q_{\mathrm{Fe^{3+},0}}$	$0\,\mathrm{mg\,g^{-1}}$

The iron concentrations in the electrolyzer and in the ion exchanger sections are plotted in Figure 4.9. Initially, the total iron concentration increases from 0.01 $\mathrm{mg\,L^{-1}}$ to 0.1 $\mathrm{mg\,L^{-1}}$ over approximately 7500 hours. This slow increase is due to the limited capacity of the ion exchange bed. This concentration threshold of $0.1\,\mathrm{mg\,L^{-1}}$ can be interpreted as a conservative guideline for cartridge replacement in applications where strict limits on iron concentration are required, such as ultrapure water systems.
As time progresses, the equilibrium capacity is approached, reducing the ion uptake rate. Most of the dissolved iron is Fe^{2+}, released due to corrosion. The oxidation of Fe^{2+} to Fe^{3+} is minimal due to the low oxidation rate. Around 9166 hours, the ion exchange bed becomes nearly exhausted, leading to a sharp increase in the total iron concentration.

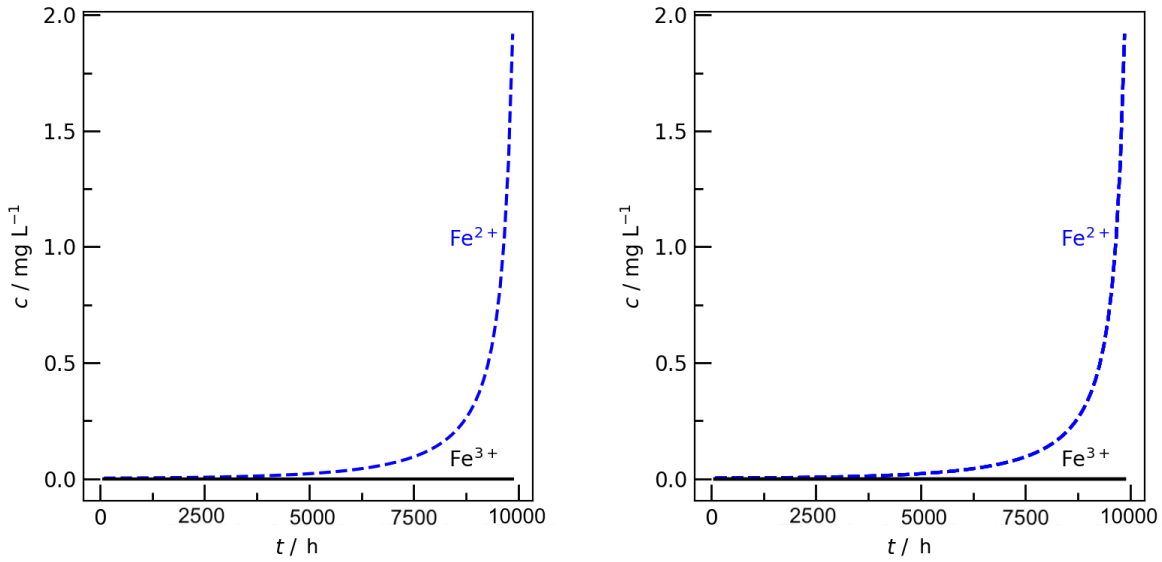

(a) Time evolution of iron concentrations in the electrolyzer during the long-term ion exchange simulation.

(b) Time evolution of iron concentrations at the ion exchanger exit during the long-term simulation.

Figure 4.9.: Long-term simulation results showing the iron concentration profiles in the electrolyzer (a) and at the ion exchanger exit (b). Initially, the iron concentration increases slowly due to the limited capacity of the ion exchange bed, reaching a peak before the bed becomes nearly exhausted, leading to a sharp rise in concentration.

The capacity of the ion exchange bed for iron ions $q_{\mathrm{Fe^{2+}}}$ reaches its maximum value around 9166 hours. At this time, $q_{\mathrm{Fe^{2+}}} \approx q_{\mathrm{max,Fe^{2+}}}$, where q_{max} is the maximum capacity. Figure 4.10 illustrates the observed capacities within the bed sections. These capacities for $\mathrm{Fe^{2+}}$ first increase slowly, then rise more quickly once the respective section is nearly exhausted. Additionally, the capacity for $\mathrm{Fe^{3+}}$ remains negligible. This is due to two factors: (1) the presence of $\mathrm{Fe^{2+}}$ reduces the uptake of $\mathrm{Fe^{3+}}$, and (2) the formation rate of $\mathrm{Fe^{3+}}$ is too low for it to accumulate significantly in the system.

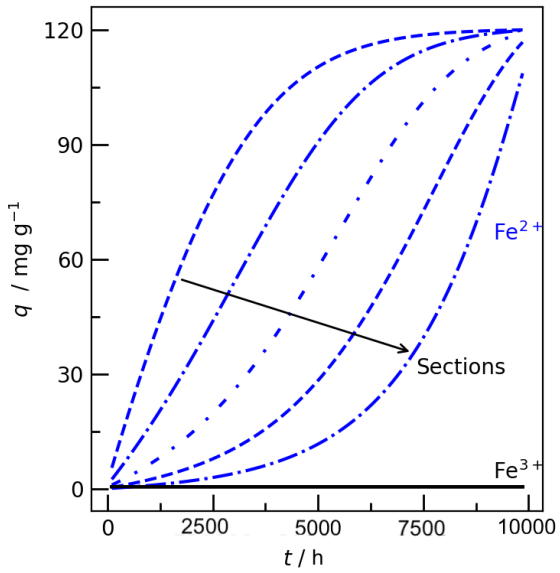

Figure 4.10.: Long-term simulation results showing the observed ion exchange capacities for Fe^{2+} and Fe^{3+} within the bed sections. The bed's Fe^{2+} capacity reaches its maximum around 9166 hours. The Fe^{3+} capacity remains negligible due to the strong preference for Fe^{2+} and the low formation rate of Fe^{3+}.

4.5. Conclusion & Outlook

In conclusion, we proposed a model for ion exchange rates in multi-species systems, specifically designed for continuous electrolysis processes with an integrated ion exchanger. A Fe^{2+}/Fe^{3+} ion exchange model was developed based on the Thomas model and adapted for multi-species systems with competitive adsorption. The model was fitted to pH measurements from laboratory-scale ion exchange experiments to estimate surface diffusivities, achieving good agreement between simulated and experimental results. The model was then utilized to predict breakthrough curves in continuous ion exchange systems, conduct sensitivity analyses, and estimate the long-term performance of the ion exchanger.
The predicted breakthrough curves show the characteristic peak in Fe^{2+} concentration over time, consistent with trends in ion exchange modeling, where competitive adsorption causes early breakthrough and overshoot for weaker-binding species [67]. This behavior aligns with the expected dynamics of multi-ion systems governed by differing Langmuir affinities, supporting the model's validity for continuous electrochemical systems, despite the limited availability of comparable experimental data in PEM contexts.
The results quantify that a higher volumetric flow rate leads to a higher concentration of ions, while the initial concentration has minimal impact on equilibrium due to the high kinetic driving force that increases the uptake rate. This suggests that ion exchange is a self-regulating process. Conversely, corrosion rates are the primary factor influencing equilibrium, with higher corrosion rates significantly increasing the concentration of ions in the system.
Long-term use of the ion exchanger results in a slow increase in ion concentration during the early part of the operational life. For the considered case study, the total iron concentration remains below $0.1\,\mathrm{mg\,L^{-1}}$ for up to 7500 hours under given conditions. This

concentration is highly dependent on process parameters and can be reduced by optimizing pH, temperature and refining flow rate. At approximately 10000 hours, the ion exchange bed is nearly exhausted and the ion concentration begins to increase rapidly. Based on the simulation results, a total iron concentration of $0.1\,\mathrm{mg\,L^{-1}}$ may serve as a practical upper limit for cartridge replacement in applications with strict water quality requirements. This threshold is maintained for up to 7500 hours under nominal conditions. Since cartridge exhaustion occurs between 7500–10000 hours, depending on operating parameters, the model supports system-specific maintenance planning.

The sensitivity analysis revealed that flow rate and corrosion rate significantly influence iron ion breakthrough behavior. These findings have practical implications: higher flow rates improve throughput but may reduce cartridge lifetime, while increased corrosion accelerates ion accumulation, potentially shortening maintenance intervals. Optimizing these operational parameters, alongside continuous monitoring, can help extend cartridge service life and improve system reliability. As such, the model can inform the design and sizing of ion exchange cartridges and aid in planning regeneration or replacement strategies. While this study focused on qualitative agreement with experimental pH curves, uncertainty quantification, such as confidence intervals for fitted parameters, was not included due to the limited availability of independent validation data.

The sensitivity to corrosion and flow conditions highlights the need for adaptive scheduling strategies. Instead of fixed intervals, replacement timing should be based on real-time monitoring of system behavior to ensure optimal performance and durability in PEM electrolyzer systems.

While the present study uses pH as an indirect proxy for iron ion exchange, future work could explore alternative indicators such as UV-Vis spectroscopy or other in-situ analytical techniques to achieve more direct validation. For example, it could incorporate direct measurements of Fe^{2+} and Fe^{3+} concentrations (e.g., via AAS or ICP-OES) to improve species-specific validation of the model and reduce reliance on pH as an indirect proxy.

Another limitation is the absence of real breakthrough curve data; although the model predicts breakthrough dynamics well, these have not yet been experimentally validated. This remains a priority for future research.

For future work, the model could be further validated and refined by incorporating equilibrium data at different pH and temperature values. The model was calibrated specifically for Lewatit TP 207® at pH = 4 and $T = 60\,^{\circ}\mathrm{C}$. Since adsorption behavior varies with pH and temperature, further validation and reparameterization are needed to extend the model to other operating conditions or exchanger materials. An identifiability analysis of the Langmuir parameters may also improve robustness. Furthermore, the current model assumes constant corrosion and oxidation rates, which may vary under different operational conditions. Investigating their variability and impact on iron ion concentrations is essential to better capture real-world dynamics.

Additionally, the model does not account for potential changes in flow patterns or channeling effects within the ion exchanger, which could influence performance. Furthermore, the fitted surface diffusivity values likely reflect unmodeled resistances and non-Fickian transport effects, and future work should examine the impact of intraparticle structure and anomalous diffusion on model calibration. Incorporating such factors would enhance predictive accuracy.

A formal quantitative sensitivity analysis is proposed to systematically rank parameter influence and support robust model-based design. This will be a priority in future work,

particularly as more comprehensive datasets become available.
Ultimately, the presented model provides a valuable tool for the design and optimization of ion exchange systems in PEM electrolyzers. By improving long-term performance and enabling predictive maintenance, it supports the broader adoption of hydrogen as a clean energy carrier.
Having addressed degradation mechanisms, gas crossover, and impurity mitigation, the following chapter summarizes the key findings of this thesis and outlines their implications for PEM electrolyzer operation and durability.

5. Conclusion and Outlook

5.1. Conclusion

This dissertation investigates chemical membrane degradation in PEM electrolyzers by first describing the underlying radical-driven degradation mechanism, building on established kinetic models, and analyzing its dependence on operating conditions. Two key contributors to this mechanism are then examined in detail: gas crossover, which governs the availability of oxidizing species such as oxygen and hydrogen peroxide, and iron ions, which catalyze radical formation through the Fenton reaction. While hydrogen and oxygen crossover are analyzed as undesired transport phenomena that influence degradation-relevant species concentrations, ion exchange is investigated as a system-level mitigation strategy to reduce iron contamination and thereby limit catalytic degradation pathways. Through a combination of mechanistic modeling and experimental studies, the work establishes a mechanistic understanding of how species transport, radical-driven chemistry, and metal-ion contamination each influence membrane degradation in PEM electrolyzers under relevant operating conditions. While each aspect is examined individually, the combined results clarify how interacting transport and impurity-related processes shape degradation-relevant reaction pathways in PEM electrolyzer membranes.

For chemical membrane degradation, a dynamic lumped model was developed by integrating the hydroxyl-radical reaction network of Frühwirt et al. [28], the hydrogen-peroxide formation mechanism of Chandesris et al. [11], and a semi-empirical oxygen crossover formulation. The model reproduces experimentally reported fluoride release rates (FRR), predicts a characteristic maximum in degradation at intermediate current densities, and yields long-term PFSA consumption times of approximately 12000–25000 h depending on the operating conditions. Its lumped formulation, however, cannot resolve spatial gradients or localized degradation phenomena such as pinhole initiation, and it relies on externally estimated iron fluxes that are not directly measurable.

The experimental evaluation of hydrogen and oxygen crossover addressed a data gap at elevated pressures. Hydrogen crossover was accurately described by existing supersaturation-based diffusion models after parameter fitting, while oxygen crossover exhibited a nonlinear dependence on current density that existing models could not reproduce. A modified oxygen crossover model incorporating current-dependent supersaturation and electro-osmotic water drag was therefore introduced and validated for pressures of 1.15 bar and 8.5 bar. Limitations remain due to the fixed operating temperature of 60 °C and the restricted pressure window, and water crossover, while simulated, was not experimentally verified.

A spatially resolved multi-species ion exchange model was developed to describe the competitive adsorption of Fe^{2+} and Fe^{3+} ions in electrolyzer process water. The model extends multi-species Langmuir theory by incorporating the replacement of Fe^{2+} by Fe^{3+}, consistent with observations from new equilibrium and breakthrough experiments using Lewatit TP 207®. Limitations include the use of pH as an indirect proxy for species con-

centrations, the absence of real breakthrough curve data, calibration restricted to a single pH and temperature, assumptions of constant corrosion and oxidation rates, and simplified treatment of flow nonuniformities and intraparticle transport. These constraints define the present model's range of validity and motivate further developments.
Taken together, these results highlight the interrelated roles of gas crossover, radical chemistry, and iron contamination in shaping degradation-relevant conditions in PEM electrolyzers. The combined consideration provides important context for assessing degradation trends, operational constraints, and durability-related behavior under realistic operating conditions. Such mechanistic clarity is essential for the development of reliable diagnostic models and informed durability assessment of PEM electrolyzers.
Overall, this dissertation combines modeling and experimental analyses to examine chemical degradation mechanisms, gas crossover phenomena, and iron impurity mitigation in PEM electrolyzers. The results provide complementary insights into how chemical reactions, species transport, and impurity presence each influence degradation-relevant conditions under realistic operating scenarios.
The results underline the importance of considering these processes jointly when interpreting degradation trends and operational limitations, and they support the use of system-aware modeling approaches when assessing durability-related behavior of PEM electrolyzers in industrial contexts.

5.2. Outlook

Further research is required to advance chemical membrane degradation modeling for PEM electrolyzers. Spatially resolved formulations would allow the investigation of concentration gradients of radicals, hydrogen peroxide, and iron species within the membrane and catalyst layers, and could provide insight into heterogeneous degradation phenomena such as localized radical accumulation, pinhole formation, and interactions between chemical and mechanical degradation. The mechanistic analysis presented in this dissertation helps identify the dominant reaction pathways and transport processes under electrolyzer operating conditions and may inform the targeted development of such spatially resolved models in future work.
Future studies should expand the experimental validation of oxygen and water crossover across a wider range of temperatures, pressures, and dynamic load scenarios. Measurements beyond 8.5 bar, under transient operation, or using membranes with modified water transport characteristics would improve the generalizability of the proposed crossover model. Incorporating two-phase transport or recombination kinetics may further enhance predictive fidelity, particularly for high-pressure or high-current-density operation.
The ion exchange model may be extended to incorporate pH-dependent adsorption behavior, long-term resin aging, fouling effects, and multi-bed regeneration strategies. Coupling the model to more detailed representations of electrolyzer water chemistry, including dynamic corrosion and oxidation behavior, would lead to more realistic predictions of impurity evolution over long-term operation. Further refinement of intraparticle diffusion modeling and detailed characterization of flow distribution, including channeling effects, would strengthen predictive capability. Improved experimental validation—particularly through the acquisition of real breakthrough curves and data across multiple pH and temperature levels—would further support model generalization.

A further step beyond the scope of this dissertation would be a closer numerical coupling of the degradation, crossover, and ion exchange models. Such a coupling would require consistent interfaces between the individual models, as well as numerical strategies capable of handling their different spatial resolutions and characteristic time scales, ranging from fast transport and reaction processes to long-term degradation and impurity accumulation. Establishing this type of coupled framework would enable the systematic analysis of feedback effects between gas crossover, water chemistry, and impurity removal, which are treated separately in the present work, and would support more comprehensive system-level studies of degradation-relevant operating conditions.
Beyond model development, the presented models could be used for condition monitoring of operating electrolyzers. By linking measurable quantities such as fluoride release, gas crossover, or water-quality indicators to the underlying degradation state, the models could support online estimation of membrane health and remaining useful life, thereby enabling predictive maintenance and condition-based operating strategies.
In summary, the results and models presented in this dissertation contribute to the advancement of durable, efficient, and maintainable PEM electrolyzer systems. Continued experimental validation, model refinement, and integration into unified simulation tools will support the deployment of reliable green hydrogen technologies at industrial scale.

Appendix

A. Chemical Degradation Mechanisms in PEM Electrolyzers

Table 1.: Kinetic data overview. Reproduced from Frühwirt et al. [28] with permission from the Royal Society of Chemistry. For each reaction (R1–R23), rate constant k at 25°C (= 298.15 K) in $\mathrm{L\,mol^{-1}\,s^{-1}}$, activation energy E_a in $\mathrm{kJ\,mol^{-1}}$ and pre-exponential factor A in $\mathrm{L\,mol^{-1}\,s^{-1}}$ are given.

Reaction			k (T=298.15 K) [$\mathrm{L\,mol^{-1}\,s^{-1}}$]	E_a[$\mathrm{kJ\,mol^{-1}}$]	A [$\mathrm{L\,mol^{-1}\,s^{-1}}$]
R1	$Fe^{2+} + H_2O_2 + H^+ \rightarrow Fe^{3+} + {}^\bullet OH + H_2O$	$r_1 = k_1[Fe^{2+}][H_2O_2]$	66	35.4[82]	1.05 x 10^8[82]
R2	$Fe^{3+} + H_2O_2 \rightarrow Fe^{2+} + {}^\bullet OOH + H^+$	$r_2 = k_2[Fe^{3+}][H_2O_2]$	8.6 x 10^{-4}	126[83]	8.43 x 10^{18}[83]
R3	$Fe^{2+} + {}^\bullet OH + H^+ \rightarrow Fe^{3+} + -H_2O_2$	$r_3 = k_3[Fe^{2+}][{}^\bullet OH]$	3.6 x 10^8[84] a	9[84]	1.37 x 10^{10}
R4	$Fe^{2+} + {}^\bullet OOH + H^+ \rightarrow Fe^{3+} + H_2O_2$	$r_4 = k_4[Fe^{2+}][{}^\bullet OOH]$	1.2 x 10^6[85]	42[85]	2.74 x 10^{13}
R5	$Fe^{3+} + {}^\bullet OOH \rightarrow Fe^{2+} + H^+ + O_2$	$r_5 = k_5[Fe^{3+}][{}^\bullet OOH]$	8.1 x 10^4[86]	33[87],[86]	4.9 x 10^{10}
R6	$H_2O_2 \rightarrow 2{}^\bullet OH$	$r_6 = k_6[H_2O_2]$	6.5 x 10^{-23} [s^{-1}]	201[88]	10^{13}[s^{-1}][88]
R7	${}^\bullet OH + H_2O_2 \rightarrow {}^\bullet OOH + H_2O$	$r_7 = k_7[{}^\bullet OH][H_2O_2]$	3.0 x 10^7[89] a	14[89]	8.43 x 10^9
R8	${}^\bullet OOH + H_2O_2 \rightarrow {}^\bullet OH + H_2O + O_2$	$r_8 = k_8[{}^\bullet OOH][H_2O_2]$	3.7[90]	33.5[90] b	2.71 x 10^6
R9	$2{}^\bullet OOH \rightarrow H_2O_2 + O_2$	$r_9 = k_9[{}^\bullet OOH]^2$	9.1 x 10^5[91] a	20.6[92]	3.7 x 10^9
R10	$2{}^\bullet OH \rightarrow H_2O_2$	$r_{10} = k_{10}[{}^\bullet OH]^2$	5.3 x 10^9[93] a	8[89]	1.33 x 10^{11}
R11	${}^\bullet OOH + {}^\bullet OH \rightarrow H_2O + O_2$	$r_{11} = k_{11}[{}^\bullet OOH][{}^\bullet OH]$	1.1 x 10^{10}[93] a	14.2[92]	3.39 x 10^{11}
R12	${}^\bullet OH + H_2 \rightarrow H_2O + {}^\bullet H$	$r_{12} = k_{12}[{}^\bullet OH][H_2]$	3.9 x 10^7[93] a	19.2[93]	9.14 x 10^{10}
R13	${}^\bullet H + O_2 \rightarrow {}^\bullet OOH$	$r_{13} = k_{13}[{}^\bullet H][O_2]$	2.2 x 10^{10}[93] a	10.3[92]	1.37 x 10^{12}
R14	$SC\text{-}SO_3H + {}^\bullet OH \rightarrow SC\text{-}O^\bullet + HOCF_2CF_2SO_3H$	$r_{14} = k_{14}[SC\text{-}SO_3H][{}^\bullet OH]$	3.7 x 10^6[94]	70[c]	6.80 x 10^{18}
R15	$SC\text{-}O^\bullet + 3{}^\bullet OH \rightarrow BB\text{-}O^\bullet + 6HF + 3CO_2$	$r_{15} = k_{15}[SC\text{-}O^\bullet][{}^\bullet OH]$	3 x 10^7[31]	70[c]	5.51 x 10^{19}
R16	$BB\text{-}O^\bullet + {}^\bullet OH \rightarrow 2\text{-}(CF_2)_nCOOH + 3HF$	$r_{16} = k_{16}[BB\text{-}O^\bullet][{}^\bullet OH]$	8.5 x 10^7[31]	70[c]	1.56 x 10^{20}
R_{17}-R_{23}	$\text{-}(CF_2)_nCOOH + 2{}^\bullet OH \rightarrow$ $\text{-}(CF_2)_{n-1}COOH + CO_2 + 2HF$	$r_{un} = k_{un}[\text{-}(CF_2)_nCOOH][{}^\bullet OH]$	1.0 x 10^6[95] d	70[c]	1.84 x 10^{18}

[a] Rate constants were recalculated for T = 298.15 K. [b] Activation energy is estimated between 6 and 10 kcal $\mathrm{mol^{-1}}$. [c] Average activation energy found in various degradation experiments.[9] [d] Upper limit for the attack of ${}^\bullet OH$ on CF_3COOH.[95],[96]

Table 2.: Used Parameters in the Model. Where $q_{\mathsf{Fe}^{2+},\mathsf{in}}$ is the fitted parameter value as a result of the parameter estimation.

Parameter	Value
$\alpha_{H_2O_2}$	0.5[11]
γ_c	$150\,\mathrm{m}^2\,\mathrm{m}^{-2}$[11]
λ	22[31]
ρ_{H_2O}	$997\,\mathrm{kg\,m}^{-3}$
ρ_m	$1\,980\,\mathrm{kg\,m}^{-3}$
A	$25\,\mathrm{cm}^2$[11]
$c_{H_2,\mathrm{mem}}$	$0.01\,\mathrm{mol\,L}^{-1}$[18]
$c_{O_2,\mathrm{mem}}$	$0.007\,5\,\mathrm{mol\,L}^{-1}$[18]
c_{SO_3}	$1.81\,\mathrm{mol\,L}^{-1}$[28]
d_{catalyst}	$3 \cdot 10^{-5}\,\mathrm{m}$[97]
d_{membrane}	$1.78 \cdot 10^{-4}\,\mathrm{m}$[11]
EW_0	$1.09\,\mathrm{kg\,mol}^{-1}$[31]
k_0	$7.2 \cdot 10^{-12}\,\mathrm{dm}^7\,\mathrm{mol}^{-2}\,\mathrm{s}^{-1}$[11]
M_{H_2O}	$0.018\,\mathrm{kg\,mol}^{-1}$
n_{drag}	2[30]
R	$8.31\,\mathrm{J\,mol}^{-1}\,\mathrm{K}$
s_{sat}	15[30]
S_{O_2}	$9.8 \cdot 10^{-6}\,\mathrm{mol\,Pa}^{-1}\,\mathrm{m}^{-3}$[30]
$\Delta H_{H_2O_2}$	$42\,450\,\mathrm{J\,mol}^{-1}$[98]
$q_{\mathsf{Fe}^{2+},\mathsf{in}}$	$3 \cdot 10^{-6}\,\mathrm{mol\,dm}^{-2}\,\mathrm{h}^{-1}$

B. Crossover Phenomena in PEM Electrolyzers

Following the formulation of the proposed oxygen crossover model (3.24), we investigated whether and how the mass transfer coefficient $k_{\mathrm{MT,O_2}}$ depends on current density, similar to the dependency observed in Trinke's hydrogen crossover model [18]. Such a dependency could arise from increased local mixing at higher current densities due to more vigorous bubble formation during oxygen evolution.

To evaluate this, we tested three functional assumptions for $k_{\mathrm{MT,O_2}}$: a constant value, a linear form $k_{\mathrm{MT,O_2}} = a_{\mathrm{fitting}}\, J + b_{\mathrm{fitting}}$, and a square-root form $k_{\mathrm{MT,O_2}} = a_{\mathrm{fitting}} \sqrt{J}$, following the approach of Trinke et al. The results of these fits are shown in Figure B.1 for both 1.15 bar and 8.5 bar.

The linear variant provided the best fit across both pressures, suggesting that the mass transfer coefficient may increase with current density. However, the improvement over the other approaches was relatively modest. At 8.5 bar, the linear fit also deviated more strongly from the experimental data than at 1.15 bar, indicating that the model may not fully capture crossover behavior at elevated pressure.

We also attempted to extend the model by including diffusion alongside electro-osmotic drag, but in all cases the optimal fits minimized the contribution of the diffusion term. This suggests that electro-osmotic drag is the dominant transport mechanism under the tested conditions, and that the influence of diffusion is negligible.

It is worth noting that oxygen recombination effects are not explicitly modeled. However, in line with previous studies [12, 30], we assume that these effects are effectively absorbed into the fitted value of $k_{\mathrm{MT,O_2}}$. Recombination is expected to increase with current density, which could contribute to the nonlinear trend in the crossover flux. Nonetheless, the proposed model achieves reasonable agreement with the experimental data even using a constant mass transfer coefficient, suggesting that recombination introduces only weak nonlinearity or is sufficiently captured through empirical fitting.

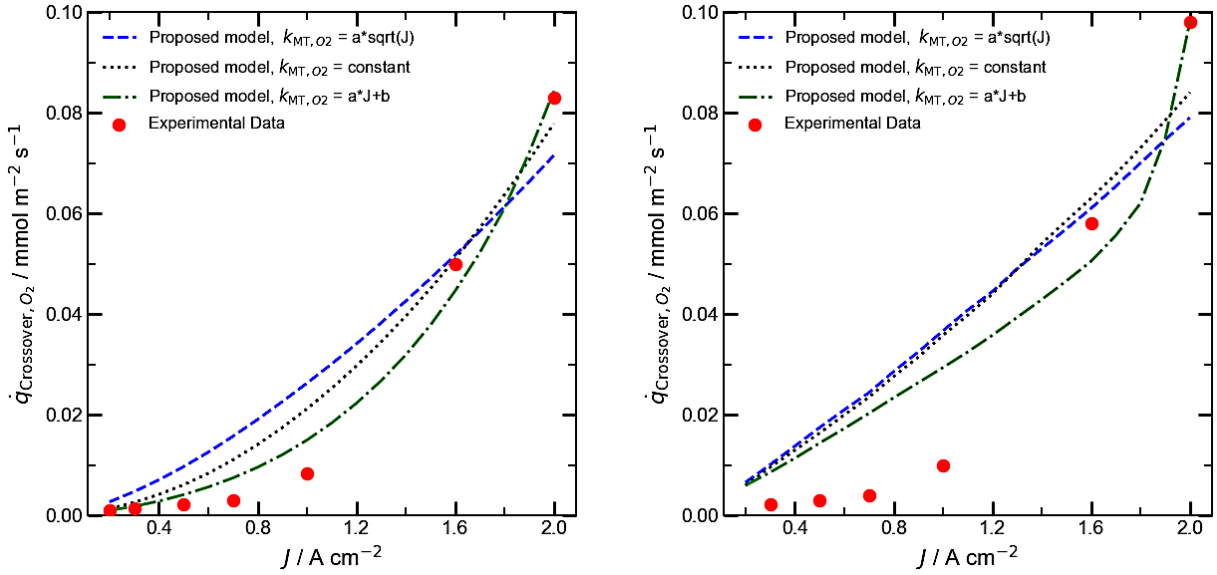

(a) Experimental data at 1.15 bar.

(b) Experimental data at 8.5 bar.

Figure B.1.: Validation of the proposed oxygen crossover model (3.24) using different assumptions for the functional form of the mass transfer coefficient $k_{\mathrm{MT,O_2}}$: constant, linear, and square-root dependencies on current density. The linear form provides the best fit across both pressures. These results support the inclusion of current-dependent supersaturation in the model formulation.

C. Multi-Species Ion Exchange Modeling for Iron Removal

The adsorption rate constant k'_{kin} for liquid adsorption is calculated via [99]

$$\begin{aligned} \frac{1}{k'_{\mathrm{kin}}} &= \frac{K'_{\mathrm{L}}+1}{2K'_{\mathrm{L}}}\left(\frac{\frac{c_i}{q_{\mathrm{max},i}\,\rho_{\mathrm{b}}}}{k_{\mathrm{s}}}+\frac{1}{k_{\mathrm{f}}}\right), \\ K'_{\mathrm{L}} &= 1+K_{\mathrm{L},i}\,c_i, \\ k_{\mathrm{s}} &= \frac{15D_{\mathrm{s}}}{(1-\epsilon_{\mathrm{b}})d_{\mathrm{p}}}, \end{aligned} \tag{C.1}$$

with mass transfer coefficient for the liquid phase k_{f}, surface diffusivity D_{s}, and adsorbent particle diameter d_{p}.
The mass transfer coefficient k_{f} is calculated following [60]:

$$k_{\mathrm{f}} = \frac{D_0}{d_{\mathrm{p}}}(2+1.45\mathrm{Re}_{\mathrm{b}}^{1/2}\mathrm{Sc}^{1/3})$$

with molecular diffusivity D_0, the Reynolds number $\mathrm{Re_b}$ and the Schmidt number Sc. The Reynolds number $\mathrm{Re_b}$ in a packed bed can be calculated as follows [100]:

$$\mathrm{Re}_{\mathrm{b}} = \frac{\rho_{\mathrm{W}}\cdot d_{\mathrm{p}}\cdot v_{\mathrm{super}}}{(1-\epsilon_{\mathrm{b}})\cdot\eta},$$

with liquid density of water ρ_{W}, and the dynamic viscosity η of water. The Schmidt number is defined as [100]:

$$\mathrm{Sc} = \frac{\eta}{\rho_{\mathrm{W}} \cdot D_0}.$$

Bibliography

[1] S. Dörner, M. Kinzl, A. Mitsos, and D. Bongartz. Dynamic lumped cell-level model of chemical membrane degradation in PEM electrolysis: Impact of pressure and time dependence. *Industrial & Engineering Chemistry Research*, 64(52):24982–24993, 2025.

[2] S. Dörner, A. Mitsos, and D. Bongartz. Gas crossover in PEM electrolyzers: Experimental validation and improved oxygen crossover model. *Chemical Engineering Science*, 324:123310, 2026.

[3] S. Dörner, J. Paduch, C. Plath, M. Wessling, A. Mitsos, and D. Bongartz. Multispecies ion exchange model with competitive adsorption for iron removal in PEM water electrolysis. *Chemical Engineering Research and Design*, 222:325–339, 2025.

[4] J. Paduch. Modellierung und Simulation der Reduzierung von Eisenionen in einer PEM-Elektrolyse-Anlage (modeling and simulation of iron ion reduction in a PEM electrolysis plant). Master's thesis, RWTH Aachen University, Chair of Chemical Process Engineering, Aachen, Germany, 2022.

[5] P. Lucht. Modelling and simulation of degradation-causing ion release in PEM electrolysis plants. Master's thesis, Hochschule für Angewandte Wissenschaften Hamburg (HAW Hamburg), Faculty of Engineering and Computer Science, Hamburg, Germany, 2022.

[6] M. Carmo, D. L. Fritz, J. Mergel, and D. Stolten. A comprehensive review on PEM water electrolysis. *International journal of hydrogen energy*, 38(12):4901–4934, 2013.

[7] S. G. Simoes, J. Catarino, A. Picado, T. F. Lopes, S. di Berardino, F. Amorim, F. Gírio, C. Rangel, and T. Ponce de Leão. Water availability and water usage solutions for electrolysis in hydrogen production. *Journal of Cleaner Production*, 315:128124, 2021.

[8] L. S. McNeill and M. Edwards. Iron pipe corrosion in distribution systems. *Journal-American Water Works Association*, 93(7):88–100, 2001.

[9] L. Gubler, S. M. Dockheer, and W. H. Koppenol. Radical (HO•, H• and HOO•) formation and ionomer degradation in polymer electrolyte fuel cells. *Journal of The Electrochemical Society*, 158(7):B755, 2011.

[10] R. Borup, J. Meyers, B. Pivovar, Y. S. Kim, R. Mukundan, N. Garland, D. Myers, M. Wilson, F. Garzon, D. Wood, et al. Scientific aspects of polymer electrolyte fuel cell durability and degradation. *Chemical reviews*, 107(10):3904–3951, 2007.

[11] M. Chandesris, V. Médeau, N. Guillet, S. Chelghoum, D. Thoby, and F. Fouda-Onana. Membrane degradation in PEM water electrolyzer: Numerical modeling and experimental evidence of the influence of temperature and current density. *International Journal of Hydrogen Energy*, 40(3):1353–1366, 2015.

[12] M. Schalenbach, M. Carmo, D. L. Fritz, J. Mergel, and D. Stolten. Pressurized PEM water electrolysis: Efficiency and gas crossover. *International Journal of Hydrogen Energy*, 38(35):14921–14933, 2013.

[13] A. Shah, T. Ralph, and F. Walsh. Modeling and simulation of the degradation of perfluorinated ion-exchange membranes in PEM fuel cells. *Journal of The Electrochemical Society*, 156(4):B465, 2009.

[14] M. Ghelichi, P.-E. A. Melchy, and M. H. Eikerling. Radically coarse-grained approach to the modeling of chemical degradation in fuel cell ionomers. *The Journal of Physical Chemistry B*, 118(38):11375–11386, 2014.

[15] S. H. Frensch, G. Serre, F. Fouda-Onana, H. C. Jensen, M. L. Christensen, S. S. Araya, and S. K. Kær. Impact of iron and hydrogen peroxide on membrane degradation for polymer electrolyte membrane water electrolysis: Computational and experimental investigation on fluoride emission. *Journal of Power Sources*, 420:54–62, 2019.

[16] P. Choi, D. G. Bessarabov, and R. Datta. A simple model for solid polymer electrolyte (SPE) water electrolysis. *Solid State Ionics*, 175(1-4):535–539, 2004.

[17] H. Ito, T. Maeda, A. Nakano, and H. Takenaka. Properties of nafion membranes under PEM water electrolysis conditions. *International journal of hydrogen energy*, 36(17):10527–10540, 2011.

[18] P. Trinke, B. Bensmann, and R. Hanke-Rauschenbach. Current density effect on hydrogen permeation in PEM water electrolyzers. *International Journal of Hydrogen Energy*, 42(21):14355–14366, 2017.

[19] E. Afshari, S. Khodabakhsh, N. Jahantigh, and S. Toghyani. Performance assessment of gas crossover phenomenon and water transport mechanism in high pressure PEM electrolyzer. *International Journal of Hydrogen Energy*, 46(19):11029–11040, 2021.

[20] R. Omrani and B. Shabani. Hydrogen crossover in proton exchange membrane electrolysers: The effect of current density, pressure, temperature, and compression. *Electrochimica acta*, 377:138085, 2021.

[21] S. Melis, G. Cao, and M. Morbidelli. A new model for the simulation of ion exchange equilibria. *Industrial & engineering chemistry research*, 34(11):3916–3924, 1995.

[22] T. R. Van Assche, G. V. Baron, and J. F. Denayer. An explicit multicomponent adsorption isotherm model: accounting for the size-effect for components with langmuir adsorption behavior. *Adsorption*, 24:517–530, 2018.

[23] Q. Feng, G. Liu, B. Wei, Z. Zhang, H. Li, H. Wang, et al. A review of proton exchange membrane water electrolysis on degradation mechanisms and mitigation strategies. *Journal of Power Sources*, 366:33–55, 2017.

[24] A. Collier, H. Wang, X. Z. Yuan, J. Zhang, and D. P. Wilkinson. Degradation of polymer electrolyte membranes. *International Journal of Hydrogen Energy*, 31(13): 1838–1854, 2006.

[25] F. D. Coms. Mechanisms of membrane degradation. *Journal of The Electrochemical Society*, 155(8):B844–B848, 2008.

[26] I. Vincent et al. The effects of compression on proton exchange membrane degradation in fuel cells and electrolyzers: a review. *Journal of Materials Chemistry A*, 6 (10):4698–4721, 2018.

[27] X. Li et al. Hydroxyl radical formation in PEM fuel cells under electrochemical conditions. *Journal of The Electrochemical Society*, 165(9):F572–F578, 2018.

[28] P. Frühwirt, A. Kregar, J. T. Törring, T. Katrašnik, and G. Gescheidt. Holistic approach to chemical degradation of nafion membranes in fuel cells: modelling and predictions. *Physical Chemistry Chemical Physics*, 22(10):5647–5666, 2020.

[29] C. Eckert, P. Trinke, B. Bensmann, and R. Hanke-Rauschenbach. Coupled simulation of chemical membrane degradation and gas crossover in PEM water electrolysis. In *244th ECS Meeting, Gothenburg, Sweden*, October 2023.

[30] P. Trinke, B. Bensmann, and R. Hanke-Rauschenbach. Experimental evidence of increasing oxygen crossover with increasing current density during PEM water electrolysis. *Electrochemistry Communications*, 82:98–102, 2017.

[31] K. H. Wong and E. Kjeang. Macroscopic in-situ modeling of chemical membrane degradation in polymer electrolyte fuel cells. *Journal of The Electrochemical Society*, 161(9):F823, 2014.

[32] V. A. Sethuraman, J. W. Weidner, A. T. Haug, M. Pemberton, and L. V. Protsailo. Importance of catalyst stability vis-à-vis hydrogen peroxide formation rates in PEM fuel cell electrodes. *Electrochimica Acta*, 54(23):5571–5582, 2009.

[33] M. Zatoń, J. Rozière, and D. Jones. Current understanding of chemical degradation mechanisms of perfluorosulfonic acid membranes and their mitigation strategies: a review. *Sustainable Energy & Fuels*, 1(3):409–438, 2017.

[34] V. Stanic and M. Hoberecht. Mechanism of pinhole formation in membrane electrode assemblies for PEM fuel cells. *ECS Proceedings Volumes*, 2004(1):391, 2004.

[35] M. Chandesris, R. Vincent, L. Guetaz, J.-S. Roch, D. Thoby, and M. Quinaud. Membrane degradation in PEM fuel cells: From experimental results to semi-empirical degradation laws. *International Journal of Hydrogen Energy*, 42(12):8139–8149, 2017.

[36] H. Ito, N. Miyazaki, M. Ishida, and A. Nakano. Cross-permeation and consumption of hydrogen during proton exchange membrane electrolysis. *International journal of hydrogen energy*, 41(45):20439–20446, 2016.

[37] S. Fahr, F. K. Engel, S. Rehfeldt, A. Peschel, and H. Klein. Overview and evaluation of crossover phenomena and mitigation measures in proton exchange membrane (pem) electrolysis. *International Journal of Hydrogen Energy*, 68:705–721, 2024.

[38] D. Bessarabov, A. Kruger, S. M. Luopa, J. Park, A. A. Molnar, and K. A. Lewinski. Gas crossover mitigation in PEM water electrolysis: hydrogen cross-over benchmark study of 3M's Ir-NSTF based electrolysis catalyst-coated membranes. *ECS Transactions*, 75(14):1165, 2016.

[39] S. Shibata. The concentration of molecular hydrogen on the platinum cathode. *Bulletin of the Chemical Society of Japan*, 36(1):53–57, 03 2006.

[40] H. Matsushima, D. Kiuchi, and Y. Fukunaka. Measurement of dissolved hydrogen supersaturation during water electrolysis in a magnetic field. *Electrochimica Acta*, 54(24):5858–5862, 2009.

[41] Green hydrogen – process analytics and instrumentation solution, 2022. URL https://assets.new.siemens.com/siemens/assets/api/uuid:0836abe5-5216-4cb7-af31-29cd5f4f2f16/dipa-b10287-00-7600flyergreen-hydrogen-300.pdf. Technical flyer (PDF), Accessed: 2025-05-06.

[42] M. Schalenbach, T. Hoefner, P. Paciok, M. Carmo, W. Lueke, and D. Stolten. Gas permeation through nafion. part 1: measurements. *The Journal of Physical Chemistry C*, 119(45):25145–25155, 2015.

[43] A. J. Bard, L. R. Faulkner, and H. S. White. *Electrochemical methods: fundamentals and applications*. John Wiley & Sons, 3 edition, 2022.

[44] M. Schalenbach, G. Tjarks, M. Carmo, W. Lueke, M. Mueller, and D. Stolten. Acidic or alkaline? Towards a new perspective on the efficiency of water electrolysis. *Journal of The Electrochemical Society*, 163(11):F3197, 2016.

[45] S. Shibata. Supersolubility of hydrogen in acidic solution in the vicinity of hydrogen-evolving platinum cathodes in different surface states. *Denki Kagaku oyobi Kogyo Butsuri Kagaku*, 44(10):709–712, 1976.

[46] S. Shibata. Supersaturation of oxygen in acidic solution in the vicinity of an oxygen-evolving platinum anode. *Electrochimica Acta*, 23(7):619–623, 1978.

[47] Z. Abdin, C. Webb, and E. M. Gray. Modelling and simulation of a proton exchange membrane (PEM) electrolyser cell. *International journal of hydrogen energy*, 40(39): 13243–13257, 2015.

[48] P. Trinke, B. Bensmann, S. Reichstein, R. Hanke-Rauschenbach, and K. Sundmacher. Hydrogen permeation in PEM electrolyzer cells operated at asymmetric pressure conditions. *Journal of The Electrochemical Society*, 163(11):F3164, 2016.

[49] R. Battino. Solubility data series. *Oxygen and ozone*, 7:412, 1981.

[50] D. L. Wise and G. Houghton. The diffusion coefficients of ten slightly soluble gases in water at 10–60 c. *Chemical Engineering Science*, 21(11):999–1010, 1966.

[51] P. Medina and M. Santarelli. Analysis of water transport in a high pressure PEM electrolyzer. *International Journal of Hydrogen Energy*, 35(11):5173–5186, 2010.

[52] L. B. Newcomb, M. E. Marucci, and J. R. Green. Explosion limits of hydrogen–oxygen mixtures from nonequilibrium critical points. *Physical Chemistry Chemical Physics*, 20(23):15746–15752, 2018.

[53] M. Barros, P. Arroyo, E. Sousa-Aguiar, and C. Tavares. Thermodynamics of the exchange processes between K^+, Ca^{2+} and Cr^{3+} in zeolite NaA. *Adsorption*, 10: 227–235, 2004.

[54] M. Al-Anber and Z. A. Al-Anber. Utilization of natural zeolite as ion-exchange and sorbent material in the removal of iron. *Desalination*, 225(1):70–81, 2008.

[55] M. R. Moghadam, N. Nasirizadeh, Z. Dashti, and E. Babanezhad. Removal of Fe(II) from aqueous solution using pomegranate peel carbon: equilibrium and kinetic studies. *International Journal of Industrial Chemistry*, 4(1):1–6, 2013.

[56] R. Griffin and J. Jurinak. Kinetics of the phosphate interaction with calcite. *Soil Science Society of America Journal*, 38(1):75–79, 1974.

[57] R. Misra, S. Jain, and P. Khatri. Iminodiacetic acid functionalized cation exchange resin for adsorptive removal of Cr(VI), Cd(II), Ni(II) and Pb(II) from their aqueous solutions. *Journal of Hazardous Materials*, 185(2):1508–1512, 2011.

[58] S. Azizian. Kinetic models of sorption: a theoretical analysis. *Journal of Colloid and Interface Science*, 276(1):47–52, 2004.

[59] H. C. Thomas. Heterogeneous ion exchange in a flowing system. *Journal of the American Chemical Society*, 66(10):1664–1666, 1944.

[60] Y. A. Mustafa and S. E. Ebrahim. Utilization of Thomas model to predict the breakthrough curves for adsorption and ion exchange. *Journal of Engineering*, 4 (16):6206–6223, 2010.

[61] W. Rudzinski and D. H. Everett. *Adsorption of gases on heterogeneous surfaces*. Academic Press, 2012.

[62] E. Bernardi, M. Bignozzi, C. Chiavari, N. Gandolfi, C. Martini, A. Mattei, and S. Sessa. Corrosion of AISI 316L in ultrahigh-purity water: Surface analyses and metal release. *Pharmaceutical Engineering*, 35:71–77, 03 2015.

[63] A. S. Benson, A. M. Dietrich, and D. L. Gallagher. Evaluation of iron release models for water distribution systems. *Critical Reviews in Environmental Science and Technology*, 42(1):44–97, 2012.

[64] Sandmeyer Steel Company. Specification sheet: Alloy 316/316L (UNS S31600, S31603) W. Nr. 1.4401, 1.4404. https://www.sandmeyersteel.com/images/316-316L-317L-Spec-Sheet.pdf, 2024. Accessed: 2024-24-07.

[65] T. K. Sherwood, R. L. Pigford, and C. R. Wilke. Mass transfer. *McGraw-Hill*, 1975.

[66] Q. Hu, D. Wang, S. Pang, and L. Xu. Prediction of breakthrough curves for multi-component adsorption in a fixed-bed column using logistic and gompertz functions. *Arabian Journal of Chemistry*, 15(9):104034, 2022.

[67] F. Helfferich and J. Dranoff. *Ion Exchange*. McGraw-Hill, 1963.

[68] W. E. Schiesser. *The numerical method of lines: integration of partial differential equations*. Elsevier, 2012.

[69] R. E. Mickens. *Nonstandard finite difference models of differential equations*. world scientific, 1993.

[70] M. Ehrhardt and R. E. Mickens. A nonstandard finite difference scheme for convection–diffusion equations having constant coefficients. *Applied Mathematics and Computation*, 219(12):6591–6604, 2013.

[71] H. Fatoorehchi and M. Ehrhardt. Numerical and semi-numerical solutions of a modified thévenin model for calculating terminal voltage of battery cells. *Journal of Energy Storage*, 45:103746, 2022.

[72] R. L. Burden, J. D. Faires, and A. M. Burden. *Numerical analysis*. Cengage learning, 10 edition, 2015.

[73] G. Ahmetli and E. Tarlan. Fe(II/III) adsorption onto styrene/divinyl benzene based polymers. *Journal of Applied Polymer Science*, 104(4):2696–2703, 2007.

[74] aqion GmbH. aqion – aqueous chemistry software. https://www.aqion.de, 2024. Accessed: 2024-01-11.

[75] G. Seber and G. A. Seber. Nonlinear regression models. *The Linear Model and Hypothesis: A General Unifying Theory*, pages 117–128, 2015.

[76] J. V. Beck and K. J. Arnold. *Parameter estimation in engineering and science*. James Beck, 1977.

[77] LANXESS. Lewatit tp 207 data sheet. https://www.lenntech.com/Data-sheets/Lewatit-TP-207-L.pdf, 2024. Accessed: 2024-01-11.

[78] J. Buffle, Z. Zhang, and K. Startchev. Metal flux and dynamic speciation at (bio) interfaces. part I: Critical evaluation and compilation of physicochemical parameters for complexes with simple ligands and fulvic/humic substances. *Environmental science & technology*, 41(22):7609–7620, 2007.

[79] V. Inglezakis and M. Fyrillas. Experimental study of zeolitic diffusion by use of a concentration-dependent surface diffusion model. *Heliyon*, 5(7):e02143, 2019.

[80] D. M. Ruthven. *Principles of adsorption and adsorption processes*. John Wiley & Sons, 1984.

[81] M. Sahimi. *Flow and transport in porous media and fractured rock: from classical methods to modern approaches*. John Wiley & Sons, 2011.

[82] T. Rigg, W. Taylor, and J. Weiss. The rate constant of the reaction between hydrogen peroxide and ferrous ions. *The Journal of chemical physics*, 22(4):575–577, 1954.

[83] C. Walling and A. Goosen. Mechanism of the ferric ion catalyzed decomposition of hydrogen peroxide. effect of organic substrates. *Journal of the American Chemical Society*, 95(9):2987–2991, 1973.

[84] T. Lundström, H. Christensen, and K. Sehested. Reactions of the HO_2 radical with OH, H, Fe^{2+} and Cu^{2+} at elevated temperatures. *Radiation Physics and Chemistry*, 69(3):211–216, 2004.

[85] G. Jayson, B. Parsons, and A. J. Swallow. Oxidation of ferrous ions by perhydroxyl radicals. *Journal of the Chemical Society, Faraday Transactions 1: Physical Chemistry in Condensed Phases*, 69:236–242, 1973.

[86] C. Lee and J. Yoon. Temperature dependence of hydroxyl radical formation in the hv/$Fe_3{}^+$/H_2O_2 and $Fe_3{}^+$/H_2O_2 systems. *Chemosphere*, 56(10):923–934, 2004.

[87] Y. Lee, C. Lee, and J. Yoon. High temperature dependence of 2, 4-dichlorophenoxyacetic acid degradation by Fe^{3+}/H_2O_2 system. *Chemosphere*, 51 (9):963–971, 2003.

[88] P. A. Giguère and I. Liu. Kinetics of the thermal decomposition of hydrogen peroxide vapor. *Canadian Journal of Chemistry*, 35(4):283–293, 1957.

[89] H. Christensen and K. Sehested. Pulse radiolysis at high temperatures and high pressures. *Radiation Physics and Chemistry (1977)*, 18(3-4):723–731, 1981.

[90] F. Dainton and J. Rowbottom. The primary radical yield in water. a comparison of the photolysis and radiolysis of solutions of hydrogen peroxide. *Transactions of the Faraday Society*, 49:1160–1173, 1953.

[91] B. H. Bielski. Reevaluation of the spectral and kinetic properties of HO_2 and O_2-free radicals. *Photochemistry and Photobiology*, 28(4-5):645–649, 1978.

[92] T. Lundström, H. Christensen, and K. Sehested. The reaction of hydrogen atoms with hydrogen peroxide as a function of temperature. *Radiation Physics and Chemistry*, 61(2):109–113, 2001.

[93] H. Christensen and K. Sehested. Reaction of hydroxyl radicals with hydrogen at elevated temperatures. determination of the activation energy. *The Journal of Physical Chemistry*, 87(1):118–120, 1983.

[94] A. Dreizler and E. Roduner. Reaction kinetics of hydroxyl radicals with model compounds of fuel cell polymer membranes. *Fuel Cells*, 12(1):132–140, 2012.

[95] P. Maruthamuthu, S. Padmaja, and R. E. Huie. Rate constants for some reactions of free radicals with haloacetates in aqueous solution. *International Journal of Chemical Kinetics*, 27(6):605–612, 1995.

[96] T. Madden, D. Weiss, N. Cipollini, D. Condit, M. Gummalla, S. Burlatsky, and V. Atrazhev. Degradation of polymer-electrolyte membranes in fuel cells: I. experimental. *Journal of The Electrochemical Society*, 156(5):B657, 2009.

[97] L. Xia, M. Ni, Q. Xu, H. Xu, and K. Zheng. Optimization of catalyst layer thickness for achieving high performance and low cost of high temperature proton exchange membrane fuel cell. *Applied Energy*, 294:117012, 2021.

[98] A. B. Anderson and T. V. Albu. Catalytic effect of platinum on oxygen reduction an ab initio model including electrode potential dependence. *Journal of The Electrochemical Society*, 147(11):4229, 2000.

[99] R. Treybal. *Mass-transfer Operations*. Chemical engineering series. McGraw-Hill, 1955.

[100] A. Izadi, A. Mohebbi, M. Amiri, and N. Izadi. Removal of iron ions from industrial copper raffinate and electrowinning electrolyte solutions by chemical precipitation and ion exchange. *Minerals Engineering*, 113:23–35, 2017.